Quantum Estimation in Driven-Dissipative Optomechanics: Beyond the Linear Model

Kamila Sala

Thesis submitted to The University of Nottingham for the degree of Doctor of Philosophy

June 2022

Abstract

This thesis examines the optimal estimation of parameters in a variety of quantum oscillator models, including cavity quantum optomechanics and the quantum van der Pol oscillator. To achieve this, we employ theoretical tools from open quantum systems, quantum estimation theory and Gaussian states. In all cases, we compare the ultimate limits to parameter estimation (quantum Cramer-Rao bounds) to the performance of experimentally feasible observables (e.g. quadrature or number operator measurements).

The majority of the thesis addresses the estimation of the "linear" and "quadratic" coupling constants in strongly driven and dissipative optomechanical models, which are well described by bilinear master equations and Gaussian steady states. In this framework, we explore how the estimation precision can be affected by temperature, drive strength, detuning and higher order corrections to the optomechanical Hamiltonian. Through a combination of analytical and numerical methods, we find that temperature is not always detrimental to the estimation precision. We also find that quadrature measurements can perform close to the ultimate bounds in appropriate parameter regimes.

The last chapter focuses instead on estimating the ratio (λ) between linear amplification and non-linear damping in a quantum van der Pol oscillator. We present both numerical and (approximate) analytical results covering all parameter regimes. In the steady state, we find that the quantum Cramer-Rao bound can in principle be saturated by a measurement of the number operator. We also observe divergent behaviour of the quantum Fisher information (which implies a vanishing quantum Cramer-Rao bound) for $\lambda \to 0$. The origin and interpretation of such singular behaviour is left as an investigation for future work.

Acknowledgements

I would like to thank my supervisors, Dr Tommaso Tufarelli and Dr Andrew Armour for all their help and support throughout the course of my PhD. I could not have done it without their constant encouragement and patience. Thank you for making it an enjoyable experience.

Contents

Abstract **i**

Acknowledgements **ii**

1 Introduction **1**

1.1 Outline of the thesis 5

2 Quantum Estimation Theory **10**

2.1 Introduction 10

2.2 Single parameter estimation 13

2.3 Multi-parameter estimation 16

2.3.1 Single parameter approximation to multi-parameter estimation theory 19

2.4 Quantum estimation for Gaussian models 20

3 Quantum Optomechanics **24**

3.1 Introduction 24

3.2 Hamiltonian models of optomechanics 28

3.3 Dissipative dynamics 34

3.4 Gaussian dynamics approximation 39

3.4.1 General Gaussian formalism 39

3.4.2 Bilinear approximation of optomechanics 41

4 Parameter estimation in the linear model **47**

4.1 Introduction 47
4.2 Single parameter Gaussian state estimation 51
4.3 Red-detuned regime 54
4.4 Resonant regime 61

5 Parameter estimation beyond the linear model 68

5.1 Introduction 68
5.2 Multi-parameter Gaussian state estimation 71
5.3 Red-detuned regime 74
5.4 Purely quadratic regime 84
5.5 Conclusion: quantum estimation in beyond linear-model optomechanics . 93

6 Quantum van der Pol Oscillator 95

6.1 Introduction 95
6.2 Quantum model 97
  6.2.1 Master equation 97
  6.2.2 Exact solution 99
  6.2.3 Behaviour of the steady state occupation probabilities 101
6.3 Quantum estimation 104
6.4 Numerical calculations 105
6.5 Analytical analysis 108
  6.5.1 Strong two-phonon emission 108
  6.5.2 Weak two-phonon emission 110
6.6 Conclusions 111

7 Conclusion 114

A Implicit differentiation 119

B Derivation of the amplitude equation for limit cycle oscillations 123

List of Figures

3.1 Schematic of an optomechanical set-up in Fabry-Perot geometry. The system consists of a cavity of bare length L and position-dependent frequency $\omega(X_b)$ which is composed of two mirrors, one fixed and the other movable mounted on a spring. To a good approximation, the movable mirror can be assumed to behave as a mechanical oscillator with frequency ω_m and effective mass m. Additionally, the interaction of the optomechanical system with its cavity and mechanical environments leads to cavity decay and mechanical damping of the oscillator at rates κ and Γ_m, respectively. The mechanical element is also characterised by a temperature T_m. The cavity mode is driven by an external laser. Adapted from [4, 82]. 26

4.1 Schematic of the parameter estimation methodology for driven-dissipative optomechanics. We consider a driven-dissipative optomechanical system featuring a driven (by an external laser) and lossy (photons escaping the cavity) cavity and a damped mechanical oscillator. The mechanical support has low but finite temperature (leading to a non-zero thermal occupation number). The optomechanical coupling arises due to the radiation pressure on the movable mirror. Once the system has reached a steady state we measure an observable. We repeat the measurement many times to get the statistics. Finally, we process the data to find the best guess for the coupling parameters of interest. Reproduced from [1]. 49

4.2 Log-log plot of the relative error bound on g_1 (as implied by the QFI) against the intracavity photon number, $|\alpha|^2$, as predicted by the linear model in the red-detuned regime in the zero temperature (purple dot-dashed line), low temperature (black line) and high temperature (orange dashed line) scenarios. Adapted from [1]. 56

4.3 Log-log plots comparing the contributions from the variances (orange dashed line) and the averages (green circles) to the $\tilde{g}_1-$QFI in the linear model in the red-detuned regime (black line) in (a) the zero temperature scenario as well as the (b) $T = 1$ mK and (c) $T = 80$ mK cases. 57

4.4 (a) Relative error bound on g_1 as a function of the intracavity photon number, $|\alpha|^2$, as implied by the global, light and mechanics QFIs in the red-detuned regime in the cases of zero temperature (black line, purple dot-dashed line, blue squares, respectively) and high temperature (orange dashed line, red dotted line and green circles, respectively). Adapted from [1]. (b) and (c) are the log-log plots of the ratios of the FI for the measurements of Q ($\mathsf{FI}(Q)$, purple dot-dashed line), P ($\mathsf{FI}(P)$, red dotted line), X_b ($\mathsf{FI}(X_b)$, green circles) and P_b ($\mathsf{FI}(P_b)$, orange dashed line) to light and mechanics QFIs against the intracavity photon number, $|\alpha|^2$, in the red-detuned regime for g_1 in the high and zero temperature scenarios, respectively. 58

4.5 Log-log plots of the relative error bound on g_1 (as implied by the QFI) against the intracavity photon number, $|\alpha|^2$, in the red-detuned regime (black line) and the measurements of P (red dotted line), Q (purple dot-dashed line), X_b (green circles) and P_b (orange dashed line). (a) and (b) are for g_1 in the high and zero temperature scenario, respectively. 60

4.6 Log-log plots of the ratios of the FI for the measurements of Q ($\mathsf{FI}(Q)$, purple dot-dashed line), P ($\mathsf{FI}(P)$, red dotted line), X_b ($\mathsf{FI}(X_b)$, green circles) and P_b ($\mathsf{FI}(P_b)$, orange dashed line) to the QFI against the intracavity photon number, $|\alpha|^2$, in the red-detuned regime. (a) and (b) are for g_1 in the high and zero temperature scenario, respectively. 61

4.7 (a) Log-log plot of the relative error bound on g_1 (as implied by the QFI) against the intracavity photon number, $|\alpha|^2$, as predicted by the linear model in the resonant regime in the zero temperature (purple dot-dashed line), low temperature (black line) and high temperature (orange dashed line) scenarios. (b) Semi-log plot of the relative error bound on g_1 (as implied by the QFI) against the temperature of the mechanical bath, T_m, for the intracavity photon number $\log_{10}|\alpha|^2 = 3.5$. 63

4.8 Log-log plots comparing the contributions from (a) the averages and (b) the variances to the $\tilde{g}_1-$QFI in the linear model in the resonant regime in the $T = 0$ K (orange dashed line), $T = 1$ mK (black line) and $T = 80$ mK (green circles) cases. 64

4.9 Relative error bound on g_1 as a function of the intracavity photon number, $|\alpha|^2$, as implied by the global, light and mechanics QFIs in the resonant regime in the cases of zero temperature (black line, purple dot-dashed line, blue squares, respectively) and high temperature (orange dashed line, red dotted line and green circles, respectively). 65

4.10 Log-log plots of relative error bound on g_1 (as implied by the QFI) against the intracavity photon number, $|\alpha|^2$, in the resonant regime (black line) and the measurements of P (red dotted line), Q (purple dot-dashed line), X_b (green circles) and P_b (orange dashed line). (a) and (b) are for g_1 in the high and zero temperature scenario, respectively. 66

5.1 (a) Log-log plot of the relative error bound on g_1 against the intracavity photon number, $|\alpha|^2$. The plot compares linear and quadratic models in the zero temperature (blue squares and purple dot-dashed line, respectively), low temperature (brown triangles and black line, respectively) and high temperature (green circles and orange dashed line, respectively) scenarios. (b)-(d) Log-log plots comparing the contributions from the variances (orange dashed line) and the averages (green circles) to the $\tilde{g}_1-$QFI in the quadratic model (black line) for $\tilde{g}_1$ in (b) the zero temperature scenario as well as the (c) $T = 1$ mK and (d) $T = 80$ mK cases. Reproduced from [1] 76

5.2 Log-log plot of the relative error bound on g_2 against the intracavity photon number, $|\alpha|^2$, as predicted by the quadratic model in the zero temperature (purple dot-dashed line), low temperature (black line) and high temperature (orange dashed line) scenarios. (b)-(d) Log-log plots comparing the variances (orange dashed line) and averages (green circles) contributions to QFI (black line) for $\tilde{g}_2$ at (b) zero temperature as well as the (c) $T = 1$ mK and (d) $T = 80$ mK cases. Reproduced from [1]. 78

5.3 Semi-log plot of the relative error bound on g_2 (as implied by the QFI) against the temperature of the mechanical bath, T_m, for the intracavity photon number $\log_{10}|\alpha|^2 = 3.5$. 79

5.4 Relative error bounds on the coupling strengths (a) g_1 and (b) g_2, against the intracavity photon number, $|\alpha|^2$, as predicted by the global, light and mechanics QFIs in the zero temperature (black line, purple dot-dashed line, blue squares, respectively) and high temperature (orange dashed line, red dotted line and green circles, respectively) scenarios. Reproduced from [1]. 80

5.5 Log-log plots of the relative error bounds on the coupling parameters g_1 and g_2 against the intracavity photon number, $|\alpha|^2$, as predicted by the QFI (black line) and the measurements of P (red dotted line), Q (purple dot-dashed line), X_b (green circles) and P_b (orange dashed line). (a) and (b) are for g_1 and g_2 in the high temperature scenario, whilst (c) and (d) are for g_1 and g_2 in the zero-temperature scenario. Reproduced from [1]. 82

5.6 (a) Log-log plot comparing the contributions from the covariance element (orange dashed line) and the average (green circles) to the $\tilde{g}_2$-FI for the measurement of P in the quadratic model (black line) in the high temperature scenario. (b) Semi-log plot comparing the contributions from the covariance element (orange dashed line) to the $\tilde{g}_2$-FI for the measurement of P in the quadratic model (black line) in the high temperature scenario. 83

5.7 Log-log plot of the relative error bound on g_2 (as implied by the QFI) against the intracavity photon number, $|\alpha|^2$, as predicted by the purely quadratic model in the red-detuned regime for $g_2 = 10$ Hz and $g_2 = 100$ Hz in the zero temperature (purple dot-dashed line and red dotted line, respectively), low temperature (black line and green dashed line, respectively) and high temperature (orange circles and blue squares, respectively) scenarios. 91

5.8 Log-log plots of the relative error bound on g_2 (as implied by the QFI) against the intracavity photon number, $|\alpha|^2$, for $g_2 = 10$ Hz and $g_2 = 100$ Hz in the red-detuned regime (black line and red dotted line, respectively) as well as the measurements of X_b (green circles and blue squares, respectively) and P_b (orange dashed line and purple dot-dashed line, respectively). (a) and (b) are for g_2 in the high and zero temperature scenarios, respectively. 92

6.1 Semi-log plots of the steady state occupation probabilities p_n against the phonon number n for (a) small ($\lambda = 0.01$ - green circles and $\lambda = 0.1$ - red squares) and (b) intermediate λ values ($\lambda = 5$ - green circles and $\lambda = 15$ - red squares). 102

6.2 Plot comparing the steady state occupation probabilities p_n for large λ values as given by the full analytical form ($\lambda = 50$ - black line and $\lambda = 70$ - purple dot-dashed line) and the Gaussian approximation ($\lambda = 50$ - orange, dashed line and $\lambda = 70$ - green circles). Here, the values specified by the full analytical form have been plotted as continuous curves although they are, strictly speaking, only defined for integer values of n. 103

6.3 (a) Semi-log plot of the numerical QFI, $Q_{diff}(\lambda_j)$, against the ratio of the strengths of phonon absorption (i.e. gain) and emission processes, λ. (b) Semi-log plot of the numerically computed function $\lambda Q(\lambda) - 1/3$ against λ. 108

6.4 (a) Semi-log plot of the QFI against the ratio of the strengths of phonon absorption (i.e. gain) and emission processes, λ. The plot compares the numerical QFI, $Q_{diff}(\lambda_j)$, (orange dashed line) and the power series QFI, $Q_{sum}(\lambda)$, (black line) in the region $0 < \lambda \leq 0.3$ (b) Plot comparing the numerically computed function $\lambda_j Q_{diff}(j) - 1/3$ (orange dashed line) and the power series evaluated function $\lambda Q_{sum} - 1/3$ (black line) in the region $0 < \lambda \leq 0.3$. 110

6.5 (a) Plot of the QFI against the ratio of the strengths of phonon absorption (i.e. gain) and emission processes, λ. The plot compares the numerical QFI, $Q_{diff}(j)$, (red dashed line) and the Gaussian QFI, $Q_{gauss}(\lambda)$, (black line) in the region $35 \leq \lambda \leq 80$ (b) Plot comparing the numerically computed function $\lambda_j Q_{diff}(\lambda_j) - 1/3$ (red dashed line) and the Gaussian evaluated function $\lambda Q_{gauss} - 1/3$ (black line) in the region $35 \leq \lambda \leq 80$. . 111

Chapter 1

Introduction

Quantum optomechanics is a rapidly evolving research field that focuses on the interaction between light and mechanical motion [1, 2, 3]. The origins of this field can be traced back to the 19th century, at which time the mechanical effects of light were already widely speculated [4]. The investigation of quantum optomechanical systems was pioneered by Braginsky and co-authors [5, 6, 7]. The rapid theoretical and experimental developments in this field have been subsequently driven by its wide range of potential applications including in fundamental physics and precision measurements. Indeed, when considering the many fundamental and technological applications of optomechanical systems, accurate knowledge of the light-matter coupling constants involved is essential. The aim of this thesis is to theoretically explore the best methods for estimating such constants in a variety of optomechanical models.

The mechanism responsible for the optomechanical interaction is radiation pressure, a phenomenon that was first postulated by Kepler in the 17th century [2, 8, 9]. The relevant physical theory, however, was not formulated until the 19th century and the existence of radiation pressure was only demonstrated experimentally at the beginning of the 1900s via light mill experiments [10]. In 1909, Einstein, through his study of the radiation pressure effects on a movable mirror, was able to correctly derive a formula describing wave-particle duality of black body radiation [11]. Thirty years later, the exchange of momentum between macroscopic objects and photons was evidenced experimentally for the very first time [12, 13].

The great potential of quantum optomechanical systems for precision measurements was realised early on [3]. These systems allow for highly precise detection of small forces, displacements, masses and accelerations, and as such, they are of great importance for many applications including gravitational wave detectors, scanning probe microscopy, and force sensing [2]. The sensitivity with which these parameters can be measured, however, is limited by quantum noise. Quantum noise, or quantum radiation pressure noise, is a fundamental consequence of the quantum nature of light [14]. The physical nature of the measurement, in particular, gives rise to quantum backaction, which inevitably affects the state of the mechanical element and introduces the standard quantum limit (SQL) for measurement sensitivity [4, 15]. This limit arises when the position of an oscillator is measured continuously and reflects a balance between the precision of the measurement and the quantum backaction that arises. The SQL was first established in works by Caves, Braginsky and co-authors, and sets a benchmark for the performance of gravitational wave detectors, such as LIGO [16, 17, 18]. However, the SQL is not a fundamental limit and can be evaded by adopting a more sophisticated measurement strategy (e.g. measuring only a single quadrature of the oscillator [19]).

In order to reach a regime where quantum effects become observable and hence where quantum levels of sensitivity can be reached all non-quantum noise sources, and in particular thermal noise, need to be removed as much as technologically possible [20, 21, 22]. A typical experimental goal in this direction is cooling the mechanical element to its ground state (or more generally, a pure state). In reality, however, the removal of all thermal phonons from the mechanical element poses an experimental challenge. Alongside quantum (and thermal) noise, the physical effects of radiation pressure may also have a hindering, or facilitating, effect on the measurement sensitivity of optomechanical parameters of interest. In fact, it was Braginsky who first realised the potential of radiation pressure for cooling macroscopic objects [5]. Indeed, it was discovered that through an effect known as "dynamical backaction" the mechanical element could, in theory, self-cool down to its ground state [6, 23, 24]. In short, dynamical backaction is a consequence of the finite delay between a position shift of the mechanical element and the response of the cavity field that leads to cooling or amplification of mechanical motion, depending on the detuning [7, 20]. However, to accurately model this radiation-pressure-induced backaction cooling and the associated cooling limits, a quantum treatment is required. Ultimately, the fundamental cooling limit is set by quantum fluctuations of light in the cavity. The prospect of ground state cooling has prompted a rapid development of the field of optomechanics over the past 20 years. In 2010 and 2011, breakthrough near ground state cooling of the mechanical element has been achieved in both microwave and optical domains [25, 26, 27, 28]. Dynamical backaction can be further exploited to allow the manipulation of mechanical motion in the quantum regime, hence revealing quantum signatures of large mechanical objects [29, 30, 31, 32]. This, in turn, could provide a direct route for testing quantum theories in largely unexplored parameter regimes.

The precision with which the desired optomechanical parameters can be measured may also be limited by the environment-induced quantum noise, i.e. shot noise [15]. Its impact, however, can be controlled through an appropriate choice of a measurement strategy. Quantum estimation theory (QET) provides the necessary tools to discern the optimal strategy for estimating unknown parameters in quantum systems [33]. Indeed, depending on the priori knowledge of the parameter, global or local QET can be employed to identify the optimal measurement strategy subject to appropriate criteria. These optimal quantum measurements offer a route for enhanced precision measurements compared to approaches based on semi-classical procedures. In some cases, the optimal measurements predicted by QET may not be technologically feasible. Whilst quantum technologies continue to evolve, however, QET can alternatively help discern which of the conventionally used measurement techniques comes closest to reaching the precision bounds.

While this thesis focuses mostly on "stable" optomechanical systems (e.g. red-detuned or resonant regimes), the blue-detuned regime is also interesting to explore. Here, dynamical backaction has an anti-damping effect on the mechanical motion, leading to the emergence of complex non-linear behaviour [4, 23, 34]. In this regime, the dynamical instability ensues as a result of the incident photons carrying more energy than the intracavity photons, and the mechanical element absorbing the extra energy [2]. In more detail, when the power of the laser driving the cavity is large enough, the intrinsic damping of the mechanical element will be overcome [2, 4, 34]. The energy of the mechanical element and the consequent amplification of mechanical motion will then continue to grow exponentially until becoming saturated by the onset of the non-linear effects [22]. At this point, the steady state regime is reached and the system starts to display self-induced oscillations. These self-sustained oscillations take the form of stable limit cycles, arising from the competition between amplification and non-linear damping.

The classical dynamics in the blue-detuned regime have been studied extensively in both experimental and theoretical settings [34]. The dynamical multistability, or the existence of multiple stable limit cycles, is one of the more prominent effects arising in the classical treatment of the optomechanical instability [2]. A quantum analysis also reveals non-classical features that can emerge in this regime [35, 36]. The dynamical state of the oscillator changes radically when limit cycles develop, which naturally poses a question of whether it is easier or harder to extract information about coupling parameters in this regime. However, the complexity of the underlying quantum dynamics makes this a difficult problem to explore. Therefore, in this thesis we explore parameter estimation in a much simpler quantum system that also displays limit cycle oscillations, namely a quantum van der Pol (vdP) oscillator [37]. For this system, much of the analysis can be done analytically [38] and the existence of a critical point [39] leads to particularly interesting behaviour.

1.1 Outline of the thesis

The goal of this thesis is to explore the application of local QET to estimate coupling parameters in driven-dissipative optomechanical systems. Accurate knowledge of these parameters is indeed essential for any application of these systems. The thesis also explores the application of local QET in a quantum vdP oscillator, a system that can aid our understanding of the quantum signatures, and in particular, the emergence of self-sustained limit cycles, in non-linear optomechanical systems.

Chapter 2 introduces QET, a tool that will be used to estimate unknown parameters in the studied quantum systems. Focusing on the local QET, first, single and multi-parameter estimation methods, and the associated precision bounds are presented. There, the feasibility and/or the conditions for saturating these bounds are also discussed. Then, the single parameter approximation to multi-parameter estimation theory is outlined. Within this approximation, the estimation methods applicable to Gaussian states are introduced. The general settings of the covariance matrix language are also presented, which the formulation of the QET in Gaussian models is reliant upon. With the Gaussian states being fully characterised by their first and second moments, the chapter finishes by explicitly quantifying the classical and quantum precision bounds in terms of these two quantities.

Chapter 3 analyses the main subject of the thesis, that is quantum optomechanics. Firstly, a historical review of the standard model of cavity optomechanics [40] is given. With the radiation pressure interaction being intrinsically non-linear, approximate Hamiltonian models are often employed; the linear and quadratic models are introduced and their limitations examined. This is followed by a discussion of open system dynamics. There, a master equation description for a driven-dissipative optomechanical system is identified. This description provides a more realistic representation of the system by accounting for its interaction with the environment. The influence of the detuning on the behaviour of the optomechanical system is also briefly explored. The last part of this chapter features parts of original research. In particular, it outlines the procedure for bilinearising the dynamics of a driven-dissipative optomechanical system within the framework of the quadratic model in the limit of strong cavity driving. The non-linearity of the resultant equations of motion for the first moments indicates the occurrence of static multistability within the system. In consequence of the bilinearisation, the system admits a Gaussian steady state. The investigation of the validity of the Gaussian dynamics approximation further reveals the need for a constraint on the strength of the quadratic optomechanical interaction, or equivalently the driving power.

Chapter 4 examines single parameter estimation in driven-dissipative optomechanics within the framework of the linear model in both red-detuned and resonant regimes. Both of these regimes feature a large region where the Gaussian formalism remains applicable, whilst the multistability of the system can be completely avoided. Armed with the closed-form expressions available for QET in Gaussian models, the chapter details the procedure for estimating the linear coupling constant. The goal of this chapter is to distinguish an optimal strategy for estimating this parameter from a range of experimentally feasible measurements as well as investigate the influence of driving and temperature on its estimation precision. The model parameters selected to explore this topic were motivated by recent experiments where near ground state cooling of a mechanical oscillator was achieved. In the red-detuned regime, the measurement of the mechanical position is found to constitute the best strategy for estimating the coupling parameter at all intracavity photon numbers in the explored range. Instead, for the resonant regime, the choice of an ultimate measurement strategy depends on both temperature and driving. In regards to temperature, for the red-detuned regime, temperature has a facilitating effect on the parameter estimation at lower driving powers. The estimation performance in the resonant regime, however, has considerably weaker temperature dependence, and at sufficiently high driving strengths the predicted QFI limits are qualitatively equal at all temperatures.

Chapter 5 expands on the previous discussion by considering single parameter approximation to multi-parameter estimation theory in driven-dissipative optomechanics within the framework of the quadratic model, strictly in the red-detuned regime. There, the effects of corrections due to the quadratic term on the estimation precision of the linear coupling constant are additionally explored. The chapter begins with a summary of the single parameter approximation to multi-parameter QET applicable to Gaussian models for one unknown parameter (at a time) - the linear or quadratic coupling constant. The numerical analysis reveals that for realistic values of the model parameters, the quadratic coupling parameter is significantly harder to estimate than the linear one at lower driving powers. At higher intracavity photon numbers, however, their estimation precisions becomes comparable. The measurement of the mechanical position is similarly found to constitute the best strategy for estimating the coupling parameters. Interestingly, in this case, temperature is found to have a facilitating effect on the estimation precision of the quadratic coupling constant at all intracavity photon numbers in the explored range. Chapter 5 also explores single parameter estimation in the red-detuned regime within the framework of the purely quadratic model. This model is obtained through a second-order expansion of the cavity frequency with respect to mechanical position in cases where the first order term vanishes. This part of the chapter begins with a detailed summary of the bilinearisation procedure along with a discussion of its validity in the case of a purely quadratic model. In this case, the equations of motion for the first moments are uncoupled and independent of the parameter of interest. There, an exact form for the steady state second moments is obtained and Gaussian QET theory is applied to the quadratic coupling constant. A numerical analysis reveals that a stronger optomechanical interaction leads to an improved estimation precision of the parameter at lower intracavity photon numbers. At sufficiently high driving powers, however, the estimation precision saturates at exactly the same value, irrespective of the strength of the interaction. In this case, it is also found that the measurement of the mechanical momentum constitutes the best strategy for estimating the quadratic coupling constant.

Chapter 6 investigates the application of local QET in a quantum vdP oscillator. The chapter begins with a summary of the classical model of the vdP oscillator along with an introduction to the corresponding quantum model. In this case, open system dynamics are assumed and the quantum vdP oscillator is described via a master equation. The way in which the relative simplicity of the quantum vdP model allows an exact evaluation of the steady state is then reviewed. The resulting steady state is found to be diagonal in the number state basis and purely dependent on the ratio of the rates of the linear and non-linear dissipative processes. QET is then employed leading to explicit formulas quantifying the classical and quantum precision bounds of the parameter. There, a measurement of the number operator is also shown to be optimal. The chapter proceeds with an outline of the numerical procedure for estimating the single parameter which controls the state of this system: the ratio of the rates of the dissipative processes. The numerical method reveals a contrasting behaviour of the quantum Fisher information (QFI) at small and large values of the ratio-of-rates parameter. Analytical methods are subsequently employed to investigate the behaviour of the QFI in these two limiting cases. For small values of the parameter, a power series expansion is used, whilst for large values the QFI is approximated via expressions available for QET in Gaussian models, adapted for scalar quantities. The analytical methods are found to agree well with the results obtained from the numerical methods. For small values of the parameter the QFI displays divergent behaviour, whilst for large values the QFI declines to zero.

The results covered in chapters 3 (Sec. 3.4), 4, 5 and 6 (Sec. 6.4-6.5) constitute original research undertaken in collaboration with Andrew Armour and Tommaso Tufarelli.

The key results on the multi-parameter estimation in driven-dissipative optomechanical systems described by a quadratic model in the red-detuned regime, are published in [1].

Chapter 2

Quantum Estimation Theory

2.1 Introduction

Accurate knowledge of the parameters of a quantum system is essential for understanding the behaviour or virtually any application of that system [1, 41]. However, many parameters, particularly those in quantum mechanical systems, remain elusive to direct measurements [33]. When this is the case, we resort to indirect measurements where the value of a parameter of interest is inferred from the data collected from the measurements of different observables. This, in turn, amounts to solving a parameter estimation problem whose solution gives the "best guess" for the actual parameter value [42]. In our case, "best" refers to a correct guess of the parameter on average whilst also minimising the variance of the estimates over many experimental runs. Quantum estimation theory (QET) then provides the theoretical tools to find the optimal measurement strategies for estimating parameters in quantum systems, i.e. the combination of observables and data analysis strategies that minimise the estimation error.

The theory of quantum parameter estimation was pioneered by Helstrom [43] and Holevo [44] in the late 1900s [45, 46]. This theory has a wide range of applications including in the detection of gravitational waves, clock synchronisation, magnetic, electric and gravitation field sensing et cetera [15, 42, 47, 48, 49, 50].

QET can be broken down into local and global theories [33, 42]. Intuitively, in local QET, the unknown parameter is in the neighbourhood of its “true value”, an order of magnitude estimate of which is typically known in advance, for example from first principles, material science modelling or from previously rough estimates [1]. Instead, in global QET, the parameter is typically assumed to be completely unknown to begin with, and as such it is not restricted to a neighbourhood of its true value [51]. More in detail, global QET seeks a measurement strategy that minimises the average error in estimating the parameter. Global QET has proven particularly useful for evaluating precision bounds set by unitary transformations, such as squeezing of the radiation field [52, 53]. Instead, local QET seeks a measurement strategy that maximises the Fisher information (FI) over all possible measurements, resulting in a fundamental quantity called the quantum Fisher information (QFI). Local QET has commonly been used to solve parameter estimation problems of open quantum systems. As this is the focus of the thesis, only the local theory will be considered from this point onward.

The ultimate limit to parameter estimation is set by the quantum Cramer Rao bound (QCRB) [33, 42]; the QCRB is the fundamental limit imposed by quantum mechanics on the achievable estimation precision [54]. The saturation of this bound is guaranteed in single parameter estimation theory provided that every mathematically permitted quantum measurement can be executed [1, 55, 56]. This, however, is not the case for the multi-parameter estimation theory, where multiple unknown parameters are estimated simultaneously, as optimal measurements for the various parameters may not be compatible [46]. The search for the most general conditions under which the QCRB in multi-parameter estimation theory can be saturated remains an active research pursuit.

Exploiting the QCRB, the ultimate limit to estimation precision can be quantified with the QFI in single parameter estimation theory, or the quantum Fisher information matrix (QFIM) in multi-parameter estimation theory [33, 46, 57]. The QFIM is a multi-parameter generalisation of the QFI with diagonal entries equal to the QFI of each individual parameter [42].

In single parameter estimation, a measurement is considered optimal if the FI associated with that measurement is equal to the QFI [33]. In this case, the ultimate estimation precision allowed by quantum mechanics can in principle be achieved [57]. However, the optimal measurement strategy may not always be realisable in practice [58]. For example, it may require technologically unfeasible measurements, or it may be implicitly dependent on the actual value of the parameter of interest which is unknown to begin with. The latter issue can be addressed by utilising adaptive measurements where the choice of an observable to be measured is updated dynamically based on the results of previous experimental runs. Thanks to the asymptotic nature of the QCRB, after many such runs the adaptive measurement will eventually converge to the optimal measurement. In multi-parameter estimation it is instead required that the FI matrix (a matrix of the estimation performances of various measurement strategies) is equal to the QFIM in order to regard a measurement strategy as optimal [42]. The existence of an optimal measurement strategy, however, is not guaranteed; since different parameters may be associated with different, generally non-commuting, optimal observables, a measurement strategy that is simultaneously optimal for all the unknown parameters may simply not exist.

For the majority of this thesis we shall be concerned with estimation problems that can be tackled within the formalism of Gaussian states [1]. This is particularly relevant for optomechanical models, but more generally open quantum systems described with Hamiltonians that are bilinear in the canonical operators which will in general admit a Gaussian steady state [59]. The appeal of these states lies in their simplicity: they can be fully characterised by their first and second moments [46, 61]. From an experimental standpoint, Gaussian states are also attractive as they can be easily created and manipulated. Beyond optomechanics, Gaussian states have various applications in quantum optics. The utilisation of Gaussian states also greatly facilitates the computation of the QFI (or the QFIM) which is necessary to evaluate the QCRB [63]. For such a case, the QFI will only depend on the state's first and second moments (along with their derivatives), the closed form expressions for which are available in the literature [55, 56].

This chapter is organised as follows. In Sec. 2.2 the key results of local QET along with an explanation of their origin are presented. The general framework of the single parameter estimation theory is also outlined. Then, in Sec. 2.4 the framework of single-parameter estimation theory is presented along with its application to Gaussian models. The covariance matrix language is also reviewed, which is an indispensable tool in the study and application of Gaussian states.

2.2 Single parameter estimation

The task of single parameter estimation theory is to estimate the value of an unknown parameter θ associated with a system [42, 59]. This amounts to finding an estimator $\hat{\theta}$, which is a function of the collected data that returns the "best guess" for the actual parameter value [33]. The precision of an estimator can be quantified via its mean squared error which can be conveniently expressed as the sum of the variance and the square of the bias of an estimator, $E[(\hat{\theta}-\theta)^2] = V(\hat{\theta}) + (E[\hat{\theta}]-\theta)^2$. In the case of an unbiased estimator, $E(\hat{\theta}) = \theta$; hence, by the definition of unbiasedness, the estimated value should on average be correct [55]. The average, in this regard, is intended over many repetitions of the same experiment (ideally infinite). Indeed, the mean squared error of an unbiased estimator can be quantified via its variance, such that higher precision implies lower variance.

The classical setting of a parameter estimation problem starts with a probabilistic model of the form $P(S = s|\theta)$, i.e. the conditional probability of obtaining the value s when measuring a random variable S, given that the parameter has the value θ [33]. This constitutes a statistical model for how the measured data S depends on the value of the unknown parameter θ. In essence, the estimation theory is all about manipulating the measured data in an optimal way to figure out (the best guess for) the value of θ. Developing an estimator $\hat{\theta}$ then entails using the knowledge of the model $P(S = s|\theta)$ combined with the actual data S to build a formula for the best guess, which for unbiased estimators is encapsulated in the variance, $V(\hat{\theta})$. In classical estimation theory, the optimal estimators are then those that saturate the Cramer-Rao bound (CRB)

$$V(\hat{\theta}) \geq \frac{1}{MF(\theta)}, \tag{2.1}$$

where M is the number of measurements and $F(\theta)$ is the FI [42]. The right-hand side of this inequality simply depends on the form of $P(S = s|\theta)$ along with the actual "true value" of θ. In accordance with this inequality, the FI quantifies the classical limit to estimation precision; it provides a measure for the amount of information that a random variable S carries about a parameter θ [64]. The FI is defined by an integral

$$F(\theta) = \int P(S = s|\theta) \left(\partial_\theta \ln P(S = s|\theta)\right)^2 ds = \int \frac{\left(\partial_\theta P(S = s|\theta)\right)^2}{P(S = s|\theta)} ds. \tag{2.2}$$

In a quantum setting of a parameter estimation problem the value of an unknown parameter θ is encoded in a density matrix ρ_θ, which in this context describes the state of a quantum system [33, 55]. The goal is to estimate this unknown parameter through a measurement of some observable on ρ_θ, described by a positive operator valued measure (POVM). The POVMs are the most general measurements, comprising of a set of non-negative operators $\Pi_s \geq 0$ that satisfy the completeness relation, $\sum_s \Pi_s = \mathbb{1}$ [42, 59]. Once a POVM has been chosen, the statistical model can be derived which is now of the form $P(S = s|\theta) = \mathrm{Tr}[\Pi_s \rho_\theta]$ [58]. From this, the CRB can be obtained, leading to a precision bound that is dependent on the chosen POVM. An appropriately chosen POVM thus guarantees that as much information as possible on the parameter can be extracted from the quantum state. Accordingly, a general quantum parameter estimation protocol involves the identification of a POVM, repeated measurement of the quantum system through this POVM and a high-precision estimation of the unknown parameter based on the data set.

The ultimate precision bound compatible with quantum mechanics can instead be determined by optimising the CRB over all possible POVMs [33]. Indeed, the optimal precision of a parameter θ is given by the QCRB, which for M experimental runs sets the ultimate lower bound for the variance $V(\hat{\theta})$ of an unbiased estimator of θ, as per

$$V(\hat{\theta}) \geq \frac{1}{MQ(\theta)}, \tag{2.3}$$

with $Q(\theta)$ the QFI [42, 55, 56, 59]. In accordance with this inequality, the ultimate precision for estimating an unknown parameter can be quantified with the QFI. Moreover, for any choice of a POVM, resulting in a specific value of $F(\theta)$, this is always bounded from above by $Q(\theta)$:

$$Q(\theta) \geq F(\theta). \tag{2.4}$$

In other words, irrespective of the choice of an observable, the QCRB cannot be beaten. Moreover, in a quantum setting of a parameter estimation problem, there are two optimisations: one on the POVM (in order to have the FI equal to the QFI) and one on the classical estimators (in order to saturate the FI).

In general, the QFI can be defined in terms of the Symmetric Logarithmic Derivative

(SLD), $\mathcal{L}_\theta$, a self-adjoint operator satisfying the equation [44]

$$(\mathcal{L}_\theta \rho_\theta + \rho_\theta \mathcal{L}_\theta) = 2\partial_\theta \rho_\theta. \tag{2.5}$$

This, in turn, results in a relation $\partial_\theta P(S = s|\theta) = \mathrm{Tr}\left[\Pi_s \partial_\theta \rho_\theta\right] = \mathrm{Re}(\mathrm{Tr}\left[\rho_\theta \Pi_s \mathcal{L}_\theta\right])$, which upon substituting into Eq. 2.2 leads to an alternative definition of the FI [33, 59]:

$$F(\theta) = \int \frac{\left(\mathrm{Re}\left(\mathrm{Tr}\left[\rho_\theta \Pi_s \mathcal{L}_\theta\right]\right)\right)^2}{\mathrm{Tr}[\Pi_s \rho_\theta]} ds. \tag{2.6}$$

Using the Cauchy-Schwarz inequality ($|\mathrm{Tr}[A^\dagger B]|^2 \leq \mathrm{Tr}[A^\dagger A]\mathrm{Tr}[B^\dagger B]$) with $A = \sqrt{\Pi_s}\sqrt{\rho_\theta}$ and $B = \sqrt{\Pi_s}\mathcal{L}_\theta\sqrt{\rho_\theta}$, the POVM normalisation condition and the cyclic property of the trace, it can then be shown that in general the QFI can be calculated via:

$$Q(\theta) = \mathrm{Tr}[\rho_\theta \mathcal{L}_\theta^2]. \tag{2.7}$$

2.3 Multi-parameter estimation

For completeness, we discuss the general settings of the multi-parameter estimation theory. The notation introduced in this section will be useful for the remainder of the thesis. The theory itself, however, will not be utilised to its full extent – we shall merely consider the single parameter approximation to multi-parameter estimation theory, i.e. by assuming that only of the parameters is unknown.

The task of the multi-parameter estimation theory is to estimate a set of parameters $\boldsymbol{\theta}$ encoded in a density matrix of a quantum system [42]. The main appeal of this theory lies in the possibility of estimating several unknown parameters at once within the same experimental set-up. This is particularly relevant for applications in imaging, microscopy and spectroscopy, which are inherently multi-parameter estimation problems

[66, 67]. Although the simultaneous multi-parameter estimation may offer significant improvement to precision, it suffers from a saturability problem; the multi-parameter QCRB will in general not be saturated due to the possible incompatibility of the optimal quantum measurements associated with different parameters [55, 57].

The multi-parameter estimation theory can be formulated by generalising the single parameter estimation theory, outlined in Sec. 2.2, to the case of various unknown parameters. This can be achieved with help of matrix formalism. Accordingly, solving a multi-parameter estimation problem amounts to finding an estimator $\hat{\boldsymbol{\theta}}$ whose precision quantifies the performance of the associated measurement and estimation strategy [33, 66]. As anticipated, the precision of $\hat{\boldsymbol{\theta}}$ is given by the mean square error $E\left[(\boldsymbol{\theta}-\hat{\boldsymbol{\theta}})(\boldsymbol{\theta}-\hat{\boldsymbol{\theta}})^T\right]$, which for unbiased estimators is equal to the covariance matrix $Cov(\hat{\boldsymbol{\theta}})$ [42, 46, 55, 57]. The covariance matrix contains information about the estimation errors of the various parameters (encoded in the diagonal elements), as well as the possible correlations between the estimation errors of the different parameters (encoded in the off-diagonal elements). In this case, the ultimate precision bound compatible with quantum mechanics is given by the multi-parameter QCRB, which is a matrix inequality that generalises the single parameter estimation theory. In more detail, the multi-parameter QCRB places a lower bound on the covariance matrix of an unbiased estimator of $\boldsymbol{\theta}$:

$$Cov(\hat{\boldsymbol{\theta}}) \geq \frac{1}{M} F(\boldsymbol{\theta})^{-1} \geq \frac{1}{M} Q(\boldsymbol{\theta})^{-1}, \tag{2.8}$$

where $F(\boldsymbol{\theta})$ is the Fisher information matrix (FIM) and $Q(\boldsymbol{\theta})$ is the QFIM [42, 57, 66]. Similarly, the FIM bounds the covariance matrix of an estimator for specific measurements. Note again that different choices of POVMs give different FI matrices, whilst the QFIM is always the same. As such, the QFIM quantifies the ultimate limit to multi-parameter estimation valid for every possible POVM and data analysis strategy. In multi-parameter estimation theory, the optimal estimators are therefore those with the FIM equal to the QFIM.

In practice, the knowledge of estimation performances of experimentally feasible measurements is helpful in discerning the best strategy for estimating unknown parameters [1]. For a given measurement strategy this is quantified in terms of the FIM, the elements of which are defined as [42, 57]

$$[F(\boldsymbol{\theta})]_{ij} = \int \frac{\left(\partial_{\theta_i} P(S = s|\boldsymbol{\theta})\right)\left(\partial_{\theta_j} P(S = s|\boldsymbol{\theta})\right)}{P(S = s|\boldsymbol{\theta})} ds. \tag{2.9}$$

As before, the conditional probabilities are obtained in terms of the chosen POVM, such that $P(S = s|\boldsymbol{\theta}) = \mathrm{Tr}[\Pi_s \rho_{\boldsymbol{\theta}}]$ [33]. The diagonal entries of the FIM then simply correspond to the FI of each individual parameter (as per Eq. 2.2). The QFIM can instead be calculated via the SLDs, the elements of which are defined as

$$[Q(\boldsymbol{\theta})]_{ij} = \frac{1}{2} Tr\left[\rho_{\boldsymbol{\theta}}\left(\mathcal{L}_{\theta_i}\mathcal{L}_{\theta_j} + \mathcal{L}_{\theta_j}\mathcal{L}_{\theta_i}\right)\right], \tag{2.10}$$

where $\mathcal{L}_{\theta_i}$ is the SLD for the parameter θ_i. Notice that this is simply a multi-parameter generalisation of Eq. 2.7; accordingly, the diagonal elements of the QFIM are equal to the QFI of a corresponding parameter.

Just like its single parameter analogue, the multi-parameter CRB (i.e. first inequality in Eq. 2.8) can in principle always be saturated [42, 66]. The optimisation of this bound can, for example, be achieved by the maximum likelihood estimator in the asymptotic limit [57]. However, as discussed above, the saturation of the multi-parameter QCRB (i.e. second inequality in Eq. 2.8) may not be possible in general due to the potential incompatibility of optimal measurements for different observables.

In single parameter estimation theory, the CRB and the QCRB can in general always be saturated [42]. In reality, however, the existence of optimal estimators and hence optimal measurements is not guaranteed [55, 57]. Alternatively, measurement schemes that rely on the asymptotic saturability of the classical and quantum precision bounds can be exploited [58]. For example, in the case of adaptive measurements these will converge to the optimal measurement as $M \to \infty$. The asymptotic saturation of the precision bounds can also be achieved by the maximum likelihood estimator, which for $M \to \infty$ returns a parameter value that is most likely to have generated the observed data.

2.3.1 Single parameter approximation to multi-parameter estimation theory

In this thesis, the optimal estimation of two unknown parameters – the linear and quadratic coupling constants – is examined. For simplicity, this is studied within the framework of single parameter estimation theory by assuming that only one of the parameters is unknown at a time. In general, this may overestimate the optimal precision with which the two parameters can be estimated simultaneously. However, these quantities can serve as a practical benchmark for assessing the performance of experimentally feasible measurements. In this sense, the performance of such measurements is never overestimated since it is judged against a benchmark that is harder to achieve, compared to the one given by the multi-parameter QET.

Indeed, assuming that only one of the parameters is unknown, say θ_i, reduces the multi-parameter estimation problem to single parameter estimation. In that case, the diagonal elements of the QFIM quantify the best possible estimation performance for each individual parameter, as per [1]

$$Var(\theta_i) \geq \frac{1}{M[Q(\boldsymbol{\theta})]_{ii}}. \tag{2.11}$$

Instead, the diagonal elements of the FIM are useful for quantifying the estimation errors of various experimentally feasible measurements. These can be equivalently quantified with the "single shot" relative error, which in accordance with the QCRB for $M = 1$, obeys the inequality

$$\frac{\Delta\theta_i}{\theta_i} \geq \frac{1}{\theta_i\sqrt{[F(\boldsymbol{\theta})]_{ii}}} \geq \frac{1}{\theta_i\sqrt{[Q(\boldsymbol{\theta})]_{ii}}}. \tag{2.12}$$

A smaller relative error then implies that more information about a given parameter is available and the easier it is to estimate it. This shall be a central quantity used to assess the results in this thesis due to the relative error having a more immediate practical interpretation compared to the QFIM.

2.4 Quantum estimation for Gaussian models

Gaussian states are a popular choice of quantum states in quantum optics and optomechanics [46, 57]. The appeal of these states can be attributed to their simplicity, together with the ease of creating and manipulating them experimentally [61]. Gaussian states are also of particular interest in QET [56]. In fact, estimation theory specific to Gaussian models has recently been formulated. In this case, all of the information about the unknown parameters will be contained in the states' first and second moments.

The formulation of the multi-parameter QET of Gaussian states relies on the covariance matrix language, the general settings of which are outlined below. The analysis focuses on a system consisting of N bosonic modes described by a vector of quadratures $\mathbf{R} = (X_i, P_i, ..., X_N, P_N)$, the elements of which satisfy the commutation relations $[X_i, P_j] = i\delta_{ij}$ and $[X_i, X_j] = [P_i, P_j] = 0$ [1, 46, 69]. More compactly, the commutator between any two quadrature operators can be written in the matrix form as

$$W_{ij} = [R_i, R_j] = i\Omega_{ij}, \tag{2.13}$$

where Ω is a $2N \times 2N$ symplectic matrix [57, 59]:

$$\Omega = \begin{pmatrix} 0_N & \mathbb{1}_N \\ -\mathbb{1}_N & 0_N \end{pmatrix}. \tag{2.14}$$

Here, $\mathbf{W}$ denotes the matrix of commutators which, by construction, satisfies $\mathbf{W}^{\mathbf{T}} = -\mathbf{W}$. In this setting, the first moments $\mathbf{r}$ of a quantum state ρ form a vector of average values defined as

$$\mathbf{r} = \langle \mathbf{R} \rangle = \mathrm{Tr}[\rho \mathbf{R}], \tag{2.15}$$

while the second moments $\boldsymbol{\sigma}$ are embodied in the covariance matrix with elements

$$\sigma_{kl} = \frac{1}{2}\langle\{R_k, R_l\}\rangle - \langle R_k\rangle\langle R_l\rangle, \tag{2.16}$$

where $\{A, B\} \equiv AB + BA$ is the anticommutator. However, in order for $\boldsymbol{\sigma}$ to be a physical covariance matrix, it needs to be real-valued and satisfy the Robertson-Schrödinger uncertainty relation,

$$2\boldsymbol{\sigma} + \mathbf{W} \geq 0. \tag{2.17}$$

If it does, then it is automatically positive semi-definite; hence, there exists a quantum (Gaussian) state ρ, such that $\boldsymbol{\sigma}$ is given by Eq. 2.16. Conversely, all covariance matrices obtained from a quantum state ρ, as in Eq. 2.16, automatically satisfy Eq. 2.17. Indeed, the inequality (2.17) is the necessary and sufficient condition for $\boldsymbol{\sigma}$ to represent the covariance matrix of a Gaussian state.

Recall that the goal of the multi-parameter QET is to estimate a set of parameters $\boldsymbol{\theta}$ encoded in a density matrix of a quantum system (see Section 2.3) [42]. As noted previously, for a Gaussian state all of the information about the parameters of interest will be contained in its average values $\mathbf{r}$ along with its covariance matrix $\boldsymbol{\sigma}$ [56, 57]. Assuming that only one of the parameters is unknown at a time, the "best-case-scenario" estimation performance for each of the parameters may be quantified with the respective diagonal elements of the QFIM. In this specific example, the diagonal elements of the QFIM can be expressed as

$$[Q(\boldsymbol{\theta})]_{ii} = \left(\partial_{\theta_i}\mathbf{r}^T\right)\boldsymbol{\sigma}^{-1}\left(\partial_{\theta_i}\mathbf{r}\right) + 2\,Tr\left[\left(\partial_{\theta_i}\boldsymbol{\sigma}\right)\left(4\mathcal{L}_{\boldsymbol{\sigma}} + \mathcal{L}_W\right)^{-1}\left(\partial_{\theta_i}\boldsymbol{\sigma}\right)\right], \tag{2.18}$$

where $\mathcal{L}_{\boldsymbol{\sigma}}(\mathbf{A}) = \boldsymbol{\sigma}\mathbf{A}\boldsymbol{\sigma}$ and $\mathcal{L}_W(\mathbf{A}) = \mathbf{WAW}$ represent the superoperators, while the term $\left(4\mathcal{L}_{\boldsymbol{\sigma}} + \mathcal{L}_W\right)^{-1}$ refers to the pseudoinverse if the term inside the bracket is singular [55]. In this thesis, the first term shall be referred to as the "contribution due to the averages", whilst the second term the "contribution due to the covariances" towards each diagonal element of the QFIM [1]. This terminology is adopted for formal convenience as well as to guide the reader's intuition in the technical discussions to follow. Note, however, that this terminology simply refers to the origin of the dependence of the gradients with respect to the unknown parameters, i.e. a term's "name tag" does not exclude its inevitable dependence on both quantities.

While the diagonal elements of the QFIM quantify the ultimate limit to single parameter estimation (i.e. estimation of θ_i when all remaining parameters in a set $\boldsymbol{\theta}$ are known), the maximum precision of specific measurement strategies is controlled by the diagonal elements of the FIM (see Section 2.3.1) [42]. Moreover, given a set of unknown parameters $\boldsymbol{\theta}$, the performance of various measurement strategies in estimating $\boldsymbol{\theta}$ can be calculated (in the continuous outcomes case) by first computing the conditional probabilities $P(S = s|\boldsymbol{\theta}) = \mathrm{Tr}[\Pi_s\rho_{\boldsymbol{\theta}}]$, where $\Pi_s \geq 0$ is the POVM element corresponding to the outcome s of the chosen observable, and then computing the integral (2.9). Interestingly, in the case of Gaussian states, analytical solutions to this integral are possible for the relevant cases of quadrature measurements, i.e. measurements of quadrature operators X_i, P_i and their linear combinations [1]. Quadrature measurements of light can, for example, be implemented by homodyne detection techniques (i.e. projective measurements of canonical operators), whilst quadrature measurements of a mechanical object correspond to measurements of its position, momentum or linear combination thereof [59]. In the case of homodyne detection, the probability distribution associated with a measurement of $S_k \in \{X_i, P_i\}$ is given by

$$P(S_k = s_k|\boldsymbol{\theta}) = \frac{e^{-\frac{(s_k - r_k(\boldsymbol{\theta}))^2}{2\sigma_{kk}(\boldsymbol{\theta})}}}{\sqrt{2\pi\sigma_{kk}(\boldsymbol{\theta})}}, \tag{2.19}$$

where $r_k(\boldsymbol{\theta})$ is the average of the chosen quadrature and $\sigma_{kk}(\boldsymbol{\theta})$ is the corresponding diagonal entry of the covariance matrix. For example, for a measurement of X_1, this corresponds to $r_1(\boldsymbol{\theta}) = \langle X_1 \rangle$ and the diagonal element $\sigma_{11}(\boldsymbol{\theta})$; similarly, for a measurement of P_1, this corresponds to $r_2(\boldsymbol{\theta}) = \langle P_1 \rangle$ and the diagonal element $\sigma_{22}(\boldsymbol{\theta})$. In this setting, an analytical solution to integral (2.9) exists and the diagonal elements of the FIM are explicitly given by

$$[F(\boldsymbol{\theta})]_{ii} = \frac{1}{2\sigma_{kk}(\boldsymbol{\theta})^2} \times \left[2\sigma_{kk}(\boldsymbol{\theta}) \left(\frac{\partial r_k(\boldsymbol{\theta})}{\partial \theta_i} \right)^2 + \left(\frac{\partial \sigma_{kk}(\boldsymbol{\theta})}{\partial \theta_i} \right)^2 \right]. \tag{2.20}$$

In the case of Gaussian states, when an optimal strategy for estimating $\boldsymbol{\theta}$ exists, it is then one with the FIM equal to the QFIM, i.e. $F(\boldsymbol{\theta}) = Q(\boldsymbol{\theta})$. Note, however, that the optimal measurement for Gaussian states is not necessarily Gaussian [60].

Chapter 3

Quantum Optomechanics

3.1 Introduction

Quantum optomechanics focuses on the interaction between the electromagnetic (EM) radiation and motional degrees of freedom of mechanical oscillators [2, 4, 71]. It is a relatively new research field with its roots going back to the 19th century. That was the time the mechanical properties of light started being investigated quantitatively. This was also when the radiation pressure force, the force responsible for the optomechanical interaction, was first theorised and later demonstrated experimentally.

The idea that light should exert pressure on material objects was first postulated by Kepler in the 17th century in his attempt to explain the specific shape of comet tails [2, 8, 9]. In particular, he noted that their tails were always pointing away from the Sun, which he proposed was due to the pressure exerted by the solar beams. The existence of radiation pressure was formally predicted by Maxwell in the 19th century and was later confirmed experimentally via light mill experiments [10].

The forces generated by radiation pressure are typically very weak, which makes it challenging to detect them experimentally [2, 5]. Braginsky and co-workers were the first people to investigate these effects in the context of interferometers [6]. Their experimental set-up featured a cavity with a harmonically bound end-mirror [4, 23]. The purpose of the cavity was to boost the otherwise weak radiation pressure forces, enhancing the light-matter interaction. Through these experiments, Braginsky demonstrated that radiation pressure forces give rise to an effect known as "dynamical backaction", which depending on the detuning, can either have a damping or amplifying effect on the mechanical motion. In this way, dynamical backaction could provide the means for controlling the motional degrees of freedom of the mirror in a predictable manner. This effect has been exploited in a variety of applications including gravitational wave detection and optomechanical backaction cooling [22].

Focusing on interferometers, Braginsky was also the first person to discuss quantum effects of the radiation pressure forces, and how they impose limits on the precision of mirror-displacement measurements [2, 23, 71]. Interferometers enable highly sensitive detection of the minute changes in the position of the mirror [72]. Their sensitivity, however, is limited by quantum noise which comes in two distinct forms: photon shot noise and quantum backaction [73, 74]. The photon shot noise is given by the statistical fluctuations in the rate of arrival of photons at the detector and dominates at lower laser powers [75]. As the laser power is increased, quantum backaction starts to dominate instead, arising from the quantum fluctuations of the EM field. These fluctuations are then converted into a random force and fed into the mirror, ultimately modifying its motion, and effectively causing the mirror to be heated. At the optimum laser power, the contributions from both the photon shot noise and quantum backaction are equal, and the SQL for measurement sensitivity is reached. This limit has important consequences for gravitational wave detectors, scanning probe microscopy and force sensing. Interestingly, however, the SQL is not the ultimate limit to measurement sensitivity and can in fact be overcome by reducing the quantum backaction, e.g. through the use of squeezed light.

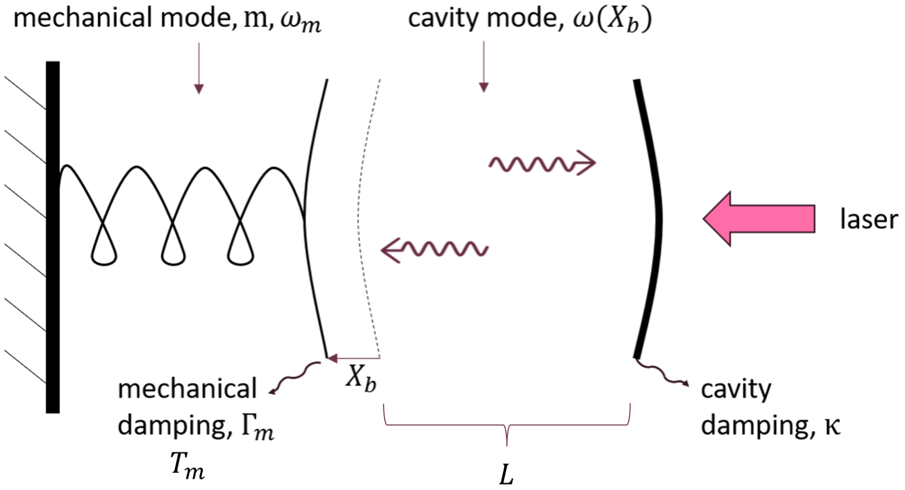

Figure 3.1: Schematic of an optomechanical set-up in Fabry-Perot geometry. The system consists of a cavity of bare length L and position-dependent frequency $\omega(X_b)$ which is composed of two mirrors, one fixed and the other movable mounted on a spring. To a good approximation, the movable mirror can be assumed to behave as a mechanical oscillator with frequency ω_m and effective mass m. Additionally, the interaction of the optomechanical system with its cavity and mechanical environments leads to cavity decay and mechanical damping of the oscillator at rates κ and Γ_m, respectively. The mechanical element is also characterised by a temperature T_m. The cavity mode is driven by an external laser. Adapted from [4, 82].

The photon shot noise was first observed experimentally in 2013 [4, 76]. However, no direct detection of the effect of quantum backaction on measurement sensitivity has been made as of yet. The main reason why quantum backaction remains challenging to measure is due to it being masked by thermal noise, the dominant source of noise of the oscillating mirror at finite temperatures [23, 77]. More in detail, at non-zero temperatures the mirror undergoes Brownian motion which effectively conceals the small motions generated by quantum backaction. Thus, to reach a regime where a range of quantum phenomena become clearly observable, the oscillating mirror has to be cooled close to its ground state [78]. This in itself is a challenge as in an effort to enter a quantum regime thermal occupation of the mirror needs to be brought to below unity, which in turn requires extremely low temperatures [74]. Interestingly, however, researchers have found ways in which dynamical backaction effects can be exploited to provide effective cooling of mechanical motion, all the way down to almost the ground state of the mechanical system.

The radiation pressure interaction can also give rise to the prospect of multistability [4, 23, 79, 80, 81]. In this phenomenon, the optomechanical system can have multiple steady states. Depending on the strength of the radiation pressure interaction, two (different) stable equilibrium positions for the mirror may exist, and when this happens the system is said to be “bistable” [4]. In the optical domain, bistability was first observed by Dorsel *et al.* using a Fabry-Perot interferometer.

The simplest optomechanical system consists of a single cavity mode interacting with a single mechanical mode and is realised, for example, in an optical cavity with a movable mirror [82]. Perhaps the most well-known example of an optomechanical set-up is a Fabry-Perot resonator, depicted in Fig. (3.1). Although alternative set-ups and geometries are also possible, the popularity of a Fabry-Perot type set-up is directly linked to how intuitive it is and how well it captures the main features of an optomechanical system. In optomechanics, a Fabry-Perot resonator consists of a cavity formed by two mirrors, one fixed and the other mounted on a spring [2]. To a good approximation, the behaviour of the movable mirror can be assumed to be that of a harmonic oscillator. Typically, the cavity and mechanical modes will not be isolated, but instead coupled to their respective environments. In that case, the interaction of the optomechanical system with its cavity and mechanical environments will lead to cavity decay, mechanical damping and heating of the oscillator. In most experiments, the cavity mode is also driven by an external laser. After having interacted with the optomechanical system, such laser light can be recollected and measured to gain information about the optomechanical interaction.

This chapter introduces the key theoretical models used in optomechanics. In Sec. 3.2, starting with its historical background, the Hamiltonian model of optomechanics is derived. This is achieved by considering the radiation pressure interaction between a single cavity mode and a mechanical oscillator. Next, in Sec. 3.3 the theory of open quantum systems is considered and a master equation description of an optomechanical system is identified. In comparison to the Hamiltonian model, this description constitutes a much more realistic representation of an optomechanical system since realistic quantum systems are unlikely to be isolated from their environments. Finally, Sec. 3.4 outlines the procedure for approximating the dynamics of driven-dissipative optomechanical systems via a bilinear master equation in the limit of strong cavity driving.

3.2 Hamiltonian models of optomechanics

A theoretical exploration of quantum optomechanical systems began during the 1990s [2]. Then, in 1995, the first exact Hamiltonian formalism to describe these systems was proposed by C. K. Law [40]. The derivation of the Hamiltonian model of optomechanics was facilitated by a previously established theory on the EM field quantisation for a one-dimensional cavity with variable length [83]. The analysis was based on a set-up featuring a cavity formed by two perfectly reflecting mirrors, one movable and the other one fixed. Starting with a classical description of the optomechanical interaction, C. K. Law used the equations of motions for the oscillating mirror and the EM field to construct a classical Hamiltonian model of the system. Following the canonical quantisation procedure, he was then able to derive the most rigorous, at the time, quantum Hamiltonian approach to modelling the mirror-field coupling.

Focusing on the simplest optomechanical system consisting of a single cavity mode interacting with a single mechanical mode, the quantum Hamiltonian, as derived by C. K. Law, to describe such system reads

$$H_{law} = \hbar\omega_m \frac{P_b^2 + X_b^2}{2} + \hbar\omega(X_b)\left(a^\dagger(X_b)a(X_b) + \frac{1}{2}\right), \tag{3.1}$$

where X_b and P_b are the dimensionless position and momentum operators of the movable mirror, $a(X_b)$ and $a^\dagger(X_b)$ are the position-dependent annihilation and creation operators for the cavity mode, whilst $\omega(X_b)$ is the position-dependent cavity frequency [1, 40]. To further simplify the C. K. Law's Hamiltonian model, here, it was additionally assumed that the behaviour of the movable mirror can be well approximated by that of a mechanical oscillator with effective mass m and frequency ω_m [2]. The position-dependent annihilation and creation operators for the cavity mode are defined as

$$a(X_b) = \sqrt{\frac{1}{2\hbar\omega(X_b)}}\,(\omega(X_b)q + ip)\,, \tag{3.2}$$

$$a^\dagger(X_b) = \sqrt{\frac{1}{2\hbar\omega(X_b)}}\,(\omega(X_b)q - ip)\,, \tag{3.3}$$

with q and p the canonical operators of the field [40, 82]. Also, here, the only non-trivial commutators read $[X_b, P_b] = i$, $[q, p] = i\hbar$ and $[a(X_b), a^\dagger(X_b)] = 1$. Note that the quadrature operators (depicted by capital letters) are conveniently defined to ensure their dimensionlessness, hence why $\hbar = 1$ in the commutator between X_b and P_b [4].

In order to better understand the nature of the optomechanical interaction, a comprehensive overview of the contributing terms in Hamiltonian (3.1) is required. The first term in this Hamiltonian only depends on the mirror's canonical variables and gives the bare energy of the mechanical mode [4, 40]. The second term instead describes the energy of the field as a function of the mirror's position. Such parametric dependence is the origin of the radiation pressure interaction in this type of model. It also implies that the radiation pressure interaction is intrinsically non-linear [2]. Besides, the parametric dependence of the field energy on the mirror's position may just as well be interpreted as a field-dependent correction to the mirror's trapping potential. Intuitively, the radiation pressure forces encoded in this Hamiltonian can induce a shift in the position of the movable mirror, which in turn leads to a change in the cavity length (hence in its frequency). This will consequently cause a change in the radiation pressure forces experienced by the mirror, et cetera.

The non-linear nature of the radiation pressure interaction hinders the possibility of studying optomechanical systems analytically [40]. For this reason, approximate models of optomechanics are typically used [2, 4]. In fact, C. K. Law was the first person to explore the linear approximation to Hamiltonian (3.1) in detail. He argued that if the mirror were bounded by a potential $\hbar\omega_m X_b^2/2$, it would perform small oscillations around its equilibrium position in which case the associated variations in cavity frequency would be tiny and the action of the radiation pressure forces on the mirror could simply be regarded as a small perturbation. With a generic optomechanical set-up in mind, in this setting, linearly expanding the cavity frequency and the field operators about $X_b = 0$ yields

$$a(X_b) \approx a + \frac{\omega'(0)}{2\omega_0} a^\dagger X_b, \tag{3.4}$$

$$\omega(X_b) \approx \omega_0 + \omega'(0) X_b, \tag{3.5}$$

where $a \equiv a(0)$. Substituting these expansions into Hamiltonian (3.1) then gives

$$\begin{aligned} H_{lin} = {} & \hbar\omega_m \frac{P_b^2 + X_b^2}{2} \\ & + \hbar\left(\omega_0 + \omega'(0)X_b\right)\left(a^\dagger a + \frac{1}{2} + \frac{\omega'(0)}{2\omega_0}\left(a^{\dagger 2} + a^2\right) X_b + \frac{\omega'(0)^2}{4\omega_0^2} a a^\dagger X_b^2\right). \end{aligned} \tag{3.6}$$

The inclusion of the counter-rotating terms (i.e. $a^{\dagger 2} + a^2$) in this Hamiltonian means that the cavity photon number $n = a^\dagger a$ is not conserved, which poses significant computational challenges [82]. Fortunately, the contribution from the counter-rotating terms can be typically neglected on the assumption that the mechanical range of the movable mirror's motion is very small (e.g. on the scale of the average cavity length). Additionally, in standard optomechanical set-ups, the higher order terms $O(\omega'(0)^2 X_b^2/\omega_0^2)$ yield negligible contributions and can thus be ignored. As a result of these simplifications, the so-called "linear model"[1] of optomechanics is then recovered:

$$H_{lin} = \hbar\omega_m \frac{P_b^2 + X_b^2}{2} + \hbar\left(\omega_0 + \sqrt{2} g_1 X_b\right) \frac{Q^2 + P^2}{2}. \tag{3.7}$$

Here, the annihilation and creation operators for the cavity mode have been replaced by the amplitude and phase quadratures, defined as $Q = \left(a + a^\dagger\right)/\sqrt{2}$ and $P = -i\left(a - a^\dagger\right)/\sqrt{2}$, respectively, which satisfy the commutation relation $[Q, P] = i$. This quadrature formalism will be relevant in the upcoming chapters. The quadratic terms in Hamiltonian (3.7) give the energies of the mechanical and cavity modes, whilst the cubic term describes the linear in X_b mirror-field interaction. In this case, the strength of the optomechanical interaction has been quantified with the linear coupling strength, which for a generic set-up is defined as [1]

$$g_1 \equiv \frac{1}{\sqrt{2}} \omega'(0). \tag{3.8}$$

The factor of $\sqrt{2}$ will be convenient later on.

The linear model, although very simple, has proven extremely successful at describing the vast majority of optomechanics experiments thus far [2]. The success of this model is further aided by the fact that the optomechanical coupling strength is typically very small [4]; in standard optomechanics experiments, the optomechanical coupling strength is much smaller than the mechanical frequency, i.e. $g_1 \ll \omega_m$ [84]. For example, in [26], authors consider $g_1 = 2 \times 10^2$ Hz, whilst in [85], $g_1 = 3 \times 10^2$ Hz. In fact, the linear model is expected to remain valid provided that the displacement of the movable mirror is many orders of magnitude below the average cavity length, which is generally satisfied for optomechanical systems. However, the investigation led by Brunelli *et al.* revealed that this model hides some potential problems [89]. There, the linear coupling Hamiltonian

---

[1] Commonly, in literature, "linearised optomechanics" refers to a linearised Hamiltonian model achieved by expanding the cavity field: $a \rightarrow \alpha + \delta a$, where $\alpha = \langle a \rangle$ is the average intracavity optical coherent amplitude and δa the fluctuating term, valid for sufficiently strong driving [2, 4].

was found to be unbounded from below, leading to the emergence of (non-physical) negative energies at large photon numbers, with the consequence that a well-defined thermal state does not exist [82]. This problem becomes prominent in the ultra-strong coupling regime where the linear coupling strength and the mechanical frequency have the same orders of magnitude. More generally, these findings highlight the necessity for more refined models of optomechanics as ways of enhancing the optomechanical coupling are continually explored, and the potential of optomechanics as tools for high-accuracy applications such as Planck physics is investigated [1]. The next step beyond the linear approach is to expand the cavity frequency up to and including second order in X_b, leading to the so-called "quadratic model". In many cases, the inclusion of the extra term improves the accuracy of the Hamiltonian model and also fixes the unboundedness issue.

More explicitly, for the quadratic model of optomechanics the position-dependent cavity frequency is approximated by

$$\omega(X_b) \approx \omega_0 + \sqrt{2} g_1 X_b + g_2 X_b^2, \tag{3.9}$$

where

$$g_2 = \frac{1}{2}\omega''(0) \tag{3.10}$$

is the quadratic coupling strength for a generic optomechanical set-up [1]. Once again, the numerical factor of $1/2$ is chosen for later convenience. Here, g_2 quantifies the strength of the quadratic mirror-field interaction. In parallel with Eq. 3.7, the quadratic Hamiltonian reads

$$H_{quad} = \hbar\omega_m \frac{P_b^2 + X_b^2}{2} + \hbar\left(\omega_0 + \sqrt{2} g_1 X_b + g_2 X_b^2\right)\frac{Q^2 + P^2}{2}. \tag{3.11}$$

This type of coupling can, for example, be realised in the membrane-in-the-middle optomechanical system which allows for great flexibility in the choice of both linear and quadratic coupling strengths [4, 85]. The membrane-in-the-middle configuration is achieved by placing a thin dielectric membrane inside a Fabry-Perot cavity [86]. The behaviour of the membrane is then assumed to be that of a harmonic oscillator. Moreover, in this system, a purely quadratic coupling (corresponding to $g_1 = 0$) can be engineered by placing the membrane at a node or antinode of the intracavity field [88]. Also, in this case, the linear model can be recovered by simply setting $g_2 = 0$. As an important aside, the quadratic model does not include all second order corrections arising from the microscopic treatment of the radiation pressure (see Eq. 3.1). How important these corrections are depends on the specific parameter regime under investigation. Unsurprisingly, the system dynamics as described by this model are also much more difficult to study.

To give a concrete example, a Fabry-Perot cavity with a movable mirror on one end is briefly considered [4, 82]. In this special case, the position-dependent frequency is of the form

$$\omega(X_b) = \frac{\omega_0}{1 + \frac{\sqrt{2}x_{zp}X_b}{L}}, \tag{3.12}$$

where $x_{zp} = \sqrt{\hbar/2m\omega_m}$ is the ground state position uncertainty of the mechanical oscillator and L is the bare cavity length [2, 40]. In accordance with Eqs. 3.8 and 3.10, in this setting the linear and quadratic coupling strengths are given by $g_1 = \omega_0 x_{zp}/L$ and $g_2 = 2\omega_0 x_{zp}^2/L^2$, respectively [1]. Additionally, in a standard Fabry-Perot setting, x_{zp} is typically many orders of magnitude below L in which case the detection of the quadratic model corrections may be experimentally challenging. However, as discussed above, there are systems where this may be easier, e.g. the membrane-in-the-middle optomechanical system. Note also that here, the positivity of g_1 can be ensured through a redefinition of the positive direction of X_b.

3.3 Dissipative dynamics

In order to establish a realistic optomechanical model, one needs to additionally consider the effects of environment on the dynamics of the system [4]. For this reason, it is often convenient to model an optomechanical system as an open quantum system, i.e. a system that is coupled to a large number of external degrees of freedom that are beyond one's control [68]. This system-environment coupling introduces dissipation (or more generally, decoherence) the effects of which are typically studied via a master equation description [91, 92].

In quantum mechanics, the state of any quantum system can be described by a density matrix, which is a semi-positive, Hermitian matrix with trace equal to one [55, 68, 91]. In most open quantum system models, the global state of the system+environment is first considered [94]. Then, by tracing out the environmental degrees of freedom, an equation of motion for the reduced density matrix of the system alone can be obtained. Such reduced density matrix is typically governed by a master equation [91]. For a memoryless (or Markovian) environment (also known as bath), this master equation is of the Lindblad form

$$\dot{\rho}(t) = \mathcal{L}\rho(t), \tag{3.13}$$

where $\mathcal{L}$ is a time-independent generator of the dynamics [95]. The Markovian approximation ensures that the future evolution of the system is only dependent on its present state; it is justified when memory effects of the environment are very short-lived in comparison to the dynamical timescales of the system. In this case, the action of $\mathcal{L}$ on the reduced density matrix is of the general form:

$$\mathcal{L}\rho(t) = -\frac{i}{\hbar}[H, \rho(t)] + \sum_{ij} \frac{\gamma_{decoh,ij}}{2} \left[2R_i\rho(t)R_j - \{R_jR_i, \rho(t)\}\right]. \tag{3.14}$$

Note here that the above master equation has been written in terms of quadrature operators that satisfy $R_i^\dagger = R_i$. More generally, the dissipative part reads $2L\rho(t)L^\dagger - \{L^\dagger L, \rho(t)\}$, where L is the Lindblad (or jump) operator of the system. Also here, the first term in the master equation (3.14) describes the Hamiltonian contribution to time evolution of $\rho(t)$ with H denoting the Hamiltonian of the system. The second term is instead responsible for making the overall dynamics non-unitary with γ_{decoh} a matrix encoding decoherence rates of the open quantum system.

For a generic oscillator with frequency ω, a characteristic decoherence rate is defined as

$$\gamma_{decoh} = \gamma(2\bar{n} + 1) \tag{3.15}$$

where γ is the damping rate, $\bar{n} = 1/(e^{\hbar\omega/k_B T} - 1)$ is the mean occupancy of the oscillator, k_B is the Boltzmann constant and T is the temperature of the coupled thermal bath [4, 94]. Here, the term "thermal bath" refers to an environment that is in a thermal equilibrium state [68]. Accordingly, there are two contributions towards decoherence: thermal noise and vacuum noise, as prescribed by the first and second term of Eq. 3.15, respectively. Thermal noise leads to the loss of information from the system at a rate proportional to the temperature of the bath, whereas the vacuum noise arises from the zero-point fluctuations of the environmental degrees of freedom [23, 97, 98, 99]. Which of these noise types dominates can be determined by assessing the magnitude of $\bar{n}$. In particular, a vacuum noise dominated regime is recovered if $\bar{n}$ is less than unity.

More in detail, the focus of this study is a generic optomechanical system coupled to its environment. In this example, the mechanical and cavity modes are assumed to be interacting with their respective thermal baths at temperatures T_m and T_c, respectively [93]. The interaction of an optomechanical system with its cavity and mechanical environments leads to cavity decay and mechanical damping of the oscillator at rates κ and Γ_m, respectively [4]. In standard optomechanical set-ups featuring an optical cavity and a mechanical oscillator coupled to their respective room temperature thermal baths, temperature can be neglected for the cavity but not for the mechanics due to the different orders of magnitude in the relevant frequencies (i.e. $\bar{n}_c \simeq 0$, $\bar{n}_m \neq 0$) [2]. Indeed, for an optical cavity with bare frequency $\omega_0 \approx 3 \times 10^{15}$ Hz, and mechanical oscillator with frequency $\omega_m = 1 \times 10^{10}$ Hz coupled to their respective thermal baths at 300 K, the mean occupancies of light and mechanics are $\bar{n}_c \approx 10^{-35}$ and $\bar{n}_m \approx 4000$. This puts the cavity deep in the vacuum dominated regime, whilst the mechanical oscillator in the thermal noise dominated regime. In this case, temperature effects can thus only be neglected for the cavity. Additionally, in order to neglect thermal occupation in microwave cavities, cryogenic conditions are required. In summary, for an undriven optomechanical system described by a quadratic Hamiltonian (3.11), the master equation is assumed of the form

$$\dot{\rho}(t) = -\frac{i}{\hbar}[H_{quad}, \rho(t)] + \sum_{ij} \frac{\gamma_{decoh,ij}}{2} \left[2R_i\rho(t)R_j - \{R_jR_i, \rho(t)\}\right], \tag{3.16}$$

where the vector of quadrature operators is defined as

$$\mathbf{R} = (Q, P, X_b, P_b), \tag{3.17}$$

while the matrix of decoherence rates is:

$$\gamma_{decoh} = \begin{pmatrix} \frac{\kappa}{2} & -i\frac{\kappa}{2} & 0 & 0 \\ i\frac{\kappa}{2} & \frac{\kappa}{2} & 0 & 0 \\ 0 & 0 & \frac{\Gamma_m}{2}(2\bar{n}_m + 1) & -i\frac{\Gamma_m}{2} \\ 0 & 0 & i\frac{\Gamma_m}{2} & \frac{\Gamma_m}{2}(2\bar{n}_m + 1) \end{pmatrix}, \tag{3.18}$$

and $\bar{n}_m = 1/\left(e^{\hbar\omega_m/k_B T_m} - 1\right)$ is the mean occupancy of the mechanical oscillator [1].

In typical optomechanics experiments, the cavity will be coherently driven by an external laser field [2, 4]. This can be employed to both control and measure the properties of the system. The drive effectively enhances the optomechanical interaction by increasing the strength of the mirror-field coupling while also altering the essential character of the interaction through detuning.

A coherently driven optomechanical system may be described by the following effective Hamiltonian

$$H_{drive} = \hbar \left(\omega_0 + \sqrt{2} g_1 X_b + g_2 X_b^2 \right) \frac{Q^2 + P^2}{2} + \hbar \omega_m \frac{X_b^2 + P_b^2}{2} + \sqrt{2} \hbar \epsilon \cos(\omega_L t) Q, \qquad (3.19)$$

with ω_L the frequency of the driving laser and ϵ the drive amplitude [4, 100]. The explicit time-dependence of the driving term can then be removed by transforming into a frame rotating at the frequency of the incident laser. In this frame, the Hamiltonian of the driven system can be written as

$$H = \hbar \left(\Delta_0 + \sqrt{2} g_1 X_b + g_2 X_b^2 \right) \frac{Q^2 + P^2}{2} + \hbar \omega_m \frac{X_b^2 + P_b^2}{2} + \sqrt{2} \hbar \epsilon Q, \qquad (3.20)$$

where $\Delta_0 = \omega_0 - \omega_L$ is the detuning between the cavity and driving laser [1]. In the rotating frame, the dynamics of a driven-dissipative optomechanical system can be described by a Lindblad master equation:

$$\dot{\rho}(t) = -\frac{i}{\hbar}[H, \rho(t)] + \sum_{ij} \frac{\gamma_{decoh,ij}}{2} \left[2R_i \rho(t) R_j - \{R_j R_i, \rho(t)\} \right], \qquad (3.21)$$

with $\mathbf{R}$ and γ_{decoh} defined in Eqs. 3.17 and 3.18, respectively.

As previously mentioned, the radiation pressure forces responsible for the optomechanical interaction also lead to an effect known as "dynamical backaction", which arises as a consequence of finite cavity decay rate, κ [4, 23, 101]. Essentially, the finite κ gives rise to a component of the radiation pressure force which is out of phase with respect to the mechanical oscillatory motion, leading to an effective damping of the mechanical oscillator [2]. In that sense, the cavity field can be thought of as acting on the mechanical element like an additional effective thermal bath (although the associated effective temperature, set by quantum fluctuations in the cavity, is typically much lower than that of the true thermal bath). Depending on the detuning, dynamical backaction can either have a damping or anti-damping effect on the oscillator's motion.

The detuning is thus a deciding factor behind the type of behaviour exhibited by an optomechanical system [2, 4, 23]. Depending on its sign, three distinct regimes can be identified. In the resonant regime, corresponding to $\Delta_0 = 0$, the cavity acts as an oscillator-dependent interferometer and it is possible to use the cavity output light to perform a continuous measurement of the mechanical position. In this case, the radiation pressure interaction also leads to heating of the mechanical oscillator, while its damping rate remains unchanged. In this regime, the limit to the precision of mirror displacement measurement is imposed by the SQL, achieved by minimising the thermal noise of the oscillator. In order to reach the SQL, near ground state cooling of the mechanical environment is thus required. As this is not straightforward to achieve in practice, in many scenarios the SQL may be impossible to reach altogether. Interestingly, the $\Delta_0 \neq 0$ regimes provide a route for enhanced measurement precisions, beyond those set by the SQL. In the blue-detuned regime, corresponding to $\Delta_0 < 0$, an optomechanical system can become unstable as a result of the energy being (on average) transferred to it from the driving laser. Therefore, in this case, the cavity field has an anti-damping effect on the motion of the oscillator, which is most pronounced at the blue sideband, $\Delta_0 = -\omega_m$. Instead, in the red-detuned regime, corresponding to $\Delta_0 > 0$, the radiation pressure interaction introduces additional damping to the mechanical element. In this regime, the effective temperature of the mechanical oscillator can be significantly reduced, that is the weighted average of the true thermal temperature and the (generally much lower) backaction temperature arising from quantum fluctuations in the cavity; the weightings are given by the standard mechanical damping and the additional damping arising from the backaction. This cavity field-induced-cooling effect is most pronounced at the red sideband, $\Delta_0 = \omega_m$, and can be exploited to allow near ground state cooling of the mechanical oscillator.

3.4 Gaussian dynamics approximation

This section will demonstrate that given the right set of circumstances, alongside strong cavity driving, the dynamics of an optomechanical system can be approximately described by a master equation that is bilinear in the canonical operators [1]. In that case, the system admits a Gaussian steady state, which can be fully described by its first and second moments [46, 61].

3.4.1 General Gaussian formalism

We start by presenting the general Gaussian formalism that allows to treat efficiently the most general picture involving a quantum system described by a quadratic Hamiltonian, coupled linearly to its environment.

Indeed, for a generic quantum system (with jump operators that are linear in the canonical quadratures), the master equation describing the system-environment interaction will be of the general Lindblad form (3.14) with

$$H = \frac{1}{2}\sum_{ij} H_{ij} R_i R_j = \frac{1}{2}\mathbf{R}^T \mathbf{H} \mathbf{R} \tag{3.22}$$

the bilinear Hamiltonian and $\mathbf{H}$ the Hamiltonian matrix which, without the loss of generality, can be assumed to be a symmetric matrix ($\mathbf{H} = \mathbf{H}^T$) [59]. Here, Eq. 3.22 is the general expression for a strictly quadratic Hamiltonian.

As anticipated, a Gaussian steady state can in general be fully characterised by its first and second moments, which will now be encoded in the steady state averages $\mathbf{R}_0$ and the steady state covariance matrix $\bar{\boldsymbol{\sigma}}$ [59]. Symbolically, the average value of a generic observable A evolves according to

$$\frac{d}{dt}\langle A\rangle \equiv \mathrm{Tr}[\dot{\rho}(t)A] = \frac{i}{\hbar}\langle [H, A]\rangle + \langle \mathcal{D}^{\dagger}(A)\rangle, \tag{3.23}$$

with [1, 68]

$$\mathcal{D}^{\dagger}(A) = \sum_{ij} \frac{\gamma_{decoh,ij}}{2}(R_j[A, R_i] + [R_j, A]R_i). \tag{3.24}$$

Using the same convention, the equation of motion for the vector of first moments can be found:

$$\dot{\mathbf{R}}_0 = -\frac{i}{\hbar}\mathbf{W}\mathbf{H}\mathbf{R}_0 + \mathbf{W}\gamma_{\mathbf{A}}\mathbf{R}_0 \tag{3.25}$$

$$= \mathbf{B}^T\mathbf{R}_0, \tag{3.26}$$

where $\mathbf{W}$ is the matrix of commutators (3.43), $\mathbf{B}$ is the drift matrix and γ_{decoh} is a decoherence matrix with elements $\gamma_{decoh,ij}$ that has been conveniently decomposed into its symmetric and antisymmetric parts [59, 69]:

$$\gamma_{\mathbf{S}} = \frac{\gamma_{decoh} + \gamma_{decoh}^T}{2}, \tag{3.27}$$

$$\gamma_{\mathbf{A}} = \frac{\gamma_{decoh} - \gamma_{decoh}^T}{2}. \tag{3.28}$$

By definition, the steady state averages satisfy $\dot{\mathbf{R}}_0 = 0$. Instead, the covariance matrix evolves according to

$$\dot{\boldsymbol{\sigma}} = (-\frac{i}{\hbar}\mathbf{W}\mathbf{H} + \mathbf{W}\gamma_{\mathbf{A}})\boldsymbol{\sigma} + \boldsymbol{\sigma}(\frac{i}{\hbar}\mathbf{H}\mathbf{W} + \gamma_{\mathbf{A}}\mathbf{W}) + \mathbf{W}\gamma_{\mathbf{S}}\mathbf{W}. \tag{3.29}$$

As the steady state covariance matrix satisfies $d\bar{\boldsymbol{\sigma}}/dt = 0$, it is thus a solution of the

Lyapunov equation

$$\mathbf{B}^T\bar{\boldsymbol{\sigma}} + \bar{\boldsymbol{\sigma}}\mathbf{B} = \mathbf{C}, \tag{3.30}$$

where

$$\mathbf{B} = \frac{i}{\hbar}\mathbf{H}\mathbf{W} + \gamma_{\mathbf{A}}\mathbf{W}, \tag{3.31}$$

$$\mathbf{C} = -\mathbf{W}\gamma_{\mathbf{S}}\mathbf{W}. \tag{3.32}$$

The necessary conditions for $\bar{\boldsymbol{\sigma}}$ to represent a valid steady state covariance matrix of a Gaussian state have been discussed in Sec. 2.4. Moreover, in order for the quantum system to admit a Gaussian steady state, the drift matrix $\mathbf{B}$ needs to be stable (i.e. the real parts of the eigenvalues of $\mathbf{B}$ need to all be negative).

3.4.2 Bilinear approximation of optomechanics

In this section we dicuss the procedure for bilinearising the dynamics of a driven-dissipative optomechanical system within the framework of the quadratic model in the limit of strong cavity driving.

Intuitively, the main effect of a strong cavity drive is to displace the steady states of both, cavity field and mechanics [4]. Provided that the cavity is driven sufficiently strongly whilst the optomechanical couplings are weak enough, the system dynamics can be well approximated by a bilinear master equation where only small quantum fluctuations around the semi-classical steady state are considered [62].

In the special case of driven-dissipative optomechanics, the bilinearisation of Hamiltonian (3.20) can be achieved by transforming into a frame in which the steady state displacements vanish [4]. This corresponds to first, making the displacements $\mathbf{R} \to \mathbf{R} + \mathbf{R}_0$, where

$$\mathbf{R}_0 = (Q_0, P_0, x_0, p_0) \tag{3.33}$$

is the vector of steady state quadrature averages, and then neglecting terms that are beyond quadratic in the canonical operators [1]. Mathematically, this is equivalent to applying two displacement operators, $D(Q, P) = e^{iP_0Q - iQ_0P}$ and $D(X_b, P_b) = e^{ip_0X_b - ix_0P_b}$, to master equation (3.21), as per $\dot{\rho}(t) \to D^\dagger(Q, P)D^\dagger(X_b, P_b)\dot{\rho}(t)D(Q, P)D(X_b, P_b)$ [62, 70]. Here, x_0 and p_0 denote the average position and momentum of the mechanics in the steady state, whereas Q_0 and P_0 are the steady state displacements of the amplitude and phase quadratures, respectively. With help of relation (3.23), the following set of coupled equations for the steady state values of the system's first moments can be derived

$$Q_0 = \frac{-2\Delta_{eff}\epsilon}{\sqrt{2}\left(\Delta_{eff}^2 + \frac{\kappa^2}{4}\right)}, \tag{3.34}$$

$$P_0 = \frac{-\kappa\epsilon}{\sqrt{2}\left(\Delta_{eff}^2 + \frac{\kappa^2}{4}\right)}, \tag{3.35}$$

$$x_0 = \frac{\sqrt{2}g_1\omega_m\epsilon^2}{\left(\omega_m^2 + \frac{\Gamma_m^2}{4}\right)\left(\Delta_{eff}^2 + \frac{\kappa^2}{4}\right) + 2g_2\omega_m\epsilon^2}, \tag{3.36}$$

$$p_0 = \frac{\Gamma_m}{2\omega_m}x_0, \tag{3.37}$$

where $\Delta_{eff} = \Delta_0 - \sqrt{2}g_1x_0 + g_2x_0^2$ is the effective detuning. The non-linearity of these equations implies that multiple steady state solutions are possible in a phenomenon known as dynamical multistability [2, 81]. In terms of physical interpretation, this phenomenon is a consequence of the radiation pressure interaction; it arises from the cavity-field-induced shift in the position of the mechanical oscillator, which in turn leads to the elongation of the cavity and subsequent displacement of the amplitude and phase quadratures of the field [23]. Depending on the driving strength, up to five (quadratic model) or three (linear model) possible steady state solutions may exist. However, by adjusting the driving strength, the multistability can be completely avoided and the system can be restricted to a regime where it is stable, i.e. where a unique real solution to Eqs. 3.34-3.37 exists. Additionally, in accordance with Eq. 3.37, the displacement of the mechanical oscillator's momentum is caused by the mechanical noise. This can be seen as a "side effect" of some of the approximations underlying the modelling of mechanical damping in the master equation, and on physical grounds $p_0 \to 0$ would be expected. Fortunately, in realistic optomechanical set-ups the mechanical damping rate is typically much smaller than the mechanical frequency (i.e. $\Gamma_m \ll \omega_m$) so that this (unphysical) displacement of the steady state mechanical momentum is minuscule in general.

Following the displacement of the canonical operators in the master equation (3.21), the displaced optomechanical Hamiltonian takes the form

$$\begin{aligned} H_D = &\frac{\hbar}{2}\Delta_{eff}(Q^2+P^2) + \hbar g_{eff} X_b(QQ_0+PP_0) + \frac{\hbar}{2}\omega_{eff}X_b^2 + \frac{\hbar}{2}\omega_m P_b^2 \\ &+ \frac{\hbar}{2}g_{eff}X_b(Q^2+P^2) + \frac{\hbar}{2}g_2X_b^2(Q^2+P^2+2QQ_0+2PP_0), \end{aligned} \tag{3.38}$$

where $g_{eff} = -\sqrt{2}g_1 + 2g_2x_0$ is the effective coupling strength, $\omega_{eff} = \omega_m + 2g_2|\alpha|^2$ is the effective mechanical frequency and $|\alpha|^2 \equiv (Q_0^2+P_0^2)/2$ is the steady state intracavity photon number [1, 4]. For the sake of clarity, here, terms that do not depend on the canonical operators have been neglected as they do not contribute towards the dynamics. In order to attain a bilinear form of this Hamiltonian, the leftover non-linear terms (i.e. terms that are beyond second order in quadrature operators) need to also be neglected. This, however, requires a careful consideration of their contributions to ensure that the remaining quadratic terms are the dominant ones. In the case of a linear model of optomechanics, recovered when $g_2 \to 0$, strong cavity driving (i.e. $|\alpha|^2 \gg 1$) is the necessary condition to achieving the bilinearised description of Hamiltonian (3.38) [62]. If this condition is satisfied, the third order non-linear term $\propto g_1X_b(Q^2+P^2)$ would generally have a negligible contribution in comparison to all other terms; hence, its exclusion would be justified. Instead, in the case of a quadratic model, the bilinearisation of Hamiltonian (3.38) is possible provided that the dominant non-linear term $\propto g_1X_b(Q^2+$

P^2) is small compared to the second order terms that depend on g_2. In general, the largest g_2-dependent bilinear term is the one proportional to $g_2|\alpha|^2$. All non-linear terms in Hamiltonian (3.38) can thus be neglected provided that the relation $g_2 \gg g_1/|\alpha|^2$ is satisfied, which effectively sets a constraint on the driving power. Note also that depending on the driving strength, the remaining g_2-dependent terms may or may not have negligible contributions. For example, at high drive strengths all quadratic terms should be kept to maximise the accuracy of the bilinear model. Instead, at lower drive strengths, where only the term proportional to $g_2|\alpha|^2$ should be kept, a numerical analysis reveals that the effect of the additional g_2-dependent contributions is so minuscule that their inclusion (or otherwise) has no visible effect on system dynamics. Accordingly, all bilinear terms can be kept provided that the condition $g_2 \gg g_1/|\alpha|^2$ is satisfied. In conclusion, for strong cavity driving and $g_2 \gg g_1/|\alpha|^2$ the dynamics of an optomechanical system can be approximated by a bilinear master equation description:

$$\dot{\rho}(t) = -\frac{i}{\hbar}[H_B, \rho(t)] + \sum_{ij} \frac{\gamma_{ij}}{2} \left[2R_i\rho(t)R_j - \{R_jR_i, \rho(t)\}\right], \tag{3.39}$$

where the Lindblad operators remain unchanged, while the Hamiltonian now takes the form

$$H_B = \frac{\hbar}{2}\Delta_{eff}(Q^2 + P^2) + \hbar g_{eff} X_b(QQ_0 + PP_0) + \frac{\hbar}{2}\omega_{eff} X_b^2 + \frac{\hbar}{2}\omega_m P_b^2. \tag{3.40}$$

Comparing with Eq. 3.22, in this case, the Hamiltonian matrix reads

$$\mathbf{H} = \begin{pmatrix} \hbar\Delta_{eff} & 0 & \hbar g_{eff} Q_0 & 0 \\ 0 & \hbar\Delta_{eff} & \hbar g_{eff} P_0 & 0 \\ \hbar g_{eff} Q_0 & \hbar g_{eff} P_0 & \hbar\omega_{eff} & 0 \\ 0 & 0 & 0 & \hbar\omega_m \end{pmatrix}. \tag{3.41}$$

Additionally, in this displaced frame of reference the steady state covariance matrix is given by

$$\bar{\boldsymbol{\sigma}} = \begin{bmatrix} \langle Q^2\rangle & \langle\frac{1}{2}\{Q,P\}\rangle & \langle QX_b\rangle & \langle QP_b\rangle \\ \langle\frac{1}{2}\{Q,P\}\rangle & \langle P^2\rangle & \langle PX_b\rangle & \langle PP_b\rangle \\ \langle X_bQ\rangle & \langle X_bP\rangle & \langle X_b^2\rangle & \langle\frac{1}{2}\{X_b,P_b\}\rangle \\ \langle P_bQ\rangle & \langle P_bP\rangle & \langle\frac{1}{2}\{X_b,P_b\}\rangle & \langle P_b^2\rangle \end{bmatrix}, \tag{3.42}$$

the explicit form of which can be found by solving the Lyapunov equation (3.30) with [69]

$$\mathbf{W} = \begin{pmatrix} 0 & i & 0 & 0 \\ -i & 0 & 0 & 0 \\ 0 & 0 & 0 & i \\ 0 & 0 & -i & 0 \end{pmatrix}, \tag{3.43}$$

$$\mathbf{B} = \begin{pmatrix} -\frac{\kappa}{2} & -\Delta_{eff} & 0 & -g_{eff}Q_0 \\ \Delta_{eff} & -\frac{\kappa}{2} & 0 & -g_{eff}P_0 \\ g_{eff}P_0 & -g_{eff}Q_0 & -\frac{\Gamma_m}{2} & -\omega_{eff} \\ 0 & 0 & \omega_m & -\frac{\Gamma_m}{2} \end{pmatrix}, \tag{3.44}$$

and

$$\mathbf{C} = \begin{pmatrix} -\frac{\kappa}{2} & 0 & 0 & 0 \\ 0 & -\frac{\kappa}{2} & 0 & 0 \\ 0 & 0 & -\frac{\Gamma_m}{2}(2\bar{n}_m+1) & 0 \\ 0 & 0 & 0 & -\frac{\Gamma_m}{2}(2\bar{n}_m+1) \end{pmatrix}. \tag{3.45}$$

In this particular example, assuming that the drift matrix $\mathbf{B}$ is stable, $\gamma_{decoh} \geq 0$ is the necessary and sufficient condition for $\bar{\boldsymbol{\sigma}}$ to represent the steady state covariance matrix of a Gaussian state.

The bilinear model of optomechanics that has just been derived is valid for generic values of detuning. Accordingly, by letting $\Delta_0 > 0$ or $\Delta_0 = 0$ in the above equations, a model applicable for the red-detuned and resonant cases, respectively, can be obtained [2, 4]. In each of these two cases, there exists a regime where a single real solution to Eqs. 3.34-3.37 occurs and a system is stable [1]. Moreover, for a given set of parameter values, a suitable range of drive strengths for which the system remains stable can be found using computational methods.

Blue detuning ($\Delta_0 < 0$) is a separate case [4]. In this case, the system exhibits a dynamical instability which eventually leads to periodic, self-induced mechanical oscillations [2, 102]. In the blue-detuned regime, the resulting steady state is a limit cycle, arising from the competition between amplification and non-linear detuning or damping. The bilinear model clearly fails to capture this non-linear behaviour of the optomechanical system, and as such it may not be applicable in this case.

Chapter 4

Parameter estimation in the linear model

4.1 Introduction

As previously discussed, quantum optomechanical systems are a consequence of the radiation pressure interaction between a cavity mode and a movable mirror [2, 4]. Unfortunately, the non-linear nature of this interaction hinders the possibility of studying these systems analytically, and approximate models of optomechanics are typically used instead [40]. Here, we focus on the linear model of optomechanics, which assumes a linear dependence of the cavity frequency $\omega(X_b)$ on the dimensionless position of the movable mirror, X_b. As discussed in Sec. 3.2, this model is a sufficiently good approximation in the majority of modern optomechanics experiments, since the range of motion of the movable mirror is typically very small.

Within this framework, we exploit the application of local QET in driven-dissipative optomechanics [1]. The goal of this chapter is to investigate the achievable precision of the coupling constant g_1, adopting the linear model of optomechanics. The knowledge of the linear coupling constant is sufficient to accurately model the dynamics of optomechanical systems in many realistic experimental platforms [103].

In order to form a realistic description of a driven-dissipative optomechanical system, we assume open system dynamics. The interaction of the system with its environment will then lead to damping and decoherence, which can be described via a Lindblad master equation (see Sec. 3.3). The full model of a driven-dissipative optomechanical system will thus include dissipation, decoherence, driving as well as a non-linear Hamiltonian describing the light matter-interaction (see Sec. 3.3). As suspected, this complete model is difficult to solve, however by assuming sufficiently strong cavity driving the dynamics of the system can be approximated via a master equation that is bilinear in the canonical operators (see Sec. 3.4) [1]. This then leads to a Gaussian steady state which can be fully characterised by its first and second moments (see Sec. 3.4) [46, 61]. This steady state, with its explicit dependence on all of the model parameters, and in particular the unknown linear coupling strength, can subsequently be attacked via general closed-form expressions that are available for QET in Gaussian models [56]. The visual representation of the parameter estimation methodology for driven-dissipative optomechanics is shown in Fig. 4.1.

As discussed in Chapter 2, the ultimate limit to parameter estimation is set by the QCRB and may be quantified via the QFI [33, 42, 61]. The optimal measurement strategy for estimating g_1 is then one with the FI equal to the QFI. As anticipated, in this chapter we investigate how well the specific measurements of mechanical position X_b, field amplitude Q, mechanical momentum P_b and field phase P perform against the fundamental limits imposed by QET [1]. In our analysis, we focus on a regime where the multistability of the system can be completely avoided, which in turn sets an upper bound on the intracavity photon numbers considered. This "stable" region will also vary depending on the detuning between the cavity and driving laser, that is $\Delta_0 = \omega_0 - \omega_L$. For completeness, we study both the red-detuned and resonant regimes as for the two, there is a large region where

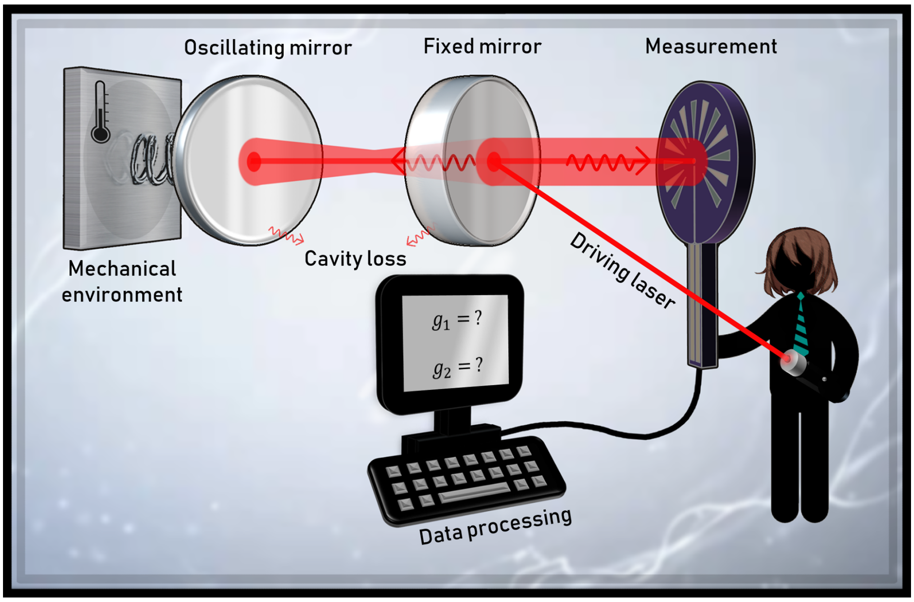

Figure 4.1: Schematic of the parameter estimation methodology for driven-dissipative optomechanics. We consider a driven-dissipative optomechanical system featuring a driven (by an external laser) and lossy (photons escaping the cavity) cavity and a damped mechanical oscillator. The mechanical support has low but finite temperature (leading to a non-zero thermal occupation number). The optomechanical coupling arises due to the radiation pressure on the movable mirror. Once the system has reached a steady state we measure an observable. We repeat the measurement many times to get the statistics. Finally, we process the data to find the best guess for the coupling parameters of interest. Reproduced from [1].

both unique steady state exists and the Gaussian formalism remains applicable.

Our main findings are the following: in the red-detuned regime (for the special case of $\Delta_0 = \omega_m$), we find that the best strategy for estimating the linear coupling constant is through a direct measurement of the mechanical position X_b. Instead, in the resonant regime ($\Delta_0 = 0$), which of the "realistic" measurements does best at estimating g_1 depends on both temperature and driving power. At higher temperatures, we find that the measurement of the field amplitude Q constitutes the best strategy for estimating the linear coupling constant for low-high driving powers. At sufficiently high intracavity photon numbers, the measurement of the field phase P performs better instead. In contrast, in the zero temperature scenario, we find that at low driving powers the best strategy for estimating the linear coupling constant is through a direct measurement of the mechanical position, whereas at high driving powers it is through a measurement of the field amplitude, or the field phase at sufficiently high $|\alpha|$.

As anticipated above, temperature has an important role in our predictions [1]. In particular, we examine three temperature scenarios: zero temperature ($T_m = 0$ K), low temperature ($T_m = 1$ mK) and "high" temperature ($T_m = 80$ mK) of the mechanical bath. In the red-detuned regime, the influence of temperature is most notable at lower intracavity photon numbers, where better estimation precision can be achieved at higher temperatures. This could be the consequence of the radiation-pressure-induced backaction cooling of the oscillator, which is most pronounced at higher tempratures. At higher intracavity photon numbers, the zero temperature scenario predicts a better estimation precision instead. Similarly, in the resonant regime, the effect of temperature on the estimation precision of the linear coupling constant is most pronounced at lower driving powers. In this region, the estimation precision of g_1 displays non-trivial dependence on temperature. In fact, at lower driving powers, the best precision is obtained at zero temperature, whilst the worst precision is obtained for $T_m = 1$ mK. Instead, at high intracavity photon numbers all temperature scenarios give qualitatively identical results.

The topic of single parameter estimation in quantum optomechanical systems was recently explored in works by Bernád, Sanavio and Xuereb [62, 103]. In [103], non-dissipative dynamics was assumed and it was found that better estimation precision of the linear coupling constant could be achieved at higher intracavity photon numbers. Our results support this claim for high driving powers in both red-detuned and resonant cases [1]. However, in the red-detuned regime we also find that for weaker drive strengths the observed behaviour becomes more complicated when finite-temperature effects are considered. In the resonant regime, although higher intracavity photon numbers clearly facilitate the estimation of the linear coupling constant, depending on the temperature the predicted QFI limits may not be achievable by simple quadrature measurements. In fact, at higher driving powers, the distance between the QFI limits and the measurements of Q, P and X_b increases. Recently, the same authors considered a driven-damped optomechanical system although using a somewhat different approach to ours [62]. In particular, the authors neglected the contribution of the steady state's first moments to the QFI, which, although a well-justified assumption for the model parameters adopted in their work, is not justifiable in general. In fact, our results to follow clearly demonstrate that there are experimentally accessible parameter regimes where the first moments come to dominate the QFI in both red-detuned and resonant regimes. Aside from considering both the contributions from the steady state's first and second moments towards the QFI, the thesis uniquely examines the performance of the measurements on the mechanics in estimating the linear coupling parameter. Typically, only the measurements on the light mode are considered as they are much easier to implement experimentally.

This chapter explores single parameter estimation in a driven-dissipative system, adopting the linear model of optomechanics. In Sec. 4.2, we adapt the multi-parameter QET introduced in Sec. 2.4 to the case of a single unknown parameter – g_1. Then in Secs. 4.3 and 4.4, we present and discuss the findings of our research for the red-detuned and resonant regimes, respectively.

4.2 Single parameter Gaussian state estimation

The parameter to be estimated – g_1 – first appears in Hamiltonian (3.7) where it quantifies the strength of the linear in X_b mirror-field interaction [40]. After approximating the master equation (3.21) to bilinear order under the assumption of strong cavity driving (see Sec. 3.4), the Hamiltonian of the system takes the bilinear form (3.40), or explicitly [1]

$$H_B = \frac{\hbar}{2}\Delta_{eff}(Q^2 + P^2) + \hbar g_{eff} X_b(QQ_0 + PP_0) + \frac{\hbar}{2}\omega_m X_b^2 + \frac{\hbar}{2}\omega_m P_b^2. \tag{4.1}$$

Here, the dependence on the linear coupling constant is embedded in the effective parameters, which in the limit $g_2 \to 0$ can be implicitly determined by the following set of equations: $g_{eff} = -\sqrt{2}g_1$ and $\Delta_{eff} = \Delta_0 - \sqrt{2}g_1 x_0$, where x_0 is the average steady state position of the mechanics (Eq. 3.36),

$$x_0 = \frac{\sqrt{2}g_1\omega_m\epsilon^2}{\left(\omega_m^2 + \frac{\Gamma_m^2}{4}\right)\left(\Delta_{eff}^2 + \frac{\kappa^2}{4}\right)}. \tag{4.2}$$

Due to the bilinear form of the master equation (3.39), in our approximated model of driven-dissipative optomechanics the system will admit a Gaussian steady state [1, 59]. All of the information about the unknown coupling parameter g_1 will thus be contained in the steady state averages $\mathbf{R}_0$ and the steady state covariance matrix $\bar{\boldsymbol{\sigma}}$, defined in Eqs. 3.33 and 3.42, respectively. Moreover, in single parameter estimation theory, the ultimate limit to parameter estimation may be quantified via the QFI, introduced in Chapter 2 [33, 42, 61]. Specifically for our coupling parameter g_1, the QFI is given by

$$Q(g_1) = \left(\partial_{g_1}\mathbf{R}_0^T\right)\bar{\boldsymbol{\sigma}}^{-1}\left(\partial_{g_1}\mathbf{R}_0\right) + 2\mathrm{Tr}\left[\left(\partial_{g_1}\bar{\boldsymbol{\sigma}}\right)\left(4\mathcal{L}_{\bar{\sigma}} + \mathcal{L}_W\right)^{-1}\left(\partial_{g_1}\bar{\boldsymbol{\sigma}}\right)\right], \tag{4.3}$$

where $\mathcal{L}_{\bar{\sigma}}(\mathbf{A}) = \bar{\boldsymbol{\sigma}}\mathbf{A}\bar{\boldsymbol{\sigma}}$ and $\mathcal{L}_W(\mathbf{A}) = \mathbf{WAW}$ represent the superoperators and $\mathbf{W}$ is the matrix of commutators (3.43) [55, 56]. Notice that the above expression is simply a single parameter analogue to Eq. 2.18. Accordingly, as discussed in Sec. 2.4, the first term in Eq. 4.3 is the contribution due to the averages, while the second term is the contribution due to the covariances towards the QFI.

In single parameter estimation theory, the QCRB (Eq. 2.3) sets the ultimate limit to the precision with which an unknown parameter can be estimated [33]. This precision bound can be equivalently expressed in terms of the single shot relative error, defined in

Eq. 2.12. In our specific example, the relative error satisfies the inequality [1]

$$\frac{\Delta g_1}{g_1} \geq \frac{1}{g_1\sqrt{Q(g_1)}} \equiv \delta g_1^{\text{min}}. \tag{4.4}$$

As the relative error is a dimensionless quantity, it allows for a fair comparison between parameters of different magnitudes or dimensions. This property will be particularly useful when re-introducing the quadratic coupling constant g_2 due to the varying magnitudes of the two coupling parameters.

As shown in Sec. 2.2, the estimation performance of various measurement strategies may be quantified via the FI [1, 33]. In our case, the FI measures the amount of information that a classical random variable s (the outcome of a quantum measurement) contains about the coupling parameter g_1. In congruence with Eq. 2.2, here, the FI is given by

$$F(g_1) = \int \frac{\left(\partial_{g_1} P(S = s|g_1)\right)^2}{P(S = s|g_1)} ds, \tag{4.5}$$

where $P(S = s|g_1)$ is the conditional probability of obtaining the value s when measuring the observable S, given that the parameter has the value g_1 [42, 57]. In our model of driven-dissipative optomechanics, analytical solutions to this integral exist for quadrature measurements, that is measurements of Q, P, X_b, P_b or their linear combinations. In these systems, the light quadratures, Q and P, can typically be measured using the homodyne detection scheme [59, 104]. In contrast, a direct measurement of the mechanical quadratures, X_b and P_b, could, for example, be achieved using another optical mode of the cavity. Following from Sec. 2.4, in this case, the probability distribution associated with a measurement of $S \in \{Q, P, X_b, P_b\}$ is given by

$$P(S = s|g_1) = \frac{e^{-\frac{(s - s_0(g_1))^2}{2\bar{\sigma}_{kk}(g_1)}}}{\sqrt{2\pi\bar{\sigma}_{kk}(g_1)}}, \tag{4.6}$$

where $s_0(g_1) \in \{Q_0, P_0, x_0, p_0\}$ is the steady state average of the chosen quadrature, while

$\bar{\sigma}_{kk}(g_1)$ is the corresponding diagonal entry of the steady state covariance matrix (i.e. $\bar{\sigma}_{11}$ for $S = Q$, $\bar{\sigma}_{22}$ for $S = P$, etc.). In this setting, an analytical solution to integral (4.5) is of the simple form

$$F(g_1) = \frac{1}{2\bar{\sigma}_{kk}(g_1)^2} \times \left[2\bar{\sigma}_{kk}(g_1) \left(\frac{\partial s_0(g_1)}{\partial g_1} \right)^2 + \left(\frac{\partial \bar{\sigma}_{kk}(g_1)}{\partial g_1} \right)^2 \right]. \tag{4.7}$$

The choice of a measurement strategy for estimating the coupling parameter g_1 is then optimal if the FI and the QFI are equal, i.e. $F(g_1) = Q(g_1)$.

Notice here that both the definitions of the QFI (Eq. 4.3) and the FI (Eq. 4.7) are dependent on the derivatives of the steady state covariance matrix and the averages with respect to the coupling parameter, g_1. Since the first and second moments are determined by the non-linear set of equations (3.34)-(3.37), which in general requires numerical methods to solve, we employ implicit differentiation to evaluate the derivatives in question. As all of the relevant quantities can now be conveyed in the numerical solutions to the above system of equations, our method allows for numerical differentiation to be avoided altogether. See Appendix A for detailed explanation of the use of implicit differentiation in our model.

4.3 Red-detuned regime

In this section, we explore the effects of temperature and driving on the estimation precision of the linear coupling constant g_1 in the red-detuned regime. Per our definition, the red-detuned regime is characterised by positive detuning values, i.e. $\Delta_0 > 0$ [1, 4]. Most commonly, as is the case also in this section, the detuning is chosen equal (or close to) the bare mechanical frequency; this is known as "red sideband driving". In our work, we consider the following parameter values: $\omega_m = 1.1 \times 10^7$ Hz, $m = 4.8 \times 10^{-14}$ kg, $\Gamma_m = 32$ Hz, $\Delta_0 = \omega_m$, $\kappa = 10^5$ Hz and $g_1 = 2 \times 10^2$ Hz. These values were inspired by [26] where near ground state cooling of the mechanical oscillator was achieved via the radiation-pressure-induced dynamical backaction.

As discussed in Sec. 3.4, in the linear model of optomechanics, strong cavity driving is the necessary condition to ensure that the Gaussian approximation is valid. This effectively places a lower bound on the drive amplitudes considered. In order to guarantee the stability of the system, we additionally need to restrict the range of drive amplitudes to a region where a single unique solution to the steady state averages (Eqs. 3.34-3.37) exists. Intuitively, we expect this region to be wider for a more stable system. With the two constraints in mind, for our set of parameter values, we select the following range of drive amplitudes as our study region: $10^8 \leq \epsilon \leq 3.8 \times 10^9$ Hz. In terms of the intracavity photon number, this corresponds to $80 \lesssim |\alpha|^2 \lesssim 1.2 \times 10^5$ (or $1.9 \lesssim \log_{10} |\alpha|^2 \lesssim 5.1$).

In order to investigate the effects of temperature on the estimation precision of the linear coupling constant, we examine three temperature scenarios: zero temperature ($T_m = 0$ K), low temperature ($T_m = 1$ mK) and "high" temperature ($T_m = 80$ mK) of the mechanical bath. In each case, we seek the best measurement strategy for estimating the coupling parameter, g_1. We start by evaluating the "global"[1] QFI, which corresponds to the best estimation precision achievable via a global measurement on the whole system [1]. In congruence with the QCRB, the calculated QFIs set the fundamental quantum limits to parameter estimation. By tracing out the mechanical or light modes, we can also extract the local QFIs, quantifying the ultimate limits to parameter estimation when only the light or mechanical modes are directly measurable. Comparing the local and global QFIs will then reveal how much information about the linear coupling parameter is contained in the reduced states of light and mechanics. Finally, we compare the global QFIs with the FIs of the realistic measurements of Q, P, X_b and P_b to help discern which of the experimentally common measurements constitute the best strategy for estimating the linear coupling constant in each temperature scenario.

---

[1] Note here that the quantities we refer to as the "global" and "local" QFIs are unrelated to the global and local QET, introduced in Chapter 2.

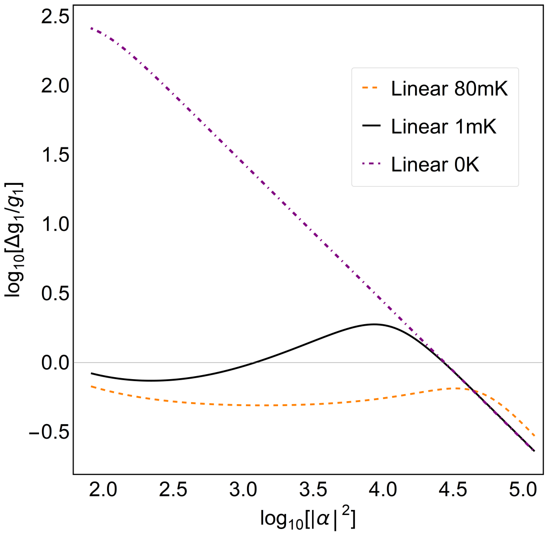

Figure 4.2: Log-log plot of the relative error bound on g_1 (as implied by the QFI) against the intracavity photon number, $|\alpha|^2$, as predicted by the linear model in the red-detuned regime in the zero temperature (purple dot-dashed line), low temperature (black line) and high temperature (orange dashed line) scenarios. Adapted from [1].

In Fig. 4.2 we investigate the effects of driving and temperature on the estimation precision of the linear coupling constant, g_1. According to this plot, the dependence of the relative error bound on g_1 (i.e. $\delta g_1^{\mathsf{min}} = 1/(g_1\sqrt{Q(g_1)})$) on temperature appears to be fairly complex; depending on the driving strength, temperature can either have an amplifying or hindering effect on the estimation precision of the linear coupling constant. In fact, there is a crossover around $\log_{10}|\alpha|^2 \sim 4.7$ (or $|\alpha|^2 \sim 5\times 10^4$) below which value the high temperature scenario offers the best estimation precision, whilst above it the best precision for estimating g_1 is found at lower temperatures. Additionally, in the non-zero temperature scenarios, $\delta g_1^{\mathsf{min}}$ displays non-monotic behaviour, the origins of which can be understood by studying how the contributions of the averages and variances to the QFI vary with temperature. Appropriately, in Fig. 4.3 we plot these contributions against the intracavity photon number for the three temperature scenarios. Here, $\tilde{g}_1-$QFI refers to the dimensionless QFI, defined as $Q(\tilde{g}_1) = \omega_m^2 Q(g_1)$ with $\tilde{g}_1 = g_1/\omega_m$ the dimensionless linear coupling constant [1]. The scope of the dimensionless parameters is to allow a simpler comparison between the linear and quadratic coupling constants due to their

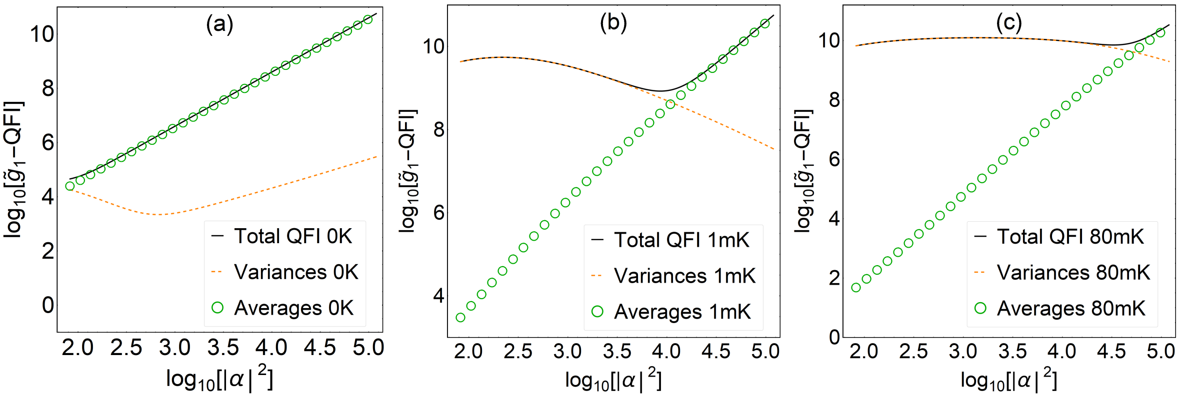

Figure 4.3: Log-log plots comparing the contributions from the variances (orange dashed line) and the averages (green circles) to the $\tilde{g}_1-$QFI in the linear model in the red-detuned regime (black line) in (a) the zero temperature scenario as well as the (b) $T=1$ mK and (c) $T=80$ mK cases.

differing dimensions. The dimensionless parameters also provide a simpler way to separate the contributions of the variances and averages to the QFI. Moreover, as shown in Fig. 4.3, the non-monotonic behaviour of $\delta g_1^{\mathrm{min}}$ in the non-zero temperature scenarios appears to be a result of the crossover of the dominance of the contributions from the variances to the averages. In the zero temperature limit no such crossover occurs; hence no local maximum is detected.

More in detail, Fig. 4.3 clearly demonstrates the contrasting behaviour of the contributions of the averages and variances. In particular, in all of the explored temperature scenarios, the contribution due to the averages increases monotonically with the intracavity photon number. As such, this contribution will always become dominant at sufficiently high $|\alpha|$. Interestingly, in the zero temperature scenario, the contribution due to the averages dominates at all intracavity photon numbers. Accordingly, in the zero temperature limit, the majority of information about the linear coupling constant is encoded in the averages. Instead, in the non-zero temperature scenarios, the contribution due to the variances is important and comes to dominate at lower intracavity photon numbers. This could be related to the radiation-pressure-induced backaction cooling of the oscillator, which makes the effective mechanical temperature, hence the steady state covariance matrix, strongly dependent on the coupling [1, 2, 4]. This effect also becomes more pro-

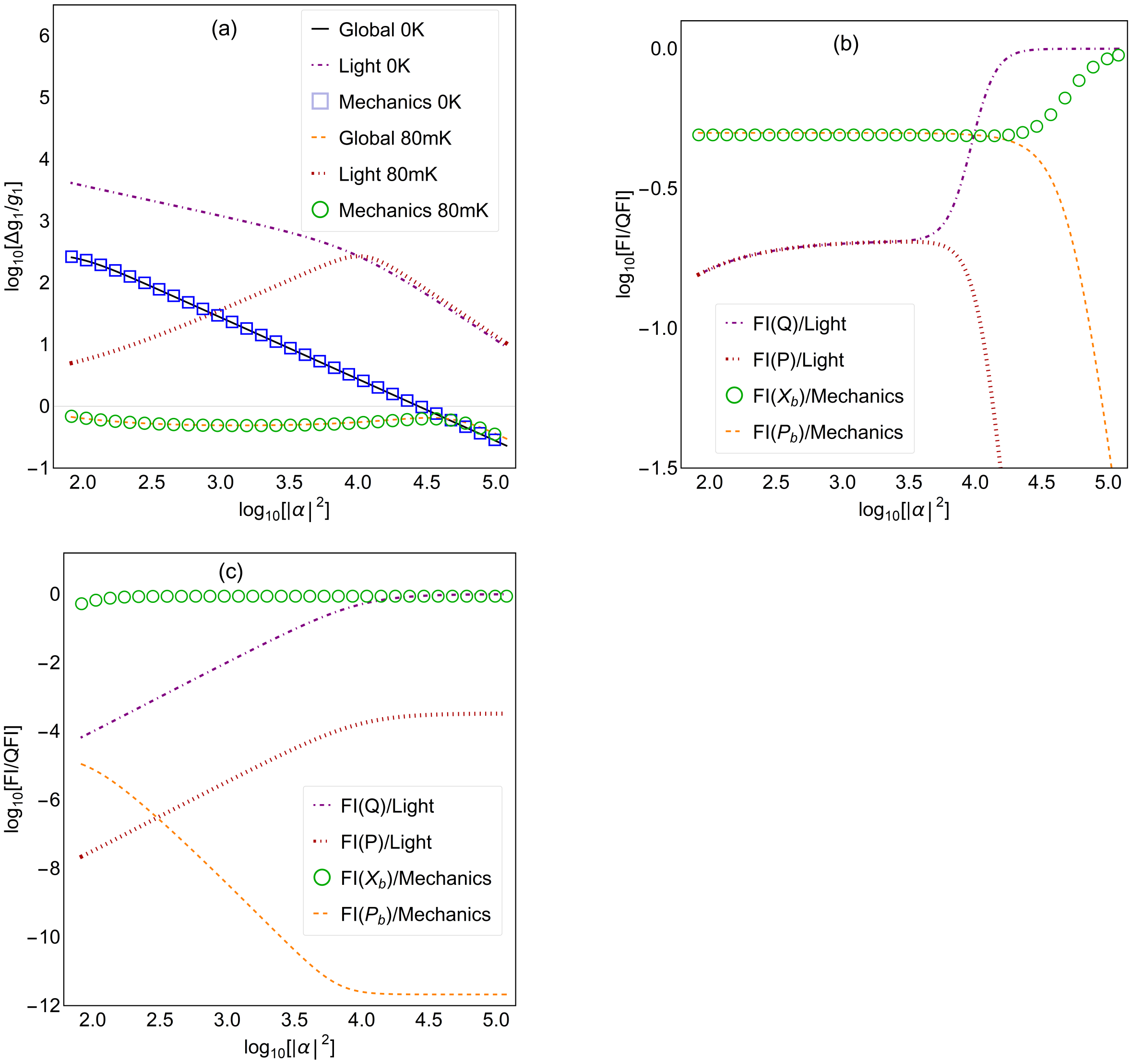

Figure 4.4: (a) Relative error bound on g_1 as a function of the intracavity photon number, $|\alpha|^2$, as implied by the global, light and mechanics QFIs in the red-detuned regime in the cases of zero temperature (black line, purple dot-dashed line, blue squares, respectively) and high temperature (orange dashed line, red dotted line and green circles, respectively). Adapted from [1]. (b) and (c) are the log-log plots of the ratios of the FI for the measurements of Q ($\mathsf{FI}(Q)$, purple dot-dashed line), P ($\mathsf{FI}(P)$, red dotted line), X_b ($\mathsf{FI}(X_b)$, green circles) and P_b ($\mathsf{FI}(P_b)$, orange dashed line) to light and mechanics QFIs against the intracavity photon number, $|\alpha|^2$, in the red-detuned regime for g_1 in the high and zero temperature scenarios, respectively.

nounced at higher temperatures as visualised by the widening of the region where the contribution due to the variances dominates.

In Fig. 4.4(a) we investigate how much information about the linear coupling constant is contained in the reduced states of light and mechanics versus the full system in the zero and high temperature scenarios. Clearly, in all of the explored cases, nearly all of the information about g_1 is encoded in the mechanical subsystem. This is better seen from Figs. 4.4(b) and (c). There, we plot the ratios of the FIs for the measurements of light and mechanical quadratures to light and mechanics QFIs, respectively, in the high and zero temperature scenarios. At 80 mK, for $\log_{10}|\alpha|^2 \lesssim 4.2$ the ratios of the FIs for the measurements of mechanical position and mechanical momentum to the mechanics QFI are both approximately equal to 0.5. In other words, in this region, the two measurements contribute roughly equally towards the mechanics QFI. At higher intracavity photon numbers, however, most of the mechanics QFI can be accessed via a measurement of mechanical position X_b. Instead, the ratios of the FIs for the measurements of field amplitude (Q) and field phase (P) to the light QFI are both approximately equal to 0.2 in the region $\log_{10}|\alpha|^2 \lesssim 3.6$. This may suggest that another measurement on light has a higher contribution towards the light QFI in this region. At sufficiently high intracavity photon numbers, however, all information encoded in light about the system can be accessed via a measurement of Q. In contrast, in the zero temperature limit, the FI for the measurement of mechanical position is essentially equal to the mechanics QFI at all intracavity photon numbers within our study range. Instead, the measurement of field amplitude only comes close to the light QFI at higher intracavity photon numbers. This again suggests that there might be another measurement on light that has a higher contribution towards the light QFI in the low driving region.

On the contrary, in optomechanics experiments, measurements are commonly performed on the light mode as it is generally more easily accessible. However, in accordance with our findings, to maximise the amount of information gained on the coupling parameter

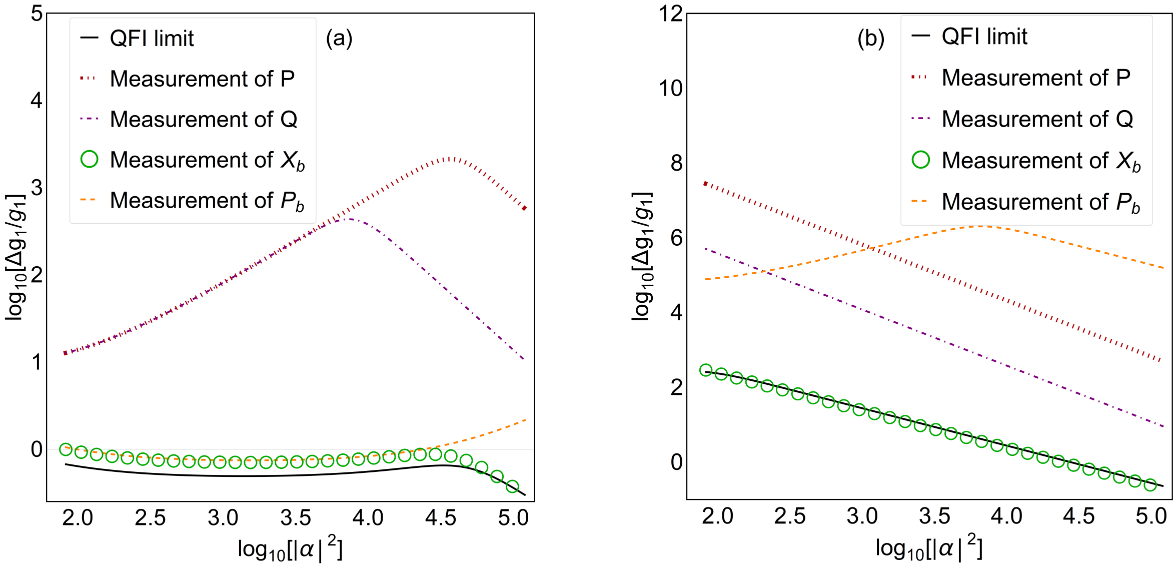

Figure 4.5: Log-log plots of the relative error bound on g_1 (as implied by the QFI) against the intracavity photon number, $|\alpha|^2$, in the red-detuned regime (black line) and the measurements of P (red dotted line), Q (purple dot-dashed line), X_b (green circles) and P_b (orange dashed line). (a) and (b) are for g_1 in the high and zero temperature scenario, respectively.

through a measurement, it may be beneficial to find ways of probing the mechanical mode more directly [1]. Additionally, both the light and mechanics QFIs reflect the monotonic or non-monotonic behaviour of the global QFI in the two temperature scenarios.

Then, in Fig. 4.5 we compare the performances of the realistic measurements of Q, P, X_b and P_b against the ultimate QFI limits in the zero and high temperature scenarios. Overall, in all of the explored cases, the mechanical position does best at estimating the linear coupling constant. Here, it is also evident that the QFI limit can only be approached in the zero temperature scenario. In addition, the behaviour of the realistic measurements is clearly temperature-dependent. In particular, the measurements of Q, P and X_b reflect the monotonicity, or otherwise, of the QFI limit in both temperature scenarios. The measurement of P_b, however, behaves very differently. In fact, in the high temperature scenario the measurements of the two mechanical quadratures perform very similarly, whilst in the zero temperature limit the measurement of X_b as well as the measurements of the light quadratures clearly outperform the measurement of the mechanical momentum.

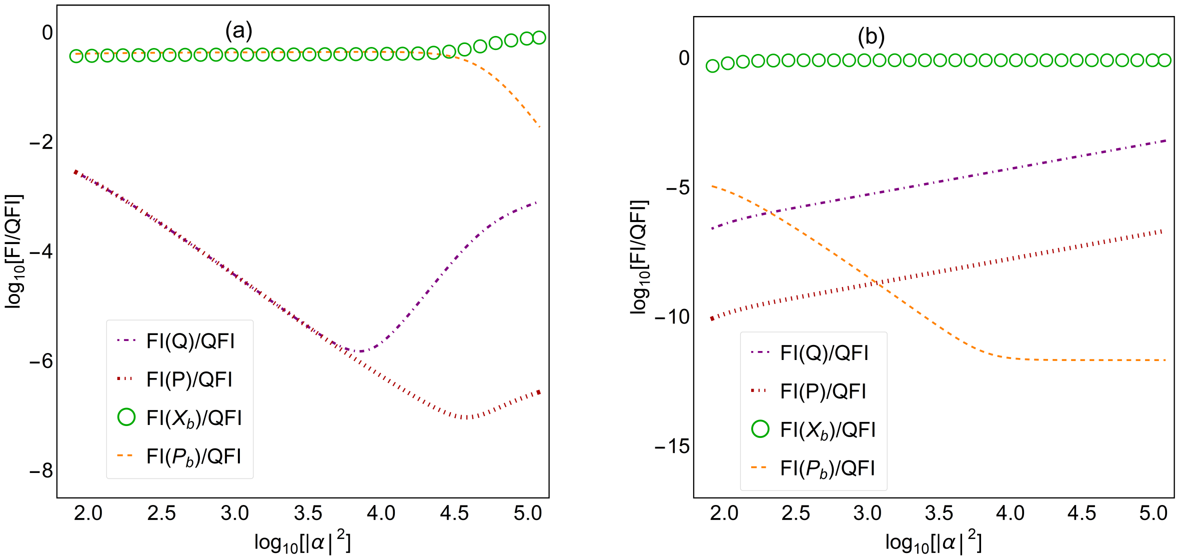

Figure 4.6: Log-log plots of the ratios of the FI for the measurements of Q ($\mathsf{FI}(Q)$, purple dot-dashed line), P ($\mathsf{FI}(P)$, red dotted line), X_b ($\mathsf{FI}(X_b)$, green circles) and P_b ($\mathsf{FI}(P_b)$, orange dashed line) to the QFI against the intracavity photon number, $|\alpha|^2$, in the red-detuned regime. (a) and (b) are for g_1 in the high and zero temperature scenario, respectively.

More in detail, in Fig. 4.6 we look at the ratios of the realistic measurements to the QFI in the zero and high temperature scenarios. In the high temperature scenario, both measurements of X_b and P_b contribute roughly 0.4 to the QFI in the region $log_{10}|\alpha|^2 \lesssim 4.15$. Beyond this region, approximately all information about the system can be accessed via a measurement of mechanical position. Instead, the realistic measurements on the light quadratures have minuscule contributions towards the QFI for the whole study region. Similarly, in the zero temperature scenario, all information about the system can roughly be accessed via the measurement of X_b at all intracavity photon numbers within our study range. This agrees well with our previous findings.

4.4 Resonant regime

For completeness, we additionally explore the estimation of the linear coupling strength in the resonant regime. Much like the red-detuned regime, in the resonant case there exists a large region where both unique steady state exists and the Gaussian formalism remains applicable [1]. In fact, the extent of this region can be explicitly determined by finding a range of drive amplitudes for which there exists a single, real solution for the average position of the mechanics, x_0 (Eq. 3.36). This, in turn, amounts to finding the discriminant of the cubic Eq. 3.36 with $\Delta_0 = 0$ (and $g_2 = 0$ for the linear model), and solving it for the drive amplitude, ϵ. In the resonant regime, the extent of the stable region can thus be determined by solving

$$\epsilon^4 = -\frac{\kappa^6(\Gamma_m^2 + 4\omega_m^2)^2}{27648 g_1^4 \omega_m^2}. \tag{4.8}$$

From Eq. 3.19 we also know that ϵ must be real, hence there is no solution to this equation. In other words, in the resonant regime, there exists a unique, real solution for the average position of the mechanics at all drive strengths. Accordingly, in this case, for a given set of parameter values, a suitable study region is only constrained by the strong cavity driving requirement, i.e. $|\alpha|^2 \gg 1$.

In order to allow for a comparison between the resonant and red-detuned regimes, we consider the same set of parameter values in both cases. However, to capture the most interesting features of the optomechanical system in this regime, we constrain our study region to $10^6 \leq \epsilon \leq 4 \times 10^8$ Hz. In terms of the intracavity photon number, this corresponds to $100 \lesssim |\alpha|^2 \lesssim \times 10^7$ (or $2 \lesssim \log_{10}|\alpha|^2 \lesssim 7$). This is a much wider region than that considered in the red-detuned case. As before, here, we explore the estimation of the linear coupling constant in the high, low and zero temperature scenarios. Our goal is to find the best strategy for estimating this coupling parameter in the resonant regime and how these results compare to our findings in the red-detuned case.

In Fig. 4.7(a) we explore the effects of temperature and driving on the estimation precision of the linear coupling constant, g_1. In contrast to the red-detuned case, in the resonant regime $\delta g_1^{\mathrm{min}}$ displays a straightforward dependence on the intracavity photon number.

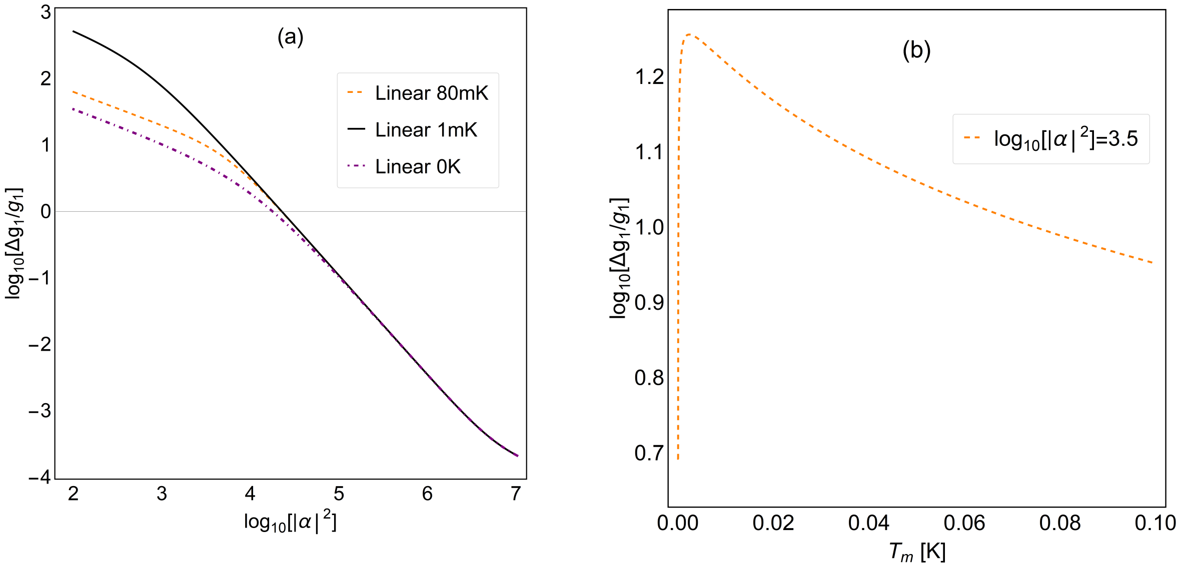

Figure 4.7: (a) Log-log plot of the relative error bound on g_1 (as implied by the QFI) against the intracavity photon number, $|\alpha|^2$, as predicted by the linear model in the resonant regime in the zero temperature (purple dot-dashed line), low temperature (black line) and high temperature (orange dashed line) scenarios. (b) Semi-log plot of the relative error bound on g_1 (as implied by the QFI) against the temperature of the mechanical bath, T_m, for the intracavity photon number $\log_{10}|\alpha|^2 = 3.5$.

Here, the relative error bound on g_1 decreases monotonically with the intracavity photon number over the whole study region. On the other hand, the dependence of $\delta g_1^{\min}$ on temperature is non-trivial at lower driving. This is illustrated in Fig. 4.7(b), which clearly demonstrates the non-monotonic dependence of $\delta g_1^{\min}$ on temperature at $\log_{10}|\alpha|^2 = 3.5$. In this case, the relative error bound on g_1 increases sharply with temperature in a region $T_m \lesssim 2$ mK, reaches a maximum at $T_m \approx 2$ mK and slowly declines at higher temperatures. At lower driving powers, the best precision for estimating g_1 is found at zero temperature, whilst the worst at $T_m = 1$ mK. Interestingly, at higher intracavity photon numbers the effect of temperature on the estimation precision becomes less important. In fact, for $\log_{10}|\alpha|^2 \gtrsim 5.3$, all temperature scenarios give qualitatively identical results.

The observed behaviour can be better understood by comparing the contributions of the variances and averages to the QFI in the three temperature scenarios. As visualised in Fig. 4.8, unlike in the red-detuned regime, in this case both contributions display

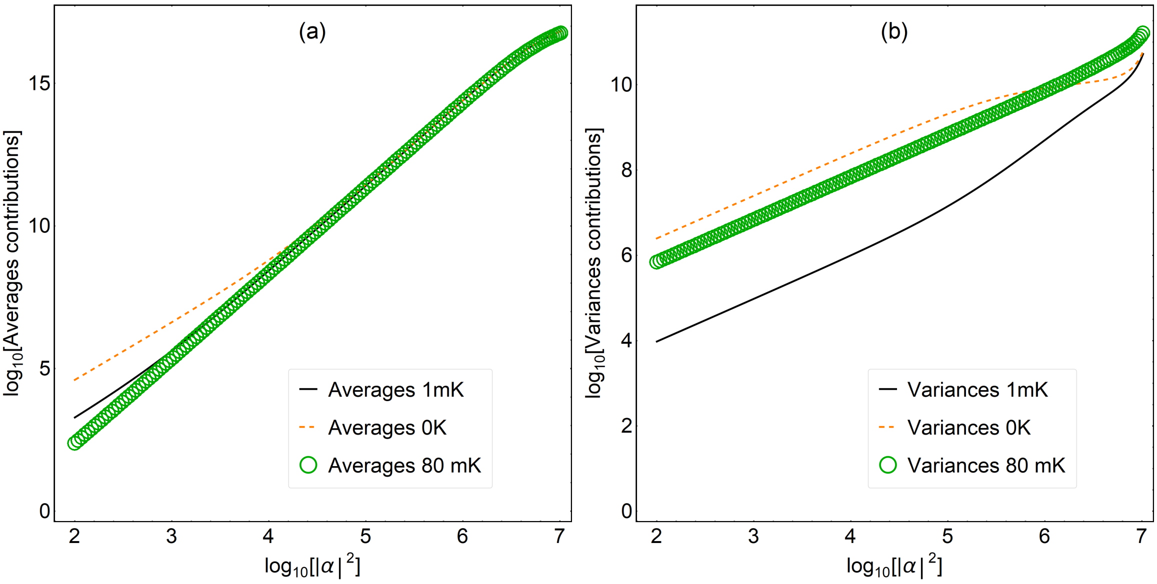

Figure 4.8: Log-log plots comparing the contributions from (a) the averages and (b) the variances to the $\tilde{g}_1-$QFI in the linear model in the resonant regime in the $T = 0$ K (orange dashed line), $T = 1$ mK (black line) and $T = 80$ mK (green circles) cases.

monotonic behaviour. Nevertheless, here, the crossover of the contributions from the variances to the averages is also observed. The location of this crossover point appears to be temperature-dependent. However, studying the origin of this temperature dependence is beyond the scope of this thesis, and is left for future work. At lower driving powers, the contribution due to the variances dominates. Interestingly, despite of its temperature dependence, this contribution is largest in the zero temperature scenario for the majority of the studied region. Instead, the contribution due to the averages dominates at large intracavity photon numbers. This, along with the temperature-independence of the averages, explains why the curves in Fig. 4.7(a) converge at large driving powers.

In Fig. 4.9 we investigate how much information about the linear coupling constant is encoded in the reduced states of light and mechanics versus the full system in the zero and high temperature scenarios. In comparison to the red-detuned regime, here, the observed behaviour is very different. Recall that in the red-detuned case, the majority of information about the linear coupling constant was contained in the mechanical subsystem. In the resonant regime, which of the two subsystems contains most information

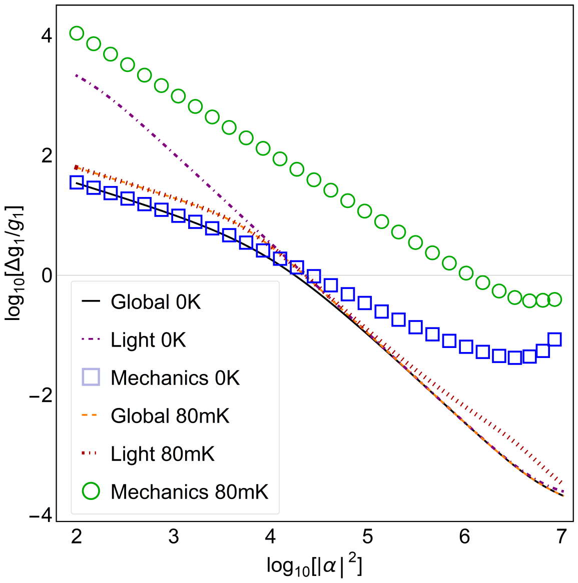

Figure 4.9: Relative error bound on g_1 as a function of the intracavity photon number, $|\alpha|^2$, as implied by the global, light and mechanics QFIs in the resonant regime in the cases of zero temperature (black line, purple dot-dashed line, blue squares, respectively) and high temperature (orange dashed line, red dotted line and green circles, respectively).

about g_1 depends instead on both temperature and driving power. Indeed, in the zero temperature scenario, there is a crossover at $\log_{10}|\alpha|^2 \approx 4.35$ below which value the majority of information about the linear coupling constant is encoded in the reduced state of the mechanics, whilst above it in the reduced state of light. Notice also that in this case, the g_1-QFI of the mechanics, or light, are only close to the global QFI in their respective regions of dominance. Instead, in the high temperature scenario, the majority of information about g_1 is contained in the light subsystem at all $|\alpha|^2$. Additionally, in this case, the g_1-QFI of the light subsystem is only close to the global QFI at lower intracavity photon numbers.

Finally, in Fig. 4.10 we compare the performances of the realistic measurements of Q, P, X_b and P_b against the ultimate QFI limits in the zero and high temperature scenarios [1]. Unlike in the red-detuned regime, in this case there is no single measurement that constitutes the best strategy for estimating the linear coupling constant over the whole study region or all temperatures. For example, in the high temperature scenario, there is a crossover at $\log_{10}|\alpha|^2 \approx 6.45$ below which value the best strategy for estimating g_1

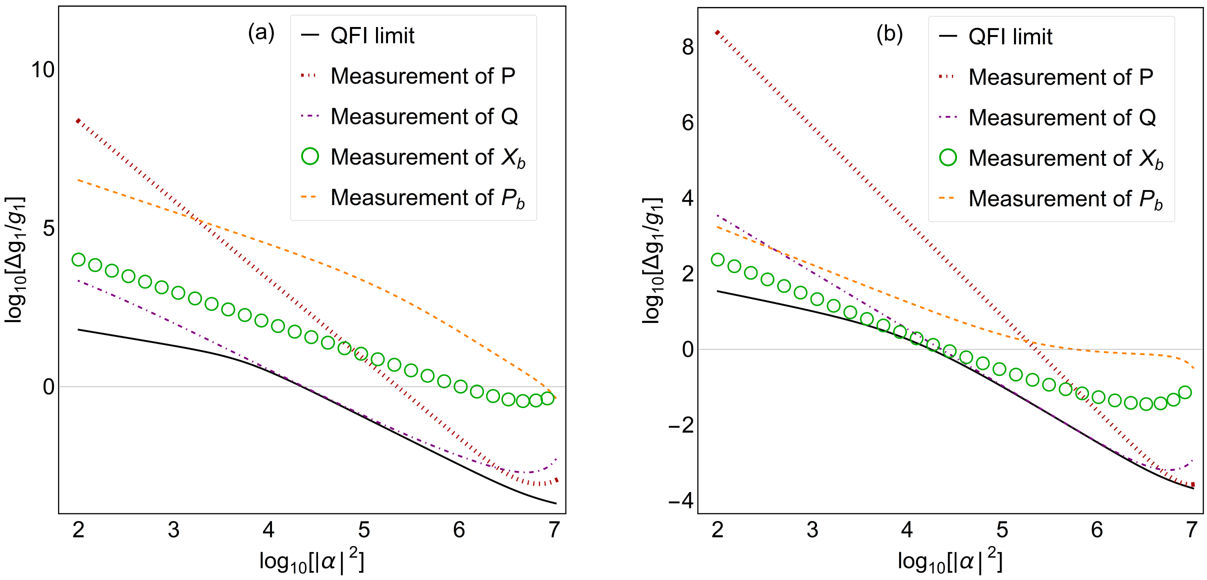

Figure 4.10: Log-log plots of relative error bound on g_1 (as implied by the QFI) against the intracavity photon number, $|\alpha|^2$, in the resonant regime (black line) and the measurements of P (red dotted line), Q (purple dot-dashed line), X_b (green circles) and P_b (orange dashed line). (a) and (b) are for g_1 in the high and zero temperature scenario, respectively.

is through a measurement of the field amplitude Q, whilst above it the measurement of the field phase P performs better. However, the ultimate limit to parameter estimation can only be approached by the measurement of Q for a limited range of drive strengths. Moreover, although the measurements of the light quadratures generally show a better agreement with the predicted QFI limit, at sufficiently low intracavity photon numbers, the measurement of the mechanical position X_b outperforms the measurement of P. Interestingly, the agreement between the QFI limit and the measurements of Q, P and X_b worsens with the intracavity photon number in the high driving regime, where these measurements start to display non-monotonic behaviour. In contrast, in the zero temperature scenario, the performance of the mechanical quadrature measurements is vastly improved. In fact, in the region $\log_{10}|\alpha|^2 < 4.35$, the measurement of the mechanical position constitutes the best strategy for estimating the linear coupling constant. Instead, in the high driving regime, we find that the best strategy for estimating g_1 is through a direct measurement of the field amplitude Q, whilst at sufficiently high $|\alpha|^2$ it is through a measurement of the field phase P. In this case, the predicted QFI limit can be approached by both the measurement of Q in the region $4.85 \lesssim \log_{10} |\alpha|^2 \lesssim 6.2$ and the measurement of P in a very limited range of drive strengths. Similarly to the high temperature scenario, here, the measurements of the light quadratures as well as the measurement of X_b start to display non-monotonic behaviour at sufficiently high intracavity photon numbers. Although the ultimate limit to parameter estimation clearly improves with driving, this limit is not attainable by simply choosing one quadrature of light and increasing the drive strength indefinitely.

Chapter 5

Parameter estimation beyond the linear model

5.1 Introduction

Although the linear model has been very successful at describing the vast majority of optomechanics experiments to date, with the potential of using optomechanics for ultra-high accuracy applications, this model will eventually need to be refined [2, 82].

This chapter explores the application of local QET in driven-dissipative optomechanics within the framework of the quadratic model. As discussed in Sec. 3.2, the quadratic model of optomechanics is obtained by expanding the cavity frequency up to and including second order in X_b [1]. The task of QET, in this case, is to find the best strategy for estimating both the linear (g_1) and quadratic (g_2) coupling constants [33]. Provided that the cavity is driven sufficiently strongly and the optomechanical couplings are weak enough, the bilinear master equation description remains applicable and the general expressions that are available for QET in Gaussian models can once again be employed.

Similarly to the previous chapter, here, we investigate the estimation of the linear and quadratic coupling constants in the red-detuned regime. Although a system described by the Hamiltonian that is consistent with the quadratic model will in general be more stable, for comparative purposes, we keep the parameter values and the study region the same as in Chapter 4. For completeness, here, we additionally explore the estimation of the quadratic coupling constant within the framework of the purely quadratic model. This model is obtained by removing the linear term in the expansion of the cavity frequency up to (and including) second order in X_b [4, 86]. This type of coupling can, for example, be realised in the membrane-in-the-middle optomechanical system in which the magnitudes of the linear and quadratic coupling constants can be independently adjusted by varying the position of the membrane. For comparative purposes, we adopt the same parameter values as in our investigation of the quadratic model. However, to capture all the interesting features of a system described by the purely quadratic model, in this case we consider a wider study region. Additionally, to gain understanding of the effect of the strength of the optomechanical interaction on the estimation precision of the quadratic coupling constant, here, we explore both $g_2 = 10$ Hz and $g_2 = 100$ Hz scenarios.

In the case of a quadratic model, we find that at low driving powers, the quadratic coupling constant is notably harder to estimate than the linear one [1]. This is somewhat intuitive since g_2 is associated with a higher order approximation of the optomechanical Hamiltonian in comparison to g_1. At higher drive strengths, however, the achievable estimation precisions of the two parameters become comparable. In the case of a purely quadratic model, we instead find that for low-high intracavity photon numbers, the estimation precision of the quadratic coupling constant improves significantly for $g_2 = 100$ Hz. At sufficiently high driving powers, however, the relative error bound on g_2 saturate at approximately $\sqrt{2}$ for both $g_2 = 10$ Hz and $g_2 = 100$ Hz scenarios.

In analogy to the previous chapter, here, we explore how well the specific measurements of mechanical position X_b, field amplitude Q, mechanical momentum P_b and field phase

P perform against the fundamental limits imposed by QET. In the case of a quadratic model, we find that in general the best strategy for estimating the coupling parameters is through a direct measurement of the mechanical position at all intracavity photon numbers within our study range [1]. Interestingly, in some parameter regimes, the measurement of the mechanical momentum performs just as well as the measurement of X_b. Instead, in the case of a purely quadratic model, all information about the quadratic coupling constant is contained in the mechanical subsystem. Additionally, we find that the measurement of P_b constitutes the best strategy for estimating this coupling parameter at all intracavity photon numbers within our study range. The measurement of X_b gives comparable estimation precision at low intracavity photon numbers, whereas at higher driving powers the relative error bound on g_2 increase with $|\alpha|^2$. Although the general behaviour of the two realistic measurements appears unchanged with the value set for g_2, the ultimate limits to the estimation precision of this coupling parameter can be approached at slightly lower intracavity photon numbers for $g_2 = 100$ Hz.

Here, we additionally investigate the influence of temperature on the estimation precision of the parameters of interest. Once again, we examine three temperature scenarios: zero temperature ($T_m = 0$ K), low temperature ($T_m = 1$ mK) and "high" temperature ($T_m = 80$ mK) of the mechanical bath. In the case of a quadratic model, we find that the influence of temperature on the estimation precision of the linear coupling constant is qualitatively identical to that discussed in Chapter 4: at lower driving powers better estimation precision can be achieved at higher temperatures, whilst at higher driving powers zero temperature is more advantageous instead [1]. Additionally, we find that higher temperatures favour the estimation precision of the quadratic coupling constant at all intracavity photon numbers within our study range. Instead, for a purely quadratic model, the relative error bound on g_2 shows weak dependence on temperature. Nevertheless, for low-high intracavity photon numbers, the highest estimation precision of g_2 can be achieved in the zero temperature limit. Also, in this region, the agreement between the realistic measurements and the ultimate limits set by the QFI improves slightly at higher temperatures.

The application of local QET in a quantum optomechanical system within the framework of the quadratic model was recently explored by Schneiter et al. [105]. Although using a different approach to ours, there a non-trivial dependence of the estimation precision of the coupling parameters on the temperature was also observed. In the case of purely quadratic optomechanics, local QET has been used to estimate the mechanical frequency, or equivalently the mass of the mechanical element [107]. Accurate knowledge of this parameter could, for example, be useful in mass precision detection.

This chapter explores quantum parameter estimation in a driven-dissipative system, adopting the quadratic and purely-quadratic models of optomechanics. In Sec. 5.2 we adapt the multi-parameter QET introduced in Sec. 2.4 to the case of two unknown parameters – g_1 and g_2. Starting with the quadratic model, in Sec. 5.3 we present and discuss the findings of our research for the red-detuned regime. Then, in Sec. 5.4 we discuss the validity of the bilinear master equation description in the case of a purely quadratic model and analyse the corresponding findings. Finally, in Sec. 5.5 we summarise our results. Note that the work covered in Sec. 5.2 is based on the research conducted in [1]. Sec. 5.4 instead features work that is fully original and yet unpublished.

5.2 Multi-parameter Gaussian state estimation

Adopting the quadratic model of optomechanics, the parameters to be estimated are the linear and quadratic coupling constants – g_1 and g_2. These parameters quantify the overall strength of the optomechanical interaction as well as the relative importance of the two types of coupling: linear and quadratic [1]. Methods to reliably estimate both coupling parameters would greatly benefit as their knowledge is essential for all applications of these systems.

The linear and quadratic coupling strengths were first introduced in Hamiltonian (3.11). Considering an optomechanical open system governed by Eq. 3.21 and taking the usual limit of strong cavity driving, the Hamiltonian of the system takes the bilinear form (3.40) instead, which we repeat here

$$H_B = \frac{\hbar}{2}\Delta_{eff}(Q^2 + P^2) + \hbar g_{eff} X_b(QQ_0 + PP_0) + \frac{\hbar}{2}\omega_{eff} X_b^2 + \frac{\hbar}{2}\omega_m P_b^2. \tag{5.1}$$

As before, the dependence on the two coupling constants is embedded in the effective parameters which can be determined by solving the coupled equations: $g_{eff} = -\sqrt{2}g_1 + 2g_2 x_0$, $\omega_{eff} = \omega_m + 2g_2|\alpha|^2$ and $\Delta_{eff} = \Delta_0 - \sqrt{2}g_1 x_0 + g_2 x_0^2$ with x_0 the average steady state position of the mechanics (Eq. 3.36),

$$x_0 = \frac{\sqrt{2}g_1\omega_m\epsilon^2}{\left(\omega_m^2 + \frac{\Gamma_m^2}{4}\right)\left(\Delta_{eff}^2 + \frac{\kappa^2}{4}\right) + 2g_2\omega_m\epsilon^2}. \tag{5.2}$$

As discussed in Sec. 3.4, Hamiltonian (5.1) (rewritten Eq. 3.40) is a valid approximation if both conditions $|\alpha|^2 \gg 1$ and $g_2 \gg g_1/|\alpha|^2$ are satisfied so that the system will admit a Gaussian steady state [1, 59]. Within these approximations, we recall that all information about the coupling parameters will be contained in the steady state averages $\mathbf{R}_0$ and the steady state covariance matrix $\bar{\boldsymbol{\sigma}}$, given in Eqs. 3.33 and 3.42, respectively.

As we now have two different parameters to estimate, the relevant theory is the multi-parameter estimation theory, introduced in Chapter 2. However, assuming that only one of these parameters is unknown, say g_i, the multi-parameter estimation problem reduces to single parameter estimation. Hence, as discussed in Sec. 2.3.1, the best estimation precision for each individual parameter may be quantified with the diagonal elements of the QFIM:

$$[Q(\mathbf{g})]_{ii} = \left(\partial_{g_i}\mathbf{R}_0^T\right)\bar{\boldsymbol{\sigma}}^{-1}\left(\partial_{g_i}\mathbf{R}_0\right) + 2Tr\left[\left(\partial_{g_i}\bar{\boldsymbol{\sigma}}\right)\left(4\mathcal{L}_{\bar{\sigma}} + \mathcal{L}_W\right)^{-1}\left(\partial_{g_i}\bar{\boldsymbol{\sigma}}\right)\right], \tag{5.3}$$

where $\mathbf{g} = (g_1, g_2)$, $\mathcal{L}_{\bar{\sigma}}(\mathbf{A}) = \bar{\boldsymbol{\sigma}}\mathbf{A}\bar{\boldsymbol{\sigma}}$, $\mathcal{L}_W(\mathbf{A}) = \mathbf{WAW}$ and $\mathbf{W}$ is the matrix of commutators (3.43) [33, 42, 55, 56, 61]. For succinctness, we will refer to $Q(\mathbf{g})_{11}$ as the "g_1-QFI" and $Q(\mathbf{g})_{22}$ as the "g_2-QFI". Comparing with the general form of this expression (Eq. 2.18), we call the first term the contribution due to the averages and the second term the contribution due to the covariances towards each diagonal entry of the QFIM [1, 56]. In this case, the QCRB (Eq. 2.8) takes the form analogous to Eq. 2.11, or explicitly

$$Var(\hat{g}_i) \geq \frac{1}{M[Q(\mathbf{g})]_{ii}}. \tag{5.4}$$

Additionally, as the linear and quadratic coupling constants will typically be several orders of magnitude apart, it may be preferable, at times, to measure the estimation precision with the single shot relative error, defined in Eq. 2.12. In our specific case, this relative error is implicitly defined by

$$\frac{\Delta g_i}{g_i} \geq \frac{1}{g_i\sqrt{[Q(\mathbf{g})]_{ii}}} \equiv \delta g_i^{\min}. \tag{5.5}$$

Similarly, the diagonal elements of the FIM quantify a classical limit to how well various measurement strategies can perform at estimating the unknown parameter [33]. In our example, the FIM provides a way for measuring the amount of information that a classical random variable s (the outcome of a quantum measurement) contains about the coupling parameters $\mathbf{g} = (g_1, g_2)$ [1]. In agreement with Eq. 2.2, we get the following expression for the diagonal elements of the FIM

$$[F(\mathbf{g})]_{ii} = \int_{-\infty}^{\infty} ds \frac{1}{P(S = s|\mathbf{g})}\left(\frac{\partial P(S = s|\mathbf{g})}{\partial g_i}\right)^2, \tag{5.6}$$

where $P(S = s|\mathbf{g})$ is the conditional probability of obtaining the value s when measuring the observable S [42, 57]. Once again, we select quadrature measurements, and specifically the measurements of Q, P, X_b and P_b, as our chosen observables. In that case, an analytical solution to this integral exists and is given by

$$[F(\mathbf{g})]_{ii} = \frac{1}{2\bar{\sigma}_{kk}(\mathbf{g})^2} \times \left[2\bar{\sigma}_{kk}(\mathbf{g}) \left(\frac{\partial s_0(\mathbf{g})}{\partial g_i} \right)^2 + \left(\frac{\partial \bar{\sigma}_{kk}(\mathbf{g})}{\partial g_j} \right)^2 \right], \tag{5.7}$$

where

$$P(S = s|\mathbf{g}) = \frac{e^{-\frac{(s - s_0(\mathbf{g}))^2}{2\bar{\sigma}_{kk}(\mathbf{g})}}}{\sqrt{2\pi\bar{\sigma}_{kk}(\mathbf{g})}}, \tag{5.8}$$

is the probability distribution associated with a measurement of $S \in \{Q, P, X_b, P_b\}$, $s_0(\mathbf{g}) \in \{Q_0, P_0, x_0, p_0\}$ is the steady state average of the chosen quadrature, whilst $\bar{\sigma}_{kk}(\mathbf{g})$ is the corresponding diagonal element of the steady state covariance matrix (i.e. $\bar{\sigma}_{11}$ for $S = Q$, $\bar{\sigma}_{22}$ for $S = P$, etc.) (for the general form of these expressions, see Eqs. 2.19 and 2.20). Also, as both the definitions of the diagonal elements of the QFIM and the FIM depend on the derivatives of the steady state covariance matrix and the averages with respect to the coupling constants, we will once again employ implicit differentiation to evaluate the derivatives in question, eliminating the need for numerical differentiation.

5.3 Red-detuned regime

Analogous to Sec. 4.3, here, we explore the influence of temperature and driving on the estimation precision of the linear and quadratic coupling constants. In this section, we additionally highlight any similarities and differences between the linear and quadratic optomechanical models. The differences between the two models emphasise the effect of corrections due to the quadratic term [1]. In order to make this comparison possible, we adopt the same parameter values and the same study region as in Sec. 4.3. Specifically, the parameter values we use are: $\omega_m = 1.1 \times 10^7$ Hz, $m = 4.8 \times 10^{-14}$ kg, $\Gamma_m = 32$ Hz, $\Delta_0 = \omega_m$, $\kappa = 10^5$ Hz and $g_1 = 2 \times 10^2$ Hz, whilst our chosen study region is $10^8 \leq \epsilon \leq 3.8 \times 10^9$ Hz (or $80 \lesssim |\alpha|^2 \lesssim 1.2 \times 10^5$ in terms of the intracavity photon number) [26]. Note that although we have chosen to keep the study region the same, for comparative purposes, for these parameter values the system described by the quadratic model will remain stable at all $|\alpha|$. The addition of the quadratic term thus results in a more stable system overall, in comparison to a system described by the linear model which exhibits bistability at finite ϵ. Moreover, our choice for the value of the quadratic coupling constant is motivated by the condition $g_2 \gg g_1/|\alpha|^2$, which ensures that the bilinear Hamiltonian (3.40) is valid (see Sec. 3.4); we let $g_2 = 10$ Hz to guarantee that this condition is satisfied at all intracavity photon numbers within our study range. Although this value is not consistent with the Fabry-Perot type set-up in [26], it can be realised in others, such as in the membrane-in-the-middle optomechanical system. In fact, [106] features a set-up in which the same order of magnitude value for the quadratic coupling constant was considered (i.e. $g_2 = 0.07 g_1$).

Here, we follow the same procedure as in Sec. 4.3. To summarise, we consider three temperature scenarios: zero temperature ($T_m = 0$ K), low temperature ($T_m = 1$ mK) and "high" temperature ($T_m = 80$ mK) of the mechanical bath. In each case, our goal is to determine the best strategy for estimating the linear and quadratic coupling constants. First, we evaluate the global QFIs, which in accordance with Eq. 5.4, quantify the "best-case-scenario" performance for the estimation of each of the coupling constants. Next, we calculate the local QFIs. By comparing these with the global QFIs, this will then tell us how much information about the linear and quadratic coupling constants is encoded in the reduced states of light and mechanics. Finally, we compare the global QFIs with the FIs of the measurements of Q, P, X_b and P_b to help us determine which of these measurements does best at estimating the linear and quadratic coupling constants in each temperature scenario.

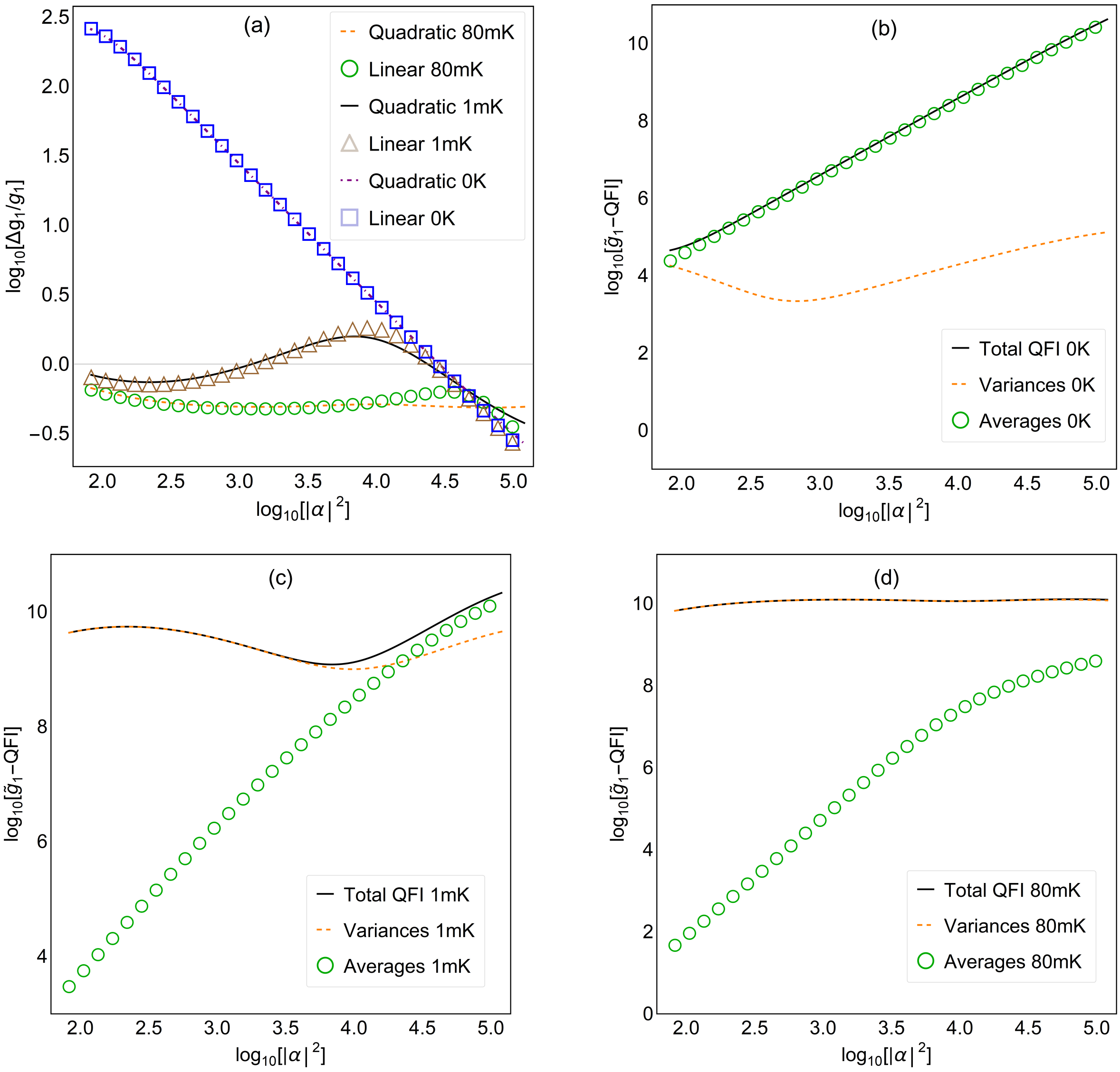

Figure 5.1: (a) Log-log plot of the relative error bound on g_1 against the intracavity photon number, $|\alpha|^2$. The plot compares linear and quadratic models in the zero temperature (blue squares and purple dot-dashed line, respectively), low temperature (brown triangles and black line, respectively) and high temperature (green circles and orange dashed line, respectively) scenarios. (b)-(d) Log-log plots comparing the contributions from the variances (orange dashed line) and the averages (green circles) to the $\tilde{g}_1$−QFI in the quadratic model (black line) for $\tilde{g}_1$ in (b) the zero temperature scenario as well as the (c) $T = 1$ mK and (d) $T = 80$ mK cases. Reproduced from [1]

In Fig. 5.1(a) we explore the influence of the higher order g_2 term, temperature and driving on the estimation precision of the linear coupling parameter, g_1. As anticipated, the relative error bound on g_1 (i.e. $\delta g_1^{\mathrm{min}}$) shows a complicated dependence on temperature [1]. Interestingly, however, the general behaviour of $\delta g_1^{\mathrm{min}}$ with temperature as predicted by the quadratic model matches that predicted by the linear model, i.e. up to around $\log_{10} |\alpha|^2 \sim 4.7$ (or $|\alpha|^2 \sim 5 \times 10^4$) the high temperature scenario offers the best estimation precision, whilst above this value the best precision for estimating g_1 is found at lower temperatures. For the quadratic model, non-monotonic behaviour of $\delta g_1^{\mathrm{min}}$ is also observed, although exclusively in the low temperature scenario. This is consistent with how the contributions of the averages and variances to the QFI vary with temperature in each of the three temperature scenarios, visualised in Figs. 5.1(b)-(d). As before, this non-monotonic behaviour appears to be a consequence of the crossover of the dominance of the contributions from the variances to the averages. Interestingly, in contrast to the linear model (see Fig. 4.3(c)), for the quadratic model no such crossover occurs in the high temperature scenario. Instead, in this case, the contribution due to the variances dominates at all intracavity photon numbers within our study range. The effect of the higher order g_2 term thus appears to be temperature-dependent; hence the contribution due to the variances is mainly affected. Additionally, for the quadratic model, $\delta g_1^{\mathrm{min}}$ remains roughly invariant with $|\alpha|^2$ in the high temperature scenario.

In Fig. 5.2(a) we investigate the influence of temperature and driving on the estimation precision of the quadratic coupling parameter, g_2. At low driving powers, the quadratic coupling constant is significantly harder to estimate than the linear one, as indicated by the considerably larger relative error bounds for g_2 than g_1 [1]. Interestingly, at high intracavity photon numbers, these error bounds become comparable, brought on by the fact that g_2 is boosted by a factor $|\alpha|^2$ in Hamiltonian (3.38). Additionally, in this case, higher temperatures appear to favour the estimation precision of g_2 for all driving strengths considered; according to Fig. 5.2(a), the lowest relative error bound on g_2 can

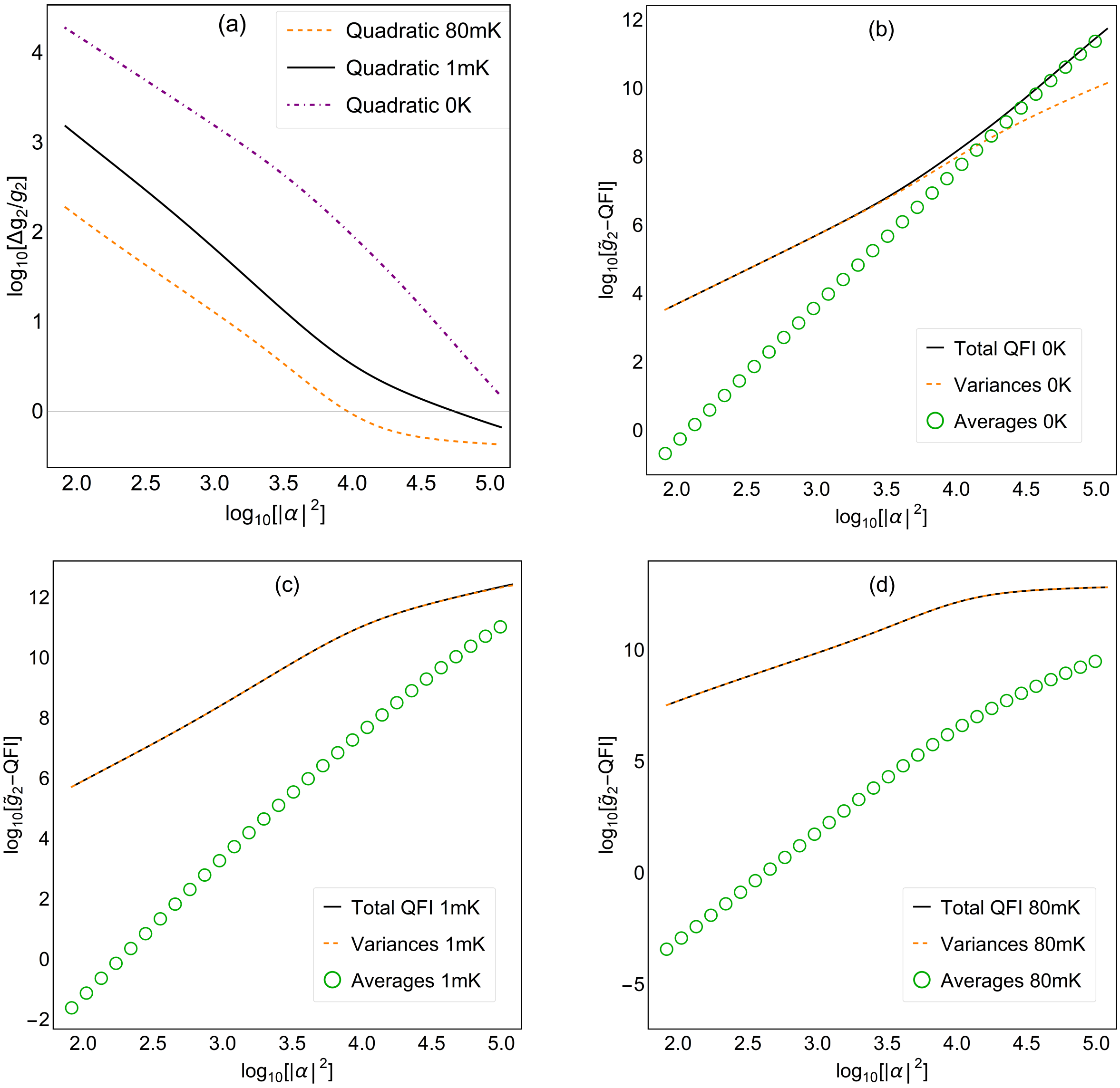

Figure 5.2: Log-log plot of the relative error bound on g_2 against the intracavity photon number, $|\alpha|^2$, as predicted by the quadratic model in the zero temperature (purple dot-dashed line), low temperature (black line) and high temperature (orange dashed line) scenarios. (b)-(d) Log-log plots comparing the variances (orange dashed line) and averages (green circles) contributions to QFI (black line) for $\tilde{g}_2$ at (b) zero temperature as well as the (c) $T = 1$ mK and (d) $T = 80$ mK cases. Reproduced from [1].

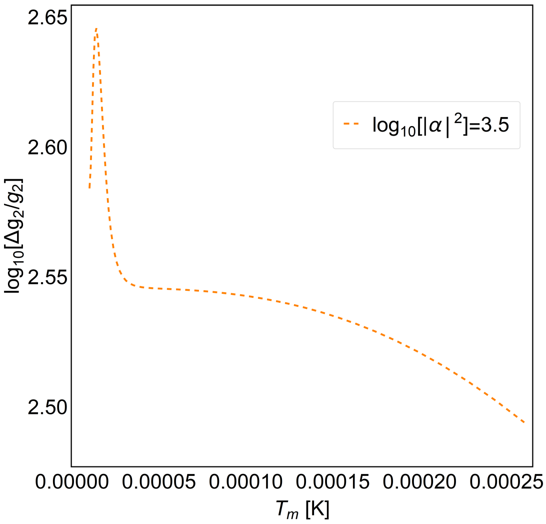

Figure 5.3: Semi-log plot of the relative error bound on g_2 (as implied by the QFI) against the temperature of the mechanical bath, T_m, for the intracavity photon number $\log_{10}|\alpha|^2 = 3.5$.

always be achieved in the high temperature scenario. This can be better understood by studying how the contributions of the averages and variances to the QFI vary with temperature in each of the three temperature scenarios, illustrated in Figs. 5.2(b)-(d). Recall that here, $\tilde{g}_i-$QFI refers to the dimensionless QFI, defined as $Q(\tilde{g}_i) = \omega_m^2 Q(g_i)$, where $\tilde{g}_i = g_i/\omega_m$ is the dimensionless linear ($i = 1$) or quadratic ($i = 2$) coupling constant. Indeed, in the low and high temperature scenarios, the temperature-dependent contribution due to the variances always dominates. In contrast, at zero temperature, the contribution due to the variances dominates at sufficiently low intracavity photon numbers before being overtaken by the contribution due to the averages at $\log_{10}|\alpha|^2 \sim 4.2$. Despite this crossover, no non-monotonic behaviour of δg_2^{min} is observed. Nevertheless, for all temperature scenarios, δg_2^{min} decreases monotonically with increasing drive.

The dependence of the relative error bound on g_2 on temperature is further investigated in Fig. 5.3. The plot clearly displays non-monotonic dependence of δg_2^{min} with temperature at $\log_{10}|\alpha|^2 = 3.5$. In this case, the relative error bound on g_2 increases sharply with temperature in a region $T_m \lesssim 1.4 \times 10^{-5}$ K, reaches a maximum at $T_m \approx 1.4 \times 10^{-5}$ K, declines sharply for $1.4 \times 10^{-5} \lesssim T_m \lesssim 3.7 \times 10^{-5}$ K, plateaus in a region $3.5 \times 10^{-5} \lesssim$

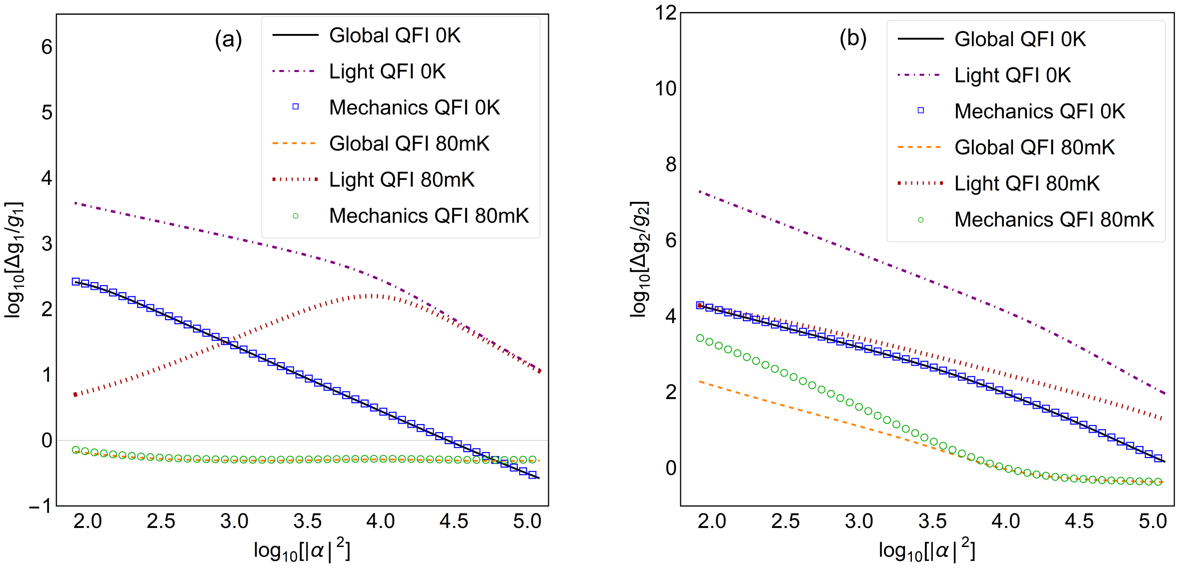

Figure 5.4: Relative error bounds on the coupling strengths (a) g_1 and (b) g_2, against the intracavity photon number, $|\alpha|^2$, as predicted by the global, light and mechanics QFIs in the zero temperature (black line, purple dot-dashed line, blue squares, respectively) and high temperature (orange dashed line, red dotted line and green circles, respectively) scenarios. Reproduced from [1].

$T_m \lesssim 6.3 \times 10^{-5}$ then slowly declines at higher temperatures. This explains why we observe the temperature to have a facilitating effect on the estimation precision of g_2 for the considered temperature scenarios (see Fig. 5.2). Interestingly, for all $T_m \gtrsim 1.4 \times 10^{-5}$ K, temperature appears to have an overall positive effect on the estimation precision of the quadratic coupling constant.

In Fig. 5.4 we compare the global and local QFIs for the linear (Fig. 5.4(a)) and quadratic (Fig. 5.4(b)) coupling constants. According to these plots, substantially more information about these parameters is encoded in the mechanical subsystem as compared to the light subsystem [1]. Accordingly, to optimise the information gained about either parameter through a local measurement, probing mechanical motion directly would be recommended.

More in detail, for g_1, the general behaviour of the mechanics and light QFIs matches that displayed in Fig. 4.4 for the linear model. Here also, the mechanics QFI closely matches the global QFI for all considered temperatures and drive strengths [1]. In contrast, in the case of g_2, the QFI of the mechanical subsystem is very close to the global QFI for all considered intracavity photon numbers in the zero temperature scenario as well as at sufficiently high drive strengths ($\log_{10}|\alpha|^2 \gtrsim 3.8$) for $T = 80$ mK. At lower drive strengths, there is instead a visible gap between the two QFIs in the high temperature scenario. Notice also that the g_2-QFI of the mechanical subsystem always outperforms the g_2-QFI of the light subsystem in both temperature scenarios.

Finally, in Fig. 5.5 we compare the performances of the realistic measurements of Q, P, X_b and P_b against the ultimate limits set by the g_1- and g_2-QFIs in the zero and high temperature scenarios. Generally, for all considered temperatures, the measurement of the mechanical position constitutes the best strategy for estimating the linear and quadratic coupling constants [1]. Here, it also clear that the g_1- and g_2-QFIs can only be approached in the zero temperature scenario, typically via a measurement of the mechanical position. These ultimate limits cannot be achieved at higher temperatures for either coupling parameter, although for g_2, the agreement between the g_2-QFI and the FI of the measurement of X_b improves at higher driving. At higher temperatures, the best strategy for estimating either coupling constant is instead through a direct measurement of the mechanical position or mechanical momentum. In contrast, in the zero temperature scenario, the corresponding ultimate limits to estimation precision can be approximately reached via a measurement of X_b for g_1 and g_2, or a measurement of P_b for g_2 in the low driving regime.

The temperature dependence of the higher order g_2 term is further demonstrated by comparing Figs. 5.5(a) and (c) with Fig. 4.5. In the zero temperature limit, the performance of the realistic measurements in estimating g_1 for the linear and quadratic models is qualitatively the same. Instead, in the high temperature scenario, the behaviour of the FIs and the g_1-QFIs for the two models is visibly different, particularly in the strong driving regime. Additionally, unlike in the linear model, in the case of the quadratic model either

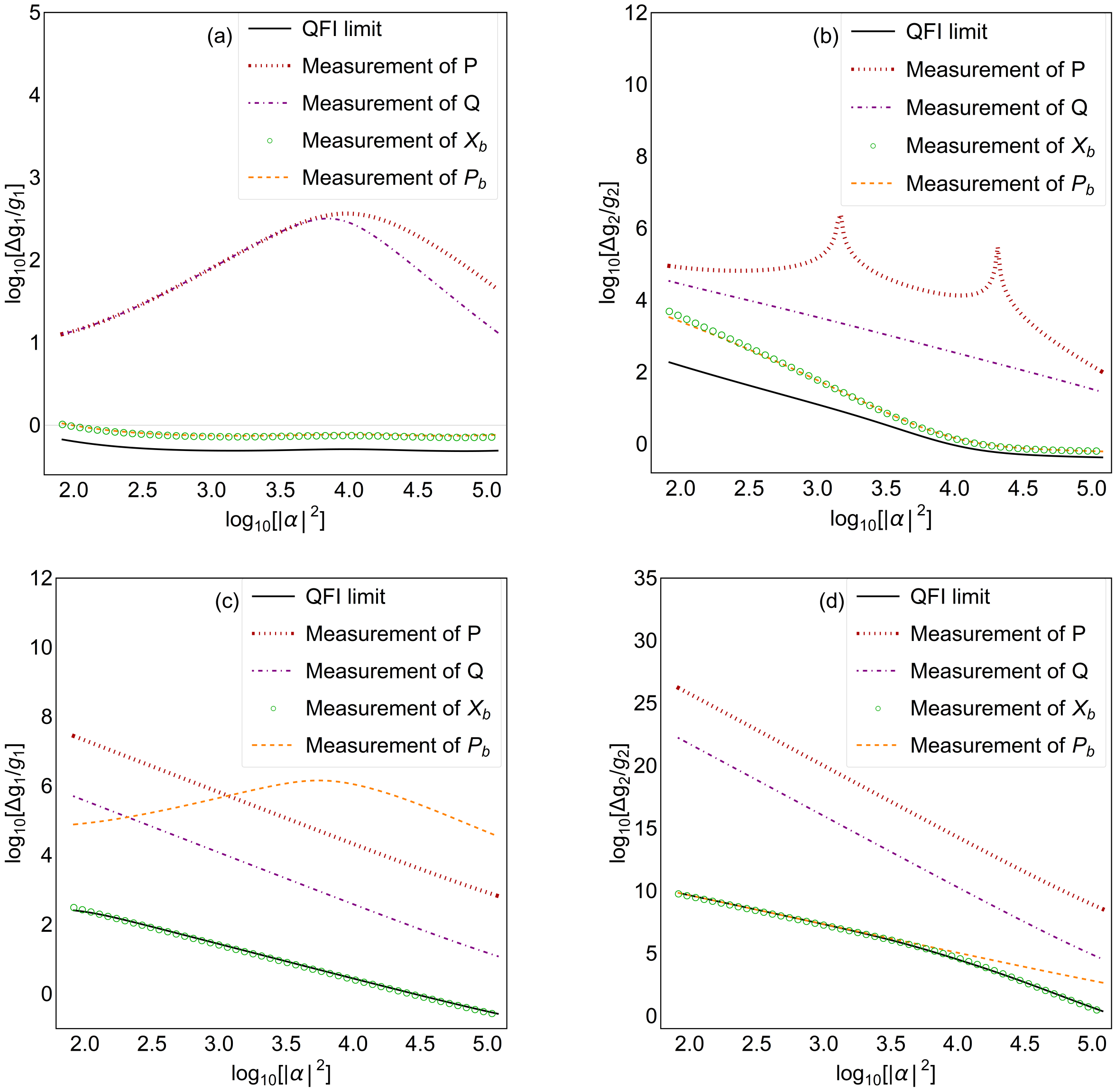

Figure 5.5: Log-log plots of the relative error bounds on the coupling parameters g_1 and g_2 against the intracavity photon number, $|\alpha|^2$, as predicted by the QFI (black line) and the measurements of P (red dotted line), Q (purple dot-dashed line), X_b (green circles) and P_b (orange dashed line). (a) and (b) are for g_1 and g_2 in the high temperature scenario, whilst (c) and (d) are for g_1 and g_2 in the zero-temperature scenario. Reproduced from [1].

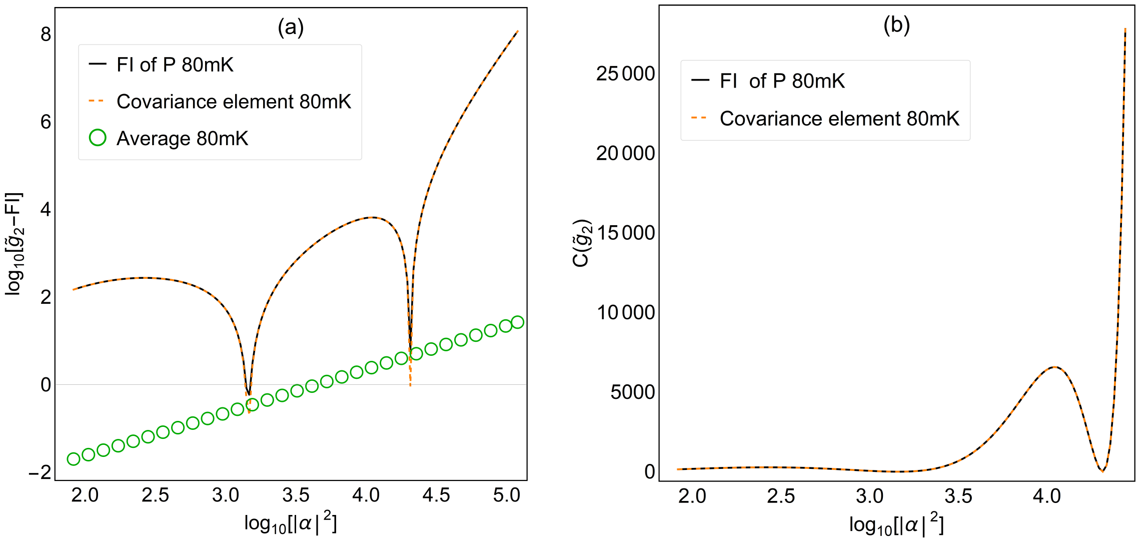

Figure 5.6: (a) Log-log plot comparing the contributions from the covariance element (orange dashed line) and the average (green circles) to the $\tilde{g}_2$-FI for the measurement of P in the quadratic model (black line) in the high temperature scenario. (b) Semi-log plot comparing the contributions from the covariance element (orange dashed line) to the $\tilde{g}_2$-FI for the measurement of P in the quadratic model (black line) in the high temperature scenario.

the measurement of the mechanical position or mechanical momentum constitutes the best strategy for estimating g_1 over the full range of drive strengths considered.

From Fig. 5.5(b), notice also the two peaks of the relative error bound on g_2 for the measurement of the phase quadrature P in the high temperature scenario [1]. This behaviour can be better understood by considering the analytical form of the FI for this measurement (see Eq. 5.7):

$$F(g_2) = \frac{1}{2\bar{\sigma}_{22}(g_2)^2} \times \left[2\bar{\sigma}_{22}(g_2) \left(\frac{\partial P_0}{\partial g_2} \right)^2 + \left(\frac{\partial \bar{\sigma}_{22}(g_2)}{\partial g_2} \right)^2 \right]. \tag{5.9}$$

The FI is composed of two terms consisting of derivatives of the steady state average of the phase quadrature P_0 and of the corresponding diagonal element of the steady state covariance matrix $\bar{\sigma}_{22}$ with respect to the quadratic coupling constant. To clarify the discussion, we shall refer to the first term as the “contribution due to the average” and the second term as the “contribution due to the covariance element” towards the FI for the measurement of P. In Fig. 5.6 we investigate these FI contributions for $\tilde{g}_2$ at $T = 80$ mK. Indeed, for the direct measurement of the phase quadrature, the majority of information about the quadratic coupling constant is contained in the covariance element. The behaviour of the measurement of P in the high temperature scenario will thus resemble that of the second term in Eq. 5.9. The observed peaks then correspond to two extremal points where the information about g_2 is very close to zero, as demonstrated in Fig. 5.6(b).

5.4 Purely quadratic regime

As the name suggests, a purely quadratic model of optomechanics assumes purely quadratic coupling with respect to the dimensionless position of the movable mirror [4, 86]. Such an interaction renormalises the bare frequency of the mechanical oscillator and in consequence, redefines the potential energy of the mechanical element [2]. As such, these systems enable measurement of the oscillator's energy, or equivalently the photon number. This type of coupling can, for example, be engineered in the membrane-in-the-middle optomechanical system through careful positioning of the dielectric membrane.

A purely quadratic model of optomechanics can be recovered by setting g_1 to zero in Eq. 3.11, resulting in the Hamiltonian:

$$H_q = \hbar\omega_m \frac{P_b^2 + X_b^2}{2} + \hbar\left(\omega_0 + g_2 X_b^2\right)\frac{Q^2 + P^2}{2}. \tag{5.10}$$

As usual, we model the dynamics of a driven-damped optomechanical system via the master equation (3.21), which in this case explicitly reads

$$\dot{\rho}(t) = -\frac{i}{\hbar}[H, \rho(t)] + \sum_{ij} \frac{\gamma_{decoh,ij}}{2}\left[2R_i\rho(t)R_j - \{R_jR_i, \rho(t)\}\right], \tag{5.11}$$

with

$$H = \hbar\left(\Delta_0 + g_2 X_b^2\right)\frac{Q^2+P^2}{2} + \hbar\omega_m\frac{X_b^2+P_b^2}{2} + \sqrt{2}\hbar\epsilon Q, \tag{5.12}$$

the corresponding Hamiltonian in the frame rotating at the frequency of the driving laser, ω_L [1]. Once again, Δ_0 is the detuning, $\mathbf{R} = (Q, P, X_b, P_b)$ is the vector of quadrature operators and γ_{decoh} is the matrix of decoherence rates, defined in Eq. 3.18. Moreover, within the framework of the purely quadratic model, the bilinearisation of the master equation (5.11) is justified provided that both conditions $|\alpha|^2 \gg 1$ and $|\epsilon| \gg 2\sqrt{2}\Delta_0$ are satisfied. In that case, the system will admit a Gaussian steady state and the QET tools for estimating unknown parameters in Gaussian models, developed in Sec. 2.4, can once again be employed.

A detailed procedure for approximating the dynamics of driven-dissipative optomechanical systems via a bilinear master equation in the limit of strong cavity driving has been outlined in Sec. 3.4. In summary, we begin by displacing the canonical operators, as per $\mathbf{R} \to \mathbf{R} + \mathbf{R}_0$, where $\mathbf{R}_0 = (Q_0, P_0, x_0, p_0)$ is the vector of steady state quadrature averages, and subsequently neglecting terms that are beyond quadratic in the operators [1]. In the present case of purely quadratic optomechanics, this then generates the following system of equations for the steady state first moments:

$$Q_0 = \frac{-\sqrt{2}\Delta_0\epsilon}{\left(\Delta_0^2 + \frac{\kappa^2}{4}\right)}, \tag{5.13}$$

$$P_0 = \frac{-\sqrt{2}\kappa\epsilon}{2\left(\Delta_0^2 + \frac{\kappa^2}{4}\right)}, \tag{5.14}$$

$$x_0 = p_0 = 0. \tag{5.15}$$

Indeed, in the case of purely quadratic optomechanics, the main effect of the drive is to displace the steady state of the cavity field by an amount that is independent of the quadratic coupling constant [4]. Accordingly, here, all of the information about the quadratic coupling parameter will be contained in the variances.

Following the displacement of the canonical operators in the master equation (5.11), the driven-displaced Hamiltonian takes the form

$$H_D = \frac{\hbar}{2}\left(\Delta_0 + g_2 X_b^2\right)\left(Q^2 + P^2\right) + \hbar g_2 X_b^2\left(QQ_0 + PP_0\right) + \frac{\hbar}{2}\omega_{eff} X_b^2 + \frac{\hbar}{2}\omega_m P_b^2, \tag{5.16}$$

where $\omega_{eff} = \omega_m + 2g_2|\alpha|^2$ is the effective mechanical frequency. Here, terms that do not depend on the canonical operators have already been neglected since they do not contribute towards system dynamics [4]. In order to attain the bilinear form of this Hamiltonian, the remaining cubic and quartic terms (i.e. terms $\propto g_2 X_b^2(QQ_0 + PP_0)$ and $\propto g_2 X_b^2(Q^2 + P^2)$, respectively) need to also be eliminated. To achieve this, a careful consideration of their contributions is required. Indeed, in the case of a purely quadratic model, we simply require the quadratic term $\propto g_2|\alpha|^2 X_b^2$ to have a dominant contribution. Comparing the coefficients of the relevant terms, we then arrive at the two constraints: $|\alpha|^2 \gg 1$ and $|\epsilon| \gg 2\sqrt{2}\Delta_0$. Thus, for strong cavity driving and $|\epsilon| \gg 2\sqrt{2}\Delta_0$, the system dynamics can be approximated via a bilinear master equation description

$$\dot{\rho}(t) = -\frac{i}{\hbar}[H_B, \rho(t)] + \sum_{ij} \frac{\gamma_{decoh,ij}}{2}\left[2R_i\rho(t)R_j - \{R_jR_i, \rho(t)\}\right] \tag{5.17}$$

with

$$H_B = \frac{\hbar}{2}\Delta_0(Q^2 + P^2) + \frac{\hbar}{2}\omega_m P_b^2 + \frac{\hbar}{2}\omega_{eff} X_b^2. \tag{5.18}$$

In accordance with Eq. 3.22, in this case, the matrix Hamiltonian is then simply

$$\mathbf{H} = \begin{pmatrix} \hbar\Delta_0 & 0 & 0 & 0 \\ 0 & \hbar\Delta_0 & 0 & 0 \\ 0 & 0 & \hbar\omega_{eff} & 0 \\ 0 & 0 & 0 & \hbar\omega_m \end{pmatrix}. \tag{5.19}$$

Thus, within the framework of the purely quadratic model, optics couple to the mechanical position via the intracavity photon number.

Thanks to the simplicity of the bilinear model, in this case, an analytical expression for the steady state covariance matrix can be found, which is given below. Indeed, solving the Lyapunov equation (3.30) with $\mathbf{W}$ given in Eq. 3.43, drift matrix

$$\mathbf{B} = \begin{bmatrix} -\frac{\kappa}{2} & -\Delta_0 & 0 & 0 \\ \Delta_0 & -\frac{\kappa}{2} & 0 & 0 \\ 0 & 0 & -\frac{\Gamma_m}{2} & \omega_{eff} \\ 0 & 0 & \omega_m & -\frac{\Gamma_m}{2} \end{bmatrix}, \tag{5.20}$$

and

$$\mathbf{C} = \begin{pmatrix} -\frac{\kappa}{2} & 0 & 0 & 0 \\ 0 & -\frac{\kappa}{2} & 0 & 0 \\ 0 & 0 & -\frac{\Gamma_m}{2}(2\bar{n}_m+1) & 0 \\ 0 & 0 & 0 & -\frac{\Gamma_m}{2}(2\bar{n}_m+1) \end{pmatrix}, \tag{5.21}$$

yields

$$\bar{\boldsymbol{\sigma}} = \begin{bmatrix} \frac{1}{2} & 0 & 0 & 0 \\ 0 & \frac{1}{2} & 0 & 0 \\ 0 & 0 & \frac{(1+2\bar{n}_m)\left(\Gamma_m^2+4\omega_m(\omega_m+g_2|\alpha|^2)\right)}{2(\Gamma_m^2+4\omega_m(\omega_m+2g_2|\alpha|^2))} & \frac{-2g_2|\alpha|^2(1+2\bar{n}_m)}{2(\Gamma_m^2+4\omega_m(\omega_m+2g_2|\alpha|^2))} \\ 0 & 0 & \frac{-2g_2|\alpha|^2(1+2\bar{n}_m)}{2(\Gamma_m^2+4\omega_m(\omega_m+2g_2|\alpha|^2))} & \frac{(1+2\bar{n}_m)\left(\Gamma_m^2+4\omega_m(\omega_m+g_2|\alpha|^2)\right)}{2(\Gamma_m^2+4\omega_m(\omega_m+2g_2|\alpha|^2))} \end{bmatrix}, \tag{5.22}$$

where $\bar{n}_m = 1/\left(e^{\hbar\omega_m/k_B T_m} - 1\right)$ is the mean occupancy of the mechanical oscillator [1]. By inspection, $\bar{\boldsymbol{\sigma}}$ is a real, symmetric matrix. Given that the Robertson-Schrödinger uncertainty relation (Eq. 2.17) is also satisfied, $\bar{\boldsymbol{\sigma}}$ represents a valid steady state covariance matrix of a Gaussian state. In addition, the form of this covariance matrix implies that all of the information about the quadratic coupling constant is contained in the mechanical subsystem. Moreover, the 2 × 2 off-diagonal matrices consisting entirely of zeros indicate the lack of correlations between the mechanical oscillator and the cavity field [4]. In other words, the bilinearisation procedure results in the decoupling of the optical and mechanical degrees of freedom in the steady state.

As demonstrated, in the case of a purely quadratic model, all information about the quadratic coupling constant will be contained in the steady state covariance matrix and, in particular, in the mechanical subsystem. Accordingly, within the framework of the single parameter estimation theory, introduced in Chapter 2, the ultimate limit to the precision with which g_2 can be estimated may be quantified via the QFI, which is now explicitly given by

$$Q(g_2) = 2\mathrm{Tr}\left[\left(\partial_{g_2}\bar{\boldsymbol{\sigma}}\right)\left(4\mathcal{L}_{\bar{\sigma}} + \mathcal{L}_W\right)^{-1}\left(\partial_{g_2}\bar{\boldsymbol{\sigma}}\right)\right], \tag{5.23}$$

with $\mathcal{L}_{\bar{\sigma}}(\mathbf{A}) = \bar{\boldsymbol{\sigma}}\mathbf{A}\bar{\boldsymbol{\sigma}}$ and $\mathcal{L}_W(\mathbf{A}) = \mathbf{WAW}$ representing the superoperators [1, 55, 56]. However, as the pseudoinverse $(4\mathcal{L}_{\bar{\sigma}} + \mathcal{L}_W)^{-1}$ might in general be difficult to evaluate analytically, we shall use the following formula for the QFI instead, valid for general single-mode Gaussian states [87]:

$$Q(g_2)_{sm} = \frac{\mathrm{Tr}\left[\left(\bar{\boldsymbol{\sigma}}_m^{-1}\partial_{g_2}\bar{\boldsymbol{\sigma}}_m\right)^2\right]}{2(1+\mathcal{P}_{g_2})} + \frac{2\left(\partial_{g_2}\mathcal{P}_{g_2}\right)^2}{1-\mathcal{P}_{g_2}^4}, \tag{5.24}$$

where $\bar{\boldsymbol{\sigma}}_m = \mathrm{Tr}_l[\bar{\boldsymbol{\sigma}}]$ is a 2 × 2 steady state covariance matrix for the mechanical mode only (obtained by taking a partial trace over the light mode) and

$$\begin{aligned}\mathcal{P}_{g_2} &= \left(\det(\bar{\boldsymbol{\sigma}}_m)\right)^{-\frac{1}{2}} \\ &= \frac{2}{\left((2\bar{n}_m+1)^2\left(\frac{64g_2^2\epsilon^4}{\left(4\Delta_0^2+\kappa^2\right)\left(32g_2\epsilon^2\omega_m+\left(4\Delta_0^2+\kappa^2\right)(\Gamma_m^2+4\omega_m^2)\right)}+1\right)\right)^{\frac{1}{2}}}\end{aligned} \tag{5.25}$$

is the purity of the mechanical-mode steady state[1]. Indeed, in the case of a purely quadratic model, the bilinearisation procedure essentially results in a single-mode Gaussian steady state described purely by $\bar{\boldsymbol{\sigma}}_m$ (as the steady state averages of the mechanics vanish, see Eq. 5.15).

Alternatively, in congruence with the QCRB (Eq. 2.3), this ultimate limit may be measured via the single shot relative error, satisfying the inequality

$$\frac{\Delta g_2}{g_2} \geq \frac{1}{g_2\sqrt{Q(g_2)}} \equiv \delta g_2^{\mathrm{min}}. \tag{5.26}$$

As anticipated, here, we simply examine the estimation performance of the measurements of the mechanical position X_b and mechanical momentum P_b. As usual, this may be quantified via the FI, which following from Eq. 2.20 with g_2 as the parameter of interest, is explicitly given by

$$F(g_2) = \frac{1}{2\bar{\sigma}_{kk}(g_2)^2} \times \left[2\bar{\sigma}_{kk}(g_2)\left(\frac{\partial s_0(g_2)}{\partial g_2}\right)^2 + \left(\frac{\partial \bar{\sigma}_{kk}(g_2)}{\partial g_2}\right)^2\right], \tag{5.27}$$

where $s_0(g_2) \in \{x_0, p_0\}$ is the steady state average of the chosen quadrature, and $\bar{\sigma}_{kk}(g_2)$ is the corresponding diagonal element of the steady state covariance matrix (i.e. $\bar{\sigma}_{33}$ for the measurement of X_b and $\bar{\sigma}_{44}$ for the measurement of P_b). In this case, the FI for the measurements of X_b and P_b can be expressed explicitly as

$$F_{X_b}(g_2) = \frac{8\omega_m^4|\alpha|^2\left(\Gamma_m^2 + 4\omega_m^2\right)^2}{\left(4\omega_{eff}\omega_m + \Gamma_m^2\right)^2\left(2\omega_m\left(\omega_{eff} + \omega_m\right) + \Gamma_m^2\right)^2}, \tag{5.28}$$

and

$$F_{P_b}(g_2) = \frac{8\omega_m^2|\alpha|^2\left(\Gamma_m^2\left(\omega_m - 2\omega_{eff}\right) - 4\omega_{eff}^2\omega_m\right)^2}{\left(4\omega_{eff}\omega_m + \Gamma_m^2\right)^2\left(2\omega_{eff}\left(\omega_{eff} + \omega_m\right) + \Gamma_m^2\right)^2}. \tag{5.29}$$

---

[1] Note that Eq. 5.24 allows for the QFI to be evaluated analytically. However, due to its lengthy expression, this analytical form has not been included in the thesis.

As before, here, we investigate the effects of temperature and driving on the estimation precision of the quadratic coupling constant. For comparative purposes, we adopt the same parameter values as in Sec. 5.3, except that g_1 will now be set to zero. The corresponding parameter values are: $\omega_m = 1.1 \times 10^7$ Hz, $m = 4.8 \times 10^{-14}$ kg, $\Gamma_m = 32$ Hz, $\Delta_0 = \omega_m$, $\kappa = 10^5$ Hz and $g_2 = 10$ Hz [26]. We also choose the same starting point for our region of interest. However, to capture all of the interesting features of the optomechanical system within the framework of the purely quadratic model, we extend our range of drive strengths to $10^8 \leq \epsilon \leq 1.5 \times 10^{12}$ Hz (or $80 \lesssim |\alpha|^2 \lesssim 1.8 \times 10^{10}$ in terms of the intracavity photon number). Indeed, since the mechanical position is unchanged by the strong cavity driving and the steady state displacements of the light quadratures are all real numbers, the system described by the purely quadratic model will remain stable at all intracavity photon numbers. Accordingly, any range of drive strengths that satisfies the two constraints for the validity of our bilinear approximation will in general constitute a suitable choice for the model. Moreover, to better understand the effect of the strength of the optomechanical interaction on the estimation precision of the quadratic coupling constant, we also explore a regime where $g_2 = 100$ Hz with the remaining parameter values and the study region unchanged.

As usual, to assess the effects of temperature on the estimation precision of the quadratic coupling constant, we consider three temperature scenarios: zero temperature ($T_m = 0$ K), low temperature ($T_m = 1$ mK) and "high" temperature ($T_m = 80$ mK) of the mechanical bath. In Fig. 5.7, we investigate the dependence of the relative error bound on g_2 – $\delta g_2^{\mathrm{min}}$ – on temperature and driving in these three temperature scenarios and for two separate g_2 values. As illustrated, for both g_2 values, the highest estimation precision for estimating the quadratic coupling parameter can be achieved at zero temperature for sufficiently low intracavity photon numbers (i.e. $\log_{10}|\alpha|^2 \lesssim 6.9$ for $g_2 = 10$ Hz or $\log_{10}|\alpha|^2 \lesssim 5.9$ for $g_2 = 100$ Hz). Additionally, focusing on the non-zero temperature scenarios, in this region, $\delta g_2^{\mathrm{min}}$ is approximately unchanged with temperature,

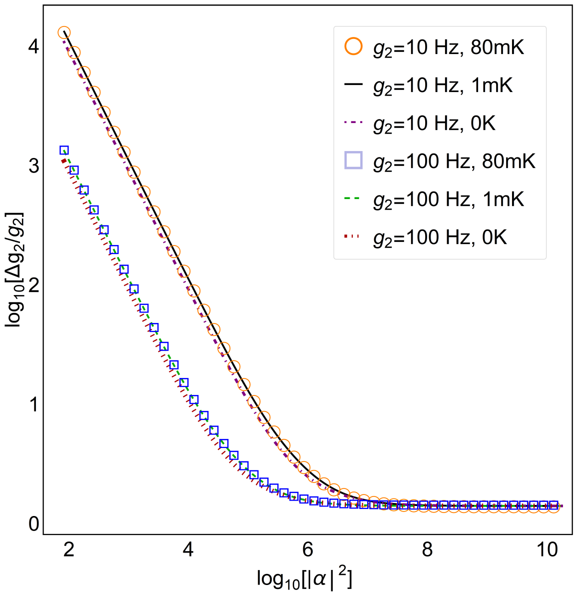

Figure 5.7: Log-log plot of the relative error bound on g_2 (as implied by the QFI) against the intracavity photon number, $|\alpha|^2$, as predicted by the purely quadratic model in the red-detuned regime for $g_2 = 10$ Hz and $g_2 = 100$ Hz in the zero temperature (purple dot-dashed line and red dotted line, respectively), low temperature (black line and green dashed line, respectively) and high temperature (orange circles and blue squares, respectively) scenarios.

thus demonstrating weak temperature dependence of the estimation precision of this parameter. Interestingly, the influence of the strength of the optomechanical interaction on the estimation precision of the quadratic coupling constant is mostly significant in the low-high driving regime, where the higher g_2 value leads to an improvement in the estimation precision. In contrast, at very high intracavity photon numbers, all temperature scenarios examined and g_2 values give qualitatively identical results. In particular, δg_2^{min} tends to approximately $\sqrt{2}$ for very large driving powers. The origin of this limit is not well understood and requires further work to analyse. Nevertheless, for all temperature scenarios, the relative error bound on g_2 displays the same behaviour with driving: δg_2^{min} decreases monotonically with the intracavity photon number before saturating at sufficiently high $|\alpha|$. Beyond this saturation point, stronger driving offers no improvement to the estimation precision of the quadratic coupling constant. Moreover, in the very high driving region, the strength of the optomechanical interaction simply affects the value of ϵ at which the relative error bound on g_2, as given by the three temperature scenarios,

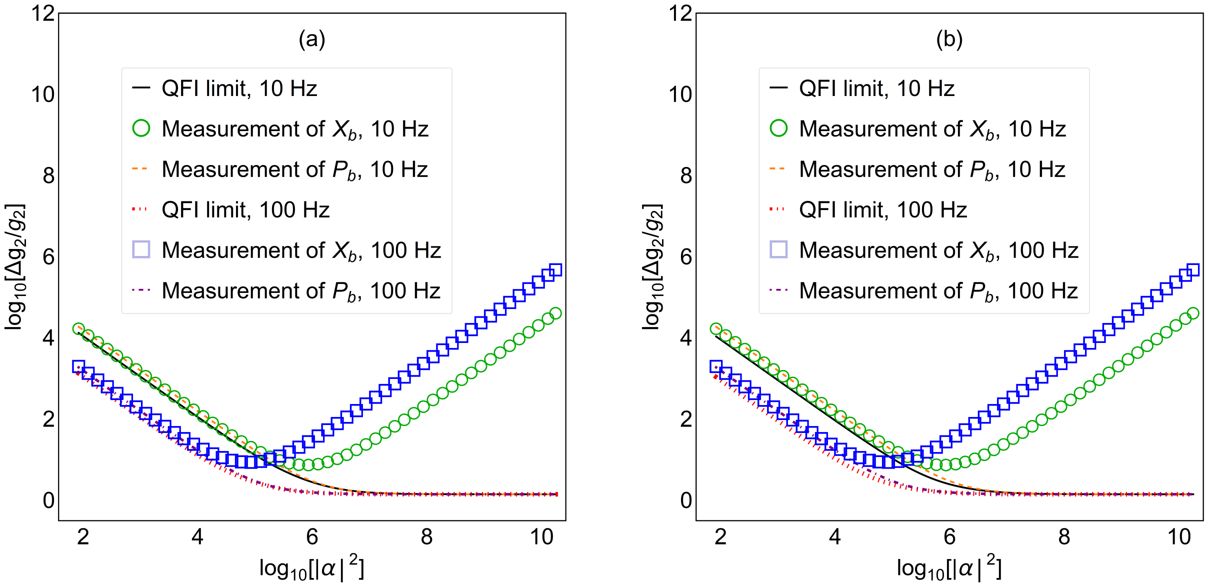

Figure 5.8: Log-log plots of the relative error bound on g_2 (as implied by the QFI) against the intracavity photon number, $|\alpha|^2$, for $g_2 = 10$ Hz and $g_2 = 100$ Hz in the red-detuned regime (black line and red dotted line, respectively) as well as the measurements of X_b (green circles and blue squares, respectively) and P_b (orange dashed line and purple dot-dashed line, respectively). (a) and (b) are for g_2 in the high and zero temperature scenarios, respectively.

saturate.

In Fig. 5.8 we compare the performances of the realistic measurements of X_b and P_b against the ultimate QFI limits in the zero and high temperature scenarios and for two separate g_2 values. In general, the measurement of the mechanical momentum almost always does best at estimating the quadratic coupling constant. Instead, the measurement of the mechanical position displays non-monotonic behaviour with a minimum point located at $|\alpha|^2 = (\Gamma_m^2 + 4\omega_m^2)/4\sqrt{2}g_2\omega_m$. The measurement of X_b shows a good agreement with the QFI limit in the low driving regime, i.e. below this minimum value.

In Fig. 5.8, weak temperature dependence of the estimation precision of g_2 is also further demonstrated. In the low driving regime, the agreement between the ultimate limits to the estimation precision of the quadratic coupling constant and the realistic measurements improves slightly at higher temperatures. Additionally, in the high temperature scenario, these ultimate limits can be approached by the measurement of the mechanical momentum at somewhat lower intracavity photon numbers. As the coupling strength is increased, the agreement between the measurement of P_b and the QFI limits is also further improved.

5.5 Conclusion: quantum estimation in beyond linear-model optomechanics

In this chapter, we explored the application of local QET in driven-dissipative optomechanics within the frameworks of the quadratic and purely quadratic models. In the case of a quadratic model, we found that the higher order g_2 term has a temperature-dependent effect on the estimation precision of the linear coupling constant, mainly affecting the behaviour of the relative error bound on g_1 in the high temperature scenario. Our analysis also revealed that the ultimate limit to the estimation precision of g_1 can only be reached in the zero temperature scenario via a measurement of the mechanical quadrature X_b, which is indeed consistent with our findings for the linear model. Additionally, exploring the influence of temperature on the estimation precision of the coupling strengths, we found that for some parameter regimes, higher temperatures can have favourable effect on the estimation performance. In fact, in the case of the quadratic coupling constant, a hotter mechanical bath led to an improved estimation performance of this parameter. Nevertheless, we found that the ultimate limits for estimating g_2 can only be approached in the zero temperature scenario via a measurement of X_b for all intracavity photon numbers within our study range, or a measurement of P_b in the low driving regime.

In the case of a purely quadratic model, we investigated the effects of cavity driving, temperature and the strength of the optomechanical interaction on the estimation precision of the quadratic coupling constant. For all temperatures considered, we found that the relative error bound on g_2 decreases monotonically with the intracavity photon number before saturating at approximately $\sqrt{2}$ for sufficiently high drive strengths. Beyond this saturation point, extra driving was found to have no effect on the estimation precision of the parameter. Our analysis also revealed that all information about the quadratic coupling constant is contained in the mechanical subsystem. As such, the ultimate limits to estimation precision could typically only be reached in the high driving regime via a measurement of P_b. Additionally, these ultimate limits as well as the measurements of the mechanical quadratures X_b and P_b showed very weak dependence on temperature. Indeed, we found that the zero temperature scenario predicts slightly lower relative errors in the low-high driving regime before converging with the non-zero temperature scenarios, and eventually saturating.

In future work, one could investigate the origin of the saturation point in the purely quadratic model of optomechanics. This could perhaps be achieved by solving the rate equations for the mechanical oscillator in the classical limit and evaluating the QFI analytically [88]. As all information about the quadratic coupling constant is contained in the mechanical degrees of freedom, this could also aid our understanding of the weak temperature dependence of the estimation precision of this parameter.

Chapter 6

Quantum van der Pol Oscillator

6.1 Introduction

The van der Pol (vdP) oscillator is a prototypical self-oscillatory system that can phase lock with an external drive or with other oscillators [37, 108]. It was originally proposed by Balthazar van der Pol in the late 1920s to describe non-linear behaviour in electrical circuits [109]. The vdP oscillator has since been used to model oscillatory processes in physics, biology, electronics, among other fields.

Self-oscillators are non-linear systems in which amplification (or negative damping) competes with non-linear damping [4]. These oscillators take energy from a source in a way that the energy gained is equal to the energy lost, thus resulting in limit cycles [111, 112]. In short, limit cycles are isolated closed trajectories in phase space. Stable limit cycles are particularly relevant to the concept of self-sustained oscillators - they are attractors, thus despite the initial conditions, or driving, the solutions will inevitably fall onto the stable oscillations as time approaches infinity [113]. The amplitude of these oscillations is governed by the rates of negative and non-linear damping.

The classical model of a vdP oscillator has been used extensively to study the phenomenon of synchronisation [114]. In short, synchronisation is a collective behaviour of a group of self-oscillators which when weakly coupled can oscillate in unison. Recently, a quantum version of the vdP oscillator model has been proposed using a Lindblad master equation that combines a linear anti-damping (gain) process with non-linear loss [37]. Due to the simplicity of its quantum model, the vdP oscillator has also been proven useful for studying synchronisation in the quantum limit where quantum fluctuations become important [111]. Accordingly, with the vdP oscillator as the model system, the differences in the extent of this phenomenon in the classical and quantum regimes can be thoroughly explored [112]. In fact, a qualitative comparison of the synchronisation behaviour in the two regimes was recently investigated in [115], revealing some significant differences. In [114], the quantum vdP oscillator was also used to study the connection between entanglement and synchronisation. More importantly, for our purposes, the quantum vdP oscillator is a step towards studying the blue-detuned regime of quantum optomechanics where limit cycles also occur, but in a more complex model [36, 102].

This chapter explores the application of local QET in a quantum vdP oscillator to estimate the ratio of the linear and non-linear damping rates, λ. It is organised as follows. In Sec. 6.2, starting with the classical model, the origin of the quantum model of the vdP oscillator is reviewed. There, the procedure for deriving the exact steady state solution for the vdP oscillator is also outlined. Then, in Sec. 6.3 we recall the QET theory and give explicit formulas that are applicable to this system. Subsequently, in Sec. 6.4 we outline the procedure for evaluating the QFI numerically, whilst in Sec. 6.5 we use analytical approximations to analyse the behaviour of the QFI in two limiting cases: $\lambda \ll 1$ and $\lambda \gg 1$. In Sec. 6.5 we additionally compare the analytical results against the numerical methods, and explore the behaviour of the QFI in the intermediate region. Finally, in Sec. 6.6 we summarise our findings.

6.2 Quantum model

The vdP oscillator is perhaps the most well-known example of a self-sustained oscillator [37, 115]. Classically, its evolution can be described with a non-linear second order differential equation:

$$\ddot{x} - \gamma_1(1 - \gamma_2 x^2)\dot{x} + \omega_0^2 x = 0, \tag{6.1}$$

with ω_0 the natural frequency of the oscillator and x a dimensionless displacement [39, 108, 111]. The vdP model includes dissipation and gain processes: negative damping $(-\dot{x})$ and non-linear damping $(x^2\dot{x})$ at rates γ_1 and $\gamma_1\gamma_2$, respectively, the combination of which gives rise to a limit cycle. More explicitly, making a change of variables via

$$x = \frac{\alpha + \alpha^*}{2}, \qquad \dot{x} = i\omega_0 \frac{\alpha^* - \alpha}{2}, \tag{6.2}$$

the resulting limit cycle can be approximated by the amplitude equation [114, 116]

$$\dot{\alpha} = -i\omega_0\alpha + \alpha\gamma_1(1 - \frac{\gamma_2}{4}|\alpha|^2). \tag{6.3}$$

This result has been achieved with help of the rotating wave approximation by which fast oscillating terms can be neglected on the assumption that both $\gamma_1 \ll \omega_0$ and $\gamma_2 \ll \omega_0/\gamma_1$ [4]. For a detailed derivation of the amplitude equation (6.3) see Appendix B. Moreover, provided that $\gamma_1, \gamma_2 > 0$, the steady state solution is a stable limit cycle with amplitude $|\alpha| = 2/\sqrt{\gamma_2}$, frequency ω_0 and no preferred phase.

6.2.1 Master equation

In a quantum regime, the vdP oscillator is modelled as an open quantum system, i.e. a system that is coupled to its environment [68]. Accordingly, the dynamics of the quantum vdP oscillator can be described via a master equation of the form [37, 39, 111]

$$\begin{aligned}\dot{\rho}(t) + i\left[\omega_0 a^\dagger a, \rho(t)\right] =& \kappa_1\left(2a^\dagger\rho(t)a - aa^\dagger\rho - \rho(t)aa^\dagger\right)\\ &+ \kappa_2\left(2a^2\rho(t)\left(a^\dagger\right)^2 - \left(a^\dagger\right)^2 a^2\rho(t) - \rho(t)\left(a^\dagger\right)^2 a^2\right). \end{aligned} \tag{6.4}$$

Namely, a quantum vdP oscillator is modelled as a quantum harmonic oscillator with frequency ω_0, and annihilation and creation operators a and $a^\dagger$ [94]. As anticipated, the interaction of the oscillator with its environment leads to two dissipative processes: negative damping and non-linear damping, quantified with κ_1 and κ_2, respectively [114]. Physically, these processes correspond to a gain of a phonon at a rate $2\kappa_1\langle aa^\dagger\rangle$ and a loss of two phonons at a rate $2\kappa_2\langle(a^\dagger)^2a^2\rangle$.

The quantum limit of the quantum vdP oscillator can be realised in a regime where $\kappa_2 \gg \kappa_1$ in which case the two-phonon emission process dominates and the oscillator has a very low mean occupation number [4, 37, 114]. Conversely, the classical regime is recovered when $\kappa_2/\kappa_1 \to 0$. In this case, the one-phonon anti-damping (i.e. gain) process dominates, which leads to the oscillator having a large number of phonons (i.e. $n = \langle a^\dagger a\rangle \gg 1$) [111]. Moreover, the interconnection of the quantum and classical models can be realised by considering the evolution of the expectation value of the annihilation operator, a. Indeed, using the relation $\langle\dot{a}\rangle = \mathrm{Tr}[a\dot{\rho}(t)]$, we find that the annihilation operator evolves as per [94]

$$\langle\dot{a}\rangle = -i\omega_0\langle a\rangle + \kappa_1\langle a\rangle - 2\kappa_2\langle a^\dagger a^2\rangle. \tag{6.5}$$

Also, making a semi-classical approximation $\langle a^\dagger aa\rangle = |\alpha|^2\alpha$, and defining $\alpha = \langle a\rangle$, results in an amplitude equation equivalent to that in Eq. 6.3 with $\kappa_1 = \gamma_1$ and $\kappa_2 = \gamma_1\gamma_2/8$. It is thus evident that the two dissipative terms in the master equation (6.4) are simply quantum analogues to the classical damping terms in Eq. 6.3. Accordingly, the limit cycle behaviour of the steady state of the vdP oscillator is preserved in the quantum regime, provided that $\kappa_1, \kappa_2 > 0$ [39]. In addition, the fact that the limit cycle is found in the quantum regime is attributed to the non-linear dissipative term in Eq. 6.4; this limit cycle behaviour would not be observed if the damping terms were purely linear.

6.2.2 Exact solution

The relative simplicity of the quantum vdP model (6.4) signifies that the system's steady state can be obtained exactly. To demonstrate this, our analysis proceeds from rate equations satisfied by the probabilities[1] $p_n = \langle n|\rho(t)|n\rangle$ for the vdP oscillator to occupy the nth energy eigenstate [94]:

$$\dot{p}_n(t) = 2\kappa_1[np_{n-1} - (n+1)p_n] + 2\kappa_2[(n+1)(n+2)p_{n+2} - n(n-1)p_n]. \tag{6.6}$$

Indeed, the symmetry of the problem means that the system is diagonal in the harmonic oscillator basis. In a stationary case ($\dot{p}_n(t) = 0$), an exact analytical solution to this set of equations can be found by introducing a steady state generating function

$$G(z) = \sum_{n=0}^{\infty} z^n p_n, \tag{6.7}$$

where z is an auxiliary variable [118, 119]. In consequence, the rate equations (6.6) reduce to a single differential equation with respect to the variable z

$$G''(z)(1+z) - \lambda z G'(z) - \lambda G(z) = 0, \tag{6.8}$$

where $\lambda = \kappa_1/\kappa_2$ is the ratio of the strengths of phonon absorption (i.e. gain) and emission processes. This differential equation can then be solved subject to two boundary

---

[1] All of the off-diagonal elements of the density matrix decouple from the diagonal ones and decay to zero in the steady state of the vdP oscillator [117].

conditions: the normalisation condition

$$G(1) = \sum_{n=0}^{\infty} p_n = 1, \tag{6.9}$$

and the semi-positivity requirement of the probabilities

$$p_n = \frac{1}{n!}\frac{d^n G}{dz^n}\Big|_{z=0} \geq 0. \tag{6.10}$$

Accordingly, the analytical solution can be found by transforming the differential equation (6.8) into the exactly solvable Kummer's equation:

$$xy'' + (\lambda - x)y' - y = 0, \tag{6.11}$$

achieved through a substitution $x = \lambda(1+z)$, such that $y = G(x)$.

Kummer's equation has two singularities at $x = 0$ and $x = \infty$, or $z = -1, \infty$ in the original variable. The solution to Eq. 6.11 is chosen to ensure that $G(z)$ remains finite at $z = -1$ [118]. This, in turn, leaves us with a solution in the form of the confluent hypergeometric function, $\Phi(1; \lambda; x)$ [119]. Indeed, in the original variable z and subject to the normalisation condition (6.9), the following solution to Eq. 6.8 is obtained

$$G(z) = \frac{\Phi(1; \lambda; \lambda(1+z))}{\Phi(1; \lambda; 2\lambda)}. \tag{6.12}$$

In this case, the semi-positivity requirement of the probabilities (Eq. 6.10) is satisfied provided that $\lambda > 0$ which, by construction, is always guaranteed. Knowing the steady state generating function, the probabilities can now be calculated via

$$p_n = \frac{1}{n!}\frac{\partial^n G}{\partial z^n}|_{z=0}. \tag{6.13}$$

In fact, with help of the relation

$$\frac{d^n}{dx^n}\Phi(a;c;x) = \frac{(a)_n}{(c)_n}\Phi(a+n;c+n;x), \tag{6.14}$$

where $(a)_n = a(a+1)...(a+n-1) = \Gamma(a+n)/\Gamma(a)$ is the Pocchammer symbol and $\Gamma(a) = (a-1)!$ is the gamma function, the probabilities can be shown to satisfy [120]

$$p_n = \frac{(\lambda)^n}{(\lambda)_n}\frac{\Phi(1+n;\lambda+n;\lambda)}{\Phi(1;\lambda;2\lambda)}, \tag{6.15}$$

with $(\lambda)_n = \lambda(\lambda+1)...(\lambda+n-1) = \Gamma(\lambda+n)/\Gamma(\lambda)$. Using the above relation, the steady state of the quantum vdP oscillator can be shown to have the following analytical form:

$$\rho_{SS} = \sum_n \frac{(\lambda)^n}{(\lambda)_n}\frac{\Phi(1+n;\lambda+n;\lambda)}{\Phi(1;\lambda;2\lambda)}|n\rangle\langle n|. \tag{6.16}$$

The off-diagonal elements of the density matrix decouple from the diagonal ones and are all found to be zero, as noted previously [117].

6.2.3 Behaviour of the steady state occupation probabilities

The behaviour of the steady state occupation probabilities of the quantum vdP oscillator p_n is distinctively different for small and large values of the parameter λ. In the limit $\lambda \ll 1$ (corresponding to a regime where $\kappa_1 \to 0$), the quantum vdP oscillator is largely confined to its ground state and its first excited state with probabilities $p_0 = 2/3$ and $p_1 = 1/3$, as evidenced in Fig. 6.1(a) [37]. In this regime, the two-phonon emission process dominates; hence, all higher energy eigenstates are annihilated by the non-linear damping, and the quantum limit is approached. Indeed, in this case, the steady state of the oscillator has a simple analytical form: $\rho_{SS} \approx 2/3|0\rangle\langle 0| + 1/3|1\rangle\langle 1|$.

The classical vdP oscillator can also be considered to have a critical point at $\lambda = 0$,

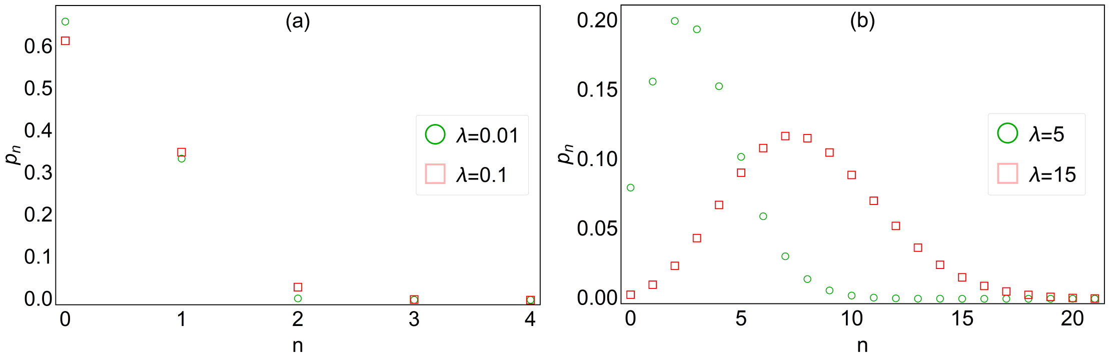

Figure 6.1: Semi-log plots of the steady state occupation probabilities p_n against the phonon number n for (a) small ($\lambda = 0.01$ - green circles and $\lambda = 0.1$ - red squares) and (b) intermediate λ values ($\lambda = 5$ - green circles and $\lambda = 15$ - red squares).

associated with the divergence of susceptibility in this limit [39]. In short, susceptibility quantifies the response of the oscillator to a weak drive, and is defined by the gradient of the steady state amplitude with respect to the drive strength [4]. It is also noteworthy that systems in the neighbourhood of a critical point are very sensitive to perturbations. Interestingly, in [39] the authors showed that this concept can be carried across to the quantum regime. This suggests that in the limit $\lambda \to 0$, the quantum vdP oscillator could be used as a sensitive measuring device since its amplitude should be highly sensitive to any small changes in the weak drive signal.

As the size of λ is increased, the probability distribution becomes more spread out, as seen in Fig. 6.1(b). For increasingly large λ, the steady state occupation probability p_n peaks at progressively larger phonon number n.

In the large λ limit, the one-phonon anti-damping process dominates instead, leading to the oscillator having a large number of phonons (i.e. $n = \langle a^\dagger a \rangle \gg 1$). In this regime, it is thus expected that the dynamics of the quantum vdP oscillator approach its classical analogue with $n \approx |\alpha|^2$ and its energy spectrum becoming continuous [111, 115]. Accordingly, in the large λ limit, we treat n as a continuous rather than a discrete variable.

Moreover, in the weak two-phonon emission regime, the probabilities p_n can be shown to

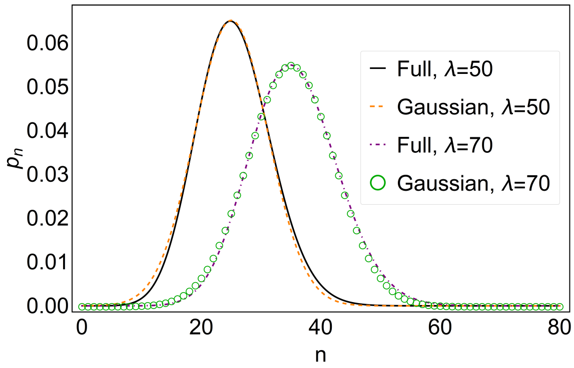

Figure 6.2: Plot comparing the steady state occupation probabilities p_n for large λ values as given by the full analytical form ($\lambda = 50$ - black line and $\lambda = 70$ - purple dot-dashed line) and the Gaussian approximation ($\lambda = 50$ - orange, dashed line and $\lambda = 70$ - green circles). Here, the values specified by the full analytical form have been plotted as continuous curves although they are, strictly speaking, only defined for integer values of n.

follow a Gaussian distribution [118]

$$p_n = \mathcal{A} \left(\frac{2}{3\pi\lambda} \right)^{\frac{1}{2}} e^{-\frac{(2n-\lambda)^2}{6\lambda}}, \tag{6.17}$$

where $\mathcal{A}$ is a normalisation factor for the interval $0 \leq n < \infty$, with an explicit form

$$\mathcal{A} = \left(\frac{1}{2} \operatorname{erfc} \left(\sqrt{\frac{\lambda}{6}} \right) \right)^{-1}. \tag{6.18}$$

In the limit $\lambda \to \infty$, this normalisation factor can simply be replaced by unity. Thus, we arrive at a Gaussian distribution with mean $\langle n \rangle = \lambda/2$ and variance $\Delta^2 n = 3\lambda/4$ [2][115]. In Fig. 6.2, we show that the Gaussian distribution is indeed a good approximation to the full analytical form for the steady state occupation probabilities of the quantum vdP oscillator (Eq. 6.15), the agreement between which improves with λ.

---

[2] The steady state of the vdP system can also be visualised in phase space using the Wigner function. However, this adds very little to the number distribution itself: the fact that the number distribution is diagonal implies a Wigner function with circular symmetry (see [117]). One therefore finds that the Wigner function of the vdP oscillator is always a ring in phase space and it is also always positive (see [117]).

6.3 Quantum estimation

As discussed in Chapter 2, the goal of QET is to find the best strategy for estimating unknown parameters in quantum systems [33]. In the case of a quantum vdP oscillator, the parameter of interest is λ, the magnitude of which quantifies which of the two dissipative processes - linear amplification or non-linear damping - dominates. Indeed, in this case, the task of single parameter estimation theory is to estimate λ through a measurement of some observable on ρ_λ, described by a POVM. To summarise, given a choice of a POVM, the FI can in general be calculated via the Symmetric Logarithmic Derivatives (SLDs, found by solving $\mathcal{L}_\lambda \rho_\lambda + \rho_\lambda \mathcal{L}_\lambda = \partial \rho_\lambda / \partial \lambda$):

$$F(\lambda) = \int dx \frac{\left(Re\left(Tr\left[\rho_\lambda \Pi_x \mathcal{L}_\lambda\right]\right)\right)^2}{\mathrm{Tr}[\Pi_x \rho_\lambda]}. \tag{6.19}$$

Maximising the FI over all possible POVMs then yields the QFI [59]:

$$Q(\lambda) = \mathrm{Tr}[\rho_\lambda \mathcal{L}_\lambda^2]. \tag{6.20}$$

The above relations can be further simplified by considering a special case of a density matrix that is diagonal in its number state basis. This scenario is of particular interest for a quantum vdP oscillator whose steady state solution is indeed of the diagonal form (Eq. 6.16). Accordingly, as the SLD satisfies the Lyapunov matrix equation (2.5), its general solution can be written as [33]

$$\mathcal{L}_\lambda = 2 \int_0^\infty dt e^{-\rho_\lambda t} \partial_\lambda \rho_\lambda e^{-\rho_\lambda t}. \tag{6.21}$$

Assuming that ρ_λ is diagonal in its number state basis, such that $\rho_\lambda = \sum_n p_n |n\rangle\langle n|$, this solution then becomes

$$\mathcal{L}_\lambda = 2\sum_{n,m} \frac{\langle m|\partial_\lambda \rho_\lambda|n\rangle}{p_n + p_m}|m\rangle\langle n|, \tag{6.22}$$

with $p_n + p_m \neq 0$. Hence, in this special case, the QFI is simply given by

$$Q(\lambda) = 2\sum_{n,m} \frac{|\langle m|\partial_\lambda \rho_\lambda|n\rangle|^2}{p_n + p_m}. \tag{6.23}$$

In this particular example, only the probabilities p_n depend on the parameter λ; hence, the partial derivative can be explicitly written as $\partial_\lambda \rho_\lambda = \sum_n \partial_\lambda p_n|n\rangle\langle n|$. Inserting this relation into Eqs. 6.22 and 6.23 then gives

$$\mathcal{L}_\lambda = \sum_n \frac{\partial_\lambda p_n}{p_n}|n\rangle\langle n|, \tag{6.24}$$

$$Q(\lambda) = \sum_n \frac{(\partial_\lambda p_n)^2}{p_n}. \tag{6.25}$$

Due to the eigenvectors (i.e. the number states) being independent of the parameter λ, in the special case of a quantum vdP oscillator, the FI of the measurement of a number operator is equal to the QFI. This automatically implies that the number state is the optimal observable for the estimation of λ. In other words, this indicates that the quantum statistical model is indeed a "classical statistical model", where only eigenvalues depend on the parameter.

6.4 Numerical calculations

We now turn to explore the behaviour of the QFI for the quantum vdP oscillator in detail. We start by discussing a numerical approach for calculating the QFI. This allows us to explore the behaviour of the QFI over a wide range of λ values whilst also suggesting that simple limiting forms emerge for very large and very small λ. Then, in Sec. 6.5 we show how these limiting forms can be derived analytically.

The finite difference method (FDM) is one of the simplest numerical methods used to solve differential equations [121]. In this method, the derivatives are approximated with appropriate difference quotients and the differential equation is reduced to a system of polynomial equations as a result [122]. In the FDM, the function $f'(x_0)$ is approximated via

$$f'(x_0) \approx \frac{f(x_0 + \Delta x) - f(x_0)}{\Delta x}, \tag{6.26}$$

where Δx, the step size, is assumed to be small [123, 124]. This identity is known as the first order approximation of $f'(x_0)$; it gives an approximation of the derivative accurate to $O(\Delta x)$.

In the case of a quantum vdP oscillator, the FDM can be used to obtain a numerical approximation to the QFI (Eq. 6.25). In particular, we can use this method to approximate the derivative of the probabilities with respect to the ratio of the strengths of phonon absorption (i.e. gain) and emission processes, λ. We start by setting up an array of p_n evaluated at k different λ values with a step size $\Delta\lambda = (\lambda_k - \lambda_1)/k$. At some value $\lambda_j \in [\lambda_1, \lambda_k]$, the probabilities are then given by $p_n(\lambda_j) = p_n(\lambda_1 + j\Delta\lambda)$. As per Eq. 6.26, at this point, the derivative of p_n can be approximated using

$$\partial_\lambda p_n(\lambda_j) \approx \frac{p_n(\lambda_{j+1}) - p_n(\lambda_j)}{\Delta\lambda}. \tag{6.27}$$

In order to ensure that this approximation is accurate, we require $\Delta\lambda$ to be very small. In more detail, we require $\Delta\lambda$ to be small enough so that the results change negligibly as the step size is reduced. The appropriate step size to use in numerical calculations can be determined by “trial and error”, which in our case corresponds to $\Delta\lambda = 0.0005$.

Using relation 6.27, the numerical approximation to the QFI (Eq. 6.25) can be obtained:

$$Q_{diff}(\lambda_j) \approx \sum_{n=0}^{N} \frac{(p_n(\lambda_{j+1}) - p_n(\lambda_j))^2}{(\Delta\lambda)^2 p_n(\lambda_j)}. \tag{6.28}$$

Here, the exact QFI is approximated by a finite sum of the first N terms. The upper limit N is chosen to ensure that the truncation error is very small, again using a simple trial and error approach. This guarantees that the results are virtually unchanged by the truncation of the infinite series in the QFI definition in Eq. 6.25. In numerical calculations, the choice of N will also depend on the size of λ. In the limit of small λ, only a few of the lower energy eigenstates of the quantum vdP oscillator will be occupied with non-negligible probabilities, and the series can be truncated at $N = 15$ with no loss in accuracy. However, as the size of λ is increased, progressively more terms will need to be included in the sum to guarantee high accuracy of the approximation. In fact, a numerical investigation reveals that for the largest λ values that we will consider, a sufficient maximum upper limit to use is $N = 80$, which is indeed the value we use for all $\lambda > 1$.

In numerical calculations, we consider a region $0 < \lambda \leq 80$. This region is sufficient to display the contrasting behaviour of the QFI in the two limiting cases - strong and weak two-phonon emission - while still allowing for efficient numerical computation. The behaviour of the numerical QFI (Eq. 6.28) in this range of λ values is shown in Fig. 6.3(a). The most striking feature of the QFI revealed here is that it diverges in the limit $\lambda \to 0$. This behaviour could be related to the presence of a critical point at $\lambda = 0$ [39]. A divergent behaviour of the quantum vdP oscillator as the critical point is approached was recently noted in [39]. Beyond the vicinity of this point, the QFI steadily declines with λ. We thus expect the majority of information about the parameter λ to be available in the strong two-phonon emission regime, or $\lambda \ll 1$ limit. To better emphasise the limiting behaviours of the QFI for small and large values of λ, we also plot a function $\lambda Q_{diff}(\lambda_j) - 1/3$ in Fig. 6.3(b). In both limits ($\lambda \to 0$ and $\lambda \to \infty$), the function $\lambda Q(\lambda)$

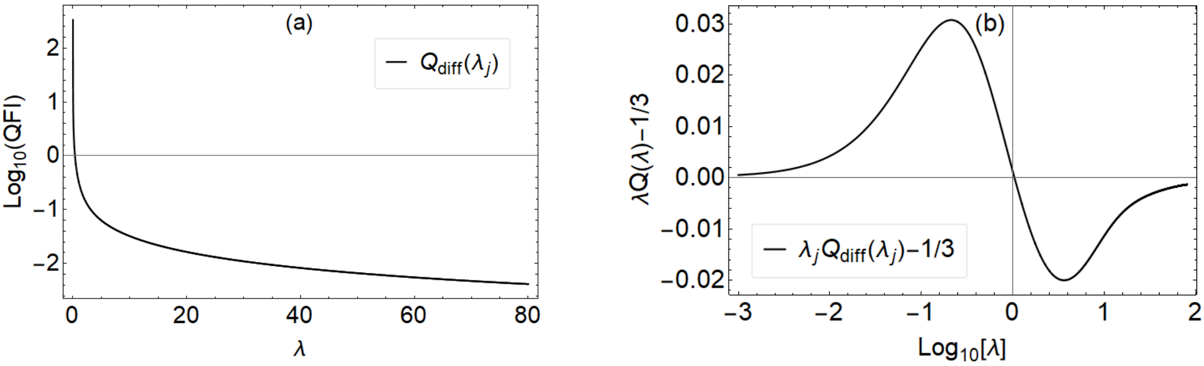

Figure 6.3: (a) Semi-log plot of the numerical QFI, $Q_{diff}(\lambda_j)$, against the ratio of the strengths of phonon absorption (i.e. gain) and emission processes, λ. (b) Semi-log plot of the numerically computed function $\lambda Q(\lambda) - 1/3$ against λ.

converges to $1/3$, albeit from different directions.

6.5 Analytical analysis

As anticipated, the size of λ determines which of the two dissipative processes - phonon emission or phonon absorption (i.e. gain) - dominates. Two limiting cases can be identified: $\lambda \ll 1$ and $\lambda \gg 1$, which, for the sake of brevity, we shall refer as the strong and weak two-phonon emission regimes, respectively. Unlike the steady state probability distribution, the QFI cannot be calculated analytically for arbitrary values of λ. However, as we now show, it is possible to obtain simple expressions for the QFI in the limits of small and large λ.

6.5.1 Strong two-phonon emission

In the small λ limit, the quantum vdP oscillator is largely confined to its ground state [4, 37, 114]. Hence, only the lower energy eigenstates will be occupied with non-negligible probabilities and the QFI can be approximated via a power series expansion [118].

The method for obtaining the power series approximation to the QFI is based on the direct expansion of the steady state generating function (Eq. 6.12). This is achieved by approximating the confluent hypergeometric functions in the expression for $G(z)$ as finite sums of the first six terms, in congruence with the definition [118]

$$\Phi(a;c;x) = \sum_{k=0}^{\infty} \frac{(a)_k x^k}{(c)_k k!}. \tag{6.29}$$

The probabilities p_n are then calculated using Eq. 6.13. The number of terms included in the power series expansion is determined by the desired precision of the QFI. Indeed, it can be shown that in order to obtain an expression for the QFI correct to $O(\lambda^p)$, terms of $O(\lambda^{p+2})$ need to be included in the series expansion of p_n. Accordingly, using Eq. 6.25, the power series approximation to the QFI, accurate to $O(\lambda^2)$, is found to take the form:

$$Q_{sum}(\lambda) = \frac{1}{3\lambda} + \frac{4}{9} - \frac{97}{36}\lambda + \frac{1681}{162}\lambda^2. \tag{6.30}$$

In agreement with the numerical case, this approximate form predicts divergent behaviour of the QFI in the $\lambda \to 0$ limit. Interestingly, here we can show analytically that the limit of $\lambda Q(\lambda)$ as λ approaches zero is indeed precisely $1/3$.

In order to assess the performance of the power series approximation in the strong two-phonon emission regime, we plot $Q_{sum}(\lambda)$ against the numerical QFI (Eq. 6.28) for λ values in the range $0 < \lambda \leq 0.3$. From Fig. 6.4(a), it is clear that the power series expanded QFI is a good approximation in a region $0 < \lambda \lesssim 0.12$. However, as λ gets progressively larger, the discrepancy between the two models increases. In Fig. 6.4(b) we also plot the function $\lambda Q(\lambda) - 1/3$ as given by the numerical and the power series expansion methods. The two approaches agree very well in a region $0 < \lambda \lesssim 0.07$, including the convergence of $\lambda Q(\lambda)$ to $1/3$ in the $\lambda \to 0$ limit. Beyond this region, however, $\lambda Q(\lambda)$ as given by the FDM reaches a plateau, whilst that given by the power series expansion method increases rapidly with λ.

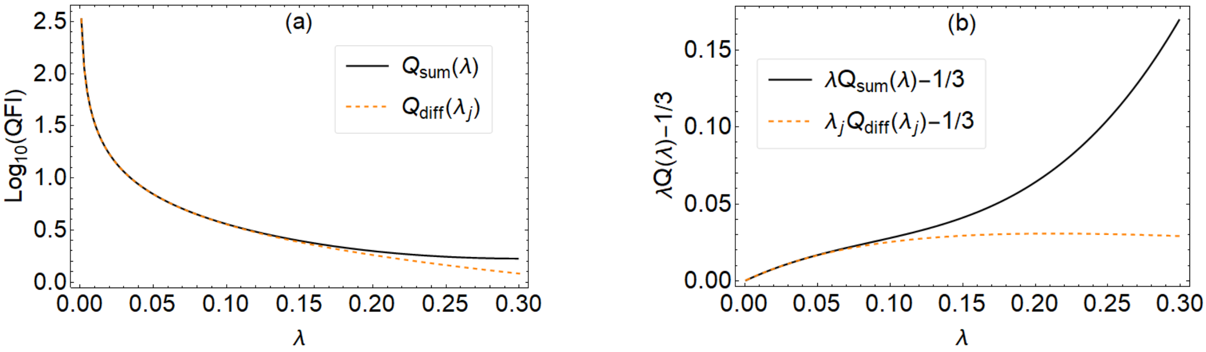

Figure 6.4: (a) Semi-log plot of the QFI against the ratio of the strengths of phonon absorption (i.e. gain) and emission processes, λ. The plot compares the numerical QFI, $Q_{diff}(\lambda_j)$, (orange dashed line) and the power series QFI, $Q_{sum}(\lambda)$, (black line) in the region $0 < \lambda \leq 0.3$ (b) Plot comparing the numerically computed function $\lambda_j Q_{diff}(j) - 1/3$ (orange dashed line) and the power series evaluated function $\lambda Q_{sum} - 1/3$ (black line) in the region $0 < \lambda \leq 0.3$.

6.5.2 Weak two-phonon emission

As dicussed in Sec. 6.2.3, in the limit of large λ, the steady state probability distribution of the quantum vdP oscillator follows a Gaussian distribution [118]. Appropriately, in this case the QFI can be approximated via [55]:

$$Q_{gauss}(\lambda) = \left(\Delta^2 n\right)^{-1} \left(\partial_\lambda \langle n\rangle\right)^2 + 8\left(\Delta^2 n\right)^{-2} \left(\partial_\lambda \langle n\rangle\right)^2 . \tag{6.31}$$

Using the expressions for the mean ($\langle n\rangle = \lambda/2$) and variance ($\Delta^2 n = 3\lambda/4$) of the quantum vdP oscillator, in the limit of large λ, the Gaussian approximation to the QFI is

$$Q_{gauss}(\lambda) = \frac{1}{3\lambda} + \frac{9}{8 + 18\lambda^2}. \tag{6.32}$$

According to this model, in the limit $\lambda \to \infty$, the QFI tends to zero. Hence, as expected, the majority of information about the parameter λ is available in the strong two-phonon emission regime. This analytical result also confirms that $\lambda Q(\lambda) \to 1/3$ as $\lambda \to +\infty$, as suggested by the numerical calculation.

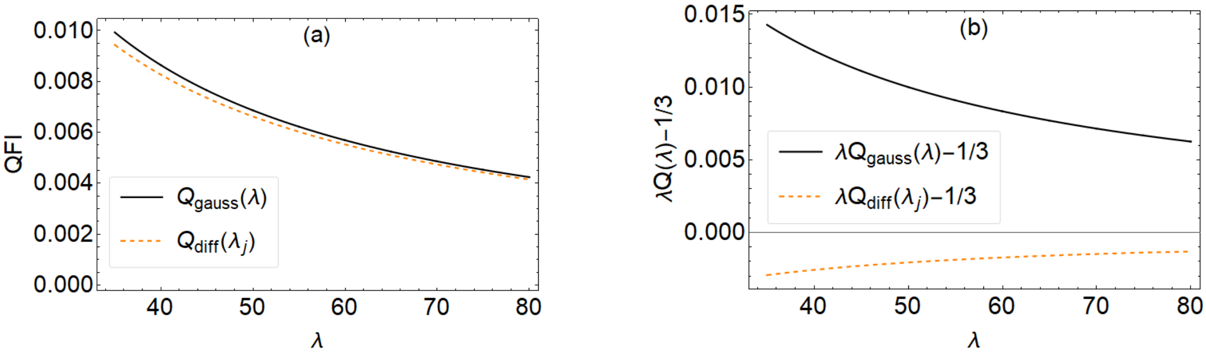

Figure 6.5: (a) Plot of the QFI against the ratio of the strengths of phonon absorption (i.e. gain) and emission processes, λ. The plot compares the numerical QFI, $Q_{diff}(j)$, (red dashed line) and the Gaussian QFI, $Q_{gauss}(\lambda)$, (black line) in the region $35 \leq \lambda \leq 80$ (b) Plot comparing the numerically computed function $\lambda_j Q_{diff}(\lambda_j) - 1/3$ (red dashed line) and the Gaussian evaluated function $\lambda Q_{gauss} - 1/3$ (black line) in the region $35 \leq \lambda \leq 80$.

Once again, we can assess the performance of the Gaussian approximation to the QFI in the weak two-phonon emission regime by plotting $Q_{gauss}(\lambda)$ against the numerical QFI (Eq. 6.4). From Fig. 6.5(a) it is clear that the two models predict very similar behaviour of the QFI for the entirety of the study region, $35 \leq \lambda \leq 80$. Unsurprisingly, the agreement between the two models also improves with λ. In Fig. 6.5(b) we plot the function $\lambda Q(\lambda) - 1/3$ as given by the numerical and Gaussian approximations to emphasise the limiting behaviour of the QFI. Although both the numerical and analytical calculations predict the same behaviour in the limit $\lambda \to \infty$, they converge towards it from different directions and at different rates.

6.6 Conclusions

In this chapter, we explored the application of local QET for estimating the ratio of the strengths of phonon absorption (i.e. gain) and emission processes, λ, in a quantum vdP oscillator. A quantum vdP oscillator has a well-defined average amplitude of oscillation in the steady state and serves as a simple model for the kinds of limit cycle oscillations encountered in optomechanics (in the blue-detuned regime). The simplicity of the model allows an analytical solution for the steady state to be obtained, which proves to be diagonal in the number state basis.

We explored the behaviour of the QFI in this system as a function of the only relevant parameter, λ. For small values of λ, only a very few of the number states are occupied in the steady state. In contrast, for very large λ, there is a Gaussian number distribution with an average that is proportional to λ. The corresponding behaviour of the QFI in the two limiting cases is very interesting. In the small λ limit, we showed, via power series expansion, that the QFI diverges. Other authors identified the $\lambda \to 0$ limit to be the critical point for the system [39]. It remains an interesting open question whether this divergent behaviour of the QFI at low λ is related to this critical behaviour. Here, we also showed analytically that $\lambda Q(\lambda)$ (the product of λ and the QFI) converges to $1/3$ in the limit $\lambda \to 0$. In contrast, in the large λ limit, we used general expressions that are available for QET in Gaussian models to approximate the QFI. Furthermore, using the Gaussian approximation, we showed that in the limit $\lambda \to \infty$, $\lambda Q(\lambda)$ also converges to $1/3$. The full numerical model was found to converge to the same limit as well, albeit from a different direction.

The interesting properties of the QFI for the quantum vdP oscillator would be worth investigating further. It is indeed curious that the $1/3$ behaviour arises in both small and large λ limits. The simple rational form of this limit could suggest a straightforward explanation to its origin. It is also curious that for $\lambda \gg 1$, the limit as given by the numerical and analytical methods is approached from opposite directions. It would be interesting to uncover the origin of this inconsistency upon more careful exploration. In this case, we have also shown that the measurement of the number operator constitutes the optimal strategy for estimating the parameter λ. In practice, however, other measurements, such as the quadrature measurements, might be more easily accessible. Future work could explore this concept in detail.

The initial goal of this chapter was to serve as a benchmark for exploring quantum parameter estimation in blue-detuned optomechanics. In this regime, the mechanical oscillator also exhibits self-sustained limit cycles although in a more complex model [34]. Perhaps our findings for the quantum vdP oscillator are also applicable to blue-detuned optomechanics. In particular, here, we have shown that the maximum information about the parameter λ is available in the $\lambda \to 0$ limit. This makes sense considering that a system is known to be highly sensitive to perturbations in the vicinity of its critical point, which the $\lambda = 0$ point has been identified as in [39]. Extending to blue-detuned optomechanics, this suggests that the best estimation performance could be achieved in a regime where a limit cycle is just forming rather than where it is well-developed.

Chapter 7

Conclusion

In this thesis, we have investigated optimal estimation of coupling parameters in driven-dissipative optomechanics. Accurate knowledge of these parameters is crucial for understanding the behaviour as well as any application of these systems. The thesis also explored the application of local QET in a quantum vdP oscillator. The findings, in this case, could aid our understanding of blue-detuned optomechanics where complex non-linear behaviour starts to emergence. In particular, it could give us an insight into a regime where the information about parameters of interest could in principle be maximised.

In Chapter 2 we outlined the single and multi-parameter estimation methods within the framework of local QET. In addition, we presented the single parameter approximation to multi-parameter estimation theory, which assumes that only one of the parameters is unknown at a time. Within this approximation, we outlined the estimation methods applicable to Gaussian models. This was the procedure we followed when estimating the linear and quadratic coupling constants within the framework of the quadratic optomechanical model. The approximation returned the "best-case-scenario" estimation performance for each of the parameters. In future work, it would be interesting to consider multi-parameter estimation (i.e. simultaneous estimation of both parameters) to investigate how these bounds compare to the most optimistic ones.

In Chapter 3 we introduced the approximate Hamiltonian models of optomechanics, including the linear and quadratic models, characterised by how many terms were retained in the expansion of the cavity frequency with respect to mechanical position. There, we also identified a master equation description for a driven-dissipative optomechanical system. Finally, we discussed the procedure for bilinearising the dynamics of the system along with the conditions for its validity. In the case of the linear model, we found the bilinear approximation to be valid for sufficiently strong cavity driving. In the case of the quadratic model, we additionally required a constraint on the magnitude of the quadratic coupling constant. This ensured that the dominant non-linear terms were small compared to the second order g_2-dependent terms we retained, hence justifying their exclusion. As a result of the bilinearisation, the system admitted a Gaussian steady state that could be fully characterised by its first and second moments; first moments were embodied in a non-linear system of equations of motion, whilst second moments in a steady state covariance matrix. The non-linearity of the equations of motion also signified the occurrence of static multistability within the system. Moreover, in all of the examples considered we restricted our study region to a regime where multistability could be completely avoided. The resultant "stable" region varied depending on driving and detuning. Intuitively, we found this stable region to be wider for a more stable system.

In Chapter 4 we examined single parameter estimation of the linear coupling constant in driven-dissipative optomechanics within the framework of the linear model in the red-detuned and resonant regimes. For the parameter values adopted (inspired by recent experiments), in the case of the red-detuned regime, the multistability of the system was avoided by setting an upper bound on the drive strengths considered. In the case of the resonant regime, the system was shown to remain stable at all intracavity photon numbers. The goal of this chapter was to find an optimal measurement strategy for estimating the linear coupling constant. For the red-detuned regime, we found the measurement of mechanical position to constitute the best strategy, whilst for the resonant regime, the choice of an optimal strategy was dependent on both temperature and driving. Interestingly, in most optomechanics experiments, measurements are typically performed on the light mode. However, our results suggest that in some parameter regimes probing the mechanical mode would be more advantageous. Finding ways of probing mechanics more directly would thus be recommended. Exploring the effects of temperature, in the case of the red-detuned regime, temperature was found to have a facilitating effect on the estimation precision of the linear coupling constant at lower driving powers. This temperature dependence was found to be considerably weaker for the resonant regime, where at sufficiently high intracavity photon numbers the predicted QFI limits were found to be qualitatively equal at all temperatures.

In Chapter 5 we considered single parameter approximation to multi-parameter estimation theory in a driven-dissipative optomechanical system described by a quadratic model in the red-detuned regime. In this case, the system was found to remain stable at all intracavity photon numbers. Expanding on the previous chapter, here we additionally explored the effects of corrections due to the quadratic term on the estimation precision of the linear coupling constant. Adopting the single parameter approximation to multi-parameter estimation theory applicable to Gaussian models, for realistic values of the model parameters, we found the quadratic coupling constant to be considerably harder to estimate than the linear one at lower intracavity photon numbers. At higher driving powers, their estimation precisions were found to be comparable instead. In general, the measurement of mechanical position was again found to constitute an optimal measurement strategy for both parameters, further justifying the importance of findings ways of probing the mechanical mode more directly. Interestingly, in this case, we found temperature to have an overall positive effect on the estimation performance of the quadratic coupling constant at all intracavity photon numbers within the study region. In fact, at a set drive strength, all temperatures above $T_m \approx 1.4 \times 10^{-5}$ K were found to facilitate the estimation of the quadratic coupling constant. This chapter also investigated single parameter estimation in the red-detuned regime within the framework of the purely quadratic model. Once again, the system was found to remain stable at intracavity photon numbers. As the name suggests, a purely quadratic model of optomechanics was obtained by assuming purely quadratic coupling with respect to the dimensionless position of the movable mirror. First, we presented the procedure for approximating the dynamics of the system via a bilinear master equation along with a discussion of its validity. In this case, we found the bilinear approximation to be valid for sufficiently strong cavity driving together with a detuning-dependent condition on the absolute value of the drive amplitude. The bilinearisation procedure essentially resulted in a single-mode Gaussian steady state described purely by a steady state covariance matrix for the mechanical mode only (as the steady state averages of the mechanics were found to vanish). Thanks to the simplicity of the bilinear model, in this case the analytical expressions for the QFI and the FIs for the measurements of mechanical position and momentum could also be obtained exactly. Moreover, a numerical analysis revealed that a stronger optomechanical interaction facilitates the estimation of the quadratic coupling constant at lower driving powers. Instead, at sufficiently high intracavity photon numbers, the estimation precision was found to saturate at exactly the same value, irrespective of the strength of the interaction. Additionally, in this case, the measurement of mechanical momentum was found to constitute an optimal strategy for estimating the quadratic coupling constant.

Finally, in Chapter 6 we explored the application of local QET in a quantum vdP oscillator to estimate the ratio of the strengths of phonon absorption and emission processes, λ. The goal of this chapter was to serve as a benchmark for studying quantum parameter estimation in blue-detuned optomechanics, where limit cycle oscillations also occur but in a more complex model. In the case of the quantum vdP oscillator, an analytical solution for the steady state can be obtained exactly which was shown to be diagonal in the number state basis and purely dependent on λ. Employing QET, explicit formulas for the classical and quantum precision bounds were then derived and the measurement of the number operator was shown to be optimal. Depending on the size of the parameter, two limiting cases were identified. For small values of λ, the quantum limit of the quantum vdP oscillator could be realised where the two-phonon emission process dominates and only a very few of the number states were populated in the steady state. The behaviour of the QFI, in this case, was studied analytically via a power series expansion. Through this method, the QFI was shown to display a divergent behaviour in the small λ limit. For large values of the parameter, the classical regime was recovered and the QFI was approximated via expressions available for QET in Gaussian models, adapted for scalar quantities. Through this method, the QFI was found to decay to zero in the limit of large λ. The employed analytical methods were found to agree well with the results obtained from numerical methods. In future work, it would be interesting to investigate how different the results would be for blue-detuned optomechanics in comparison to the simplified vdP model. In particular, based on our analysis, we would expect most information about the parameters of interest to be available close to $\lambda = 0$ point, corresponding to the critical point of the system. If these results could be extended to blue-detuned optomechanics, we would then expect the best estimation performance of the parameters to be achievable in a regime where a limit cycle is just forming rather than where it is well-developed.

Appendix A

Implicit differentiation

For completeness, we discuss the use of implicit differentiation in evaluating the classical and quantum precision bounds of the coupling parameters within the framework of the bilinear optomechanical model. The primary reason for employing implicit differentiation in this case is to avoid numerical differentiation.

As discussed in Sec. 3.4.2, the bilinear model of optomechanics is obtained by transforming into a frame in which the steady state displacements vanish and hence, where only small quantum fluctuations around the semi-classical steady state can be considered [4, 62]. This, in turn, requires strong cavity driving (along with a constraint on the magnitude of the quadratic coupling constant in the case of the quadratic optomechanical model). Implementing these displacements then results in the non-linear set of equations for the steady state values of the system's first moments (Eqs.3.34-3.37). Due to the non-linearity of these equations, enforced by their implicit dependence on the coupling constants through the effective parameters (effective mechanical frequency ω_{eff}, effective detuning Δ_{eff} and effective coupling strength g_{eff}), numerical methods would typically be required to evaluate their derivatives, which are essential for evaluating the classical and quantum precision bounds of the coupling constants (see Eqs. 4.7 and 4.3 or Eqs. 5.7

and 5.3 for the linear and quadratic models, respectively). Instead, the implementation of implicit differentiation results in a non-linear set of equations for the derivatives of the system's steady state first moments that can be solved numerically. In other words, implicit differentiation ensures that all of the relevant quantities can be conveyed in the numerical solutions to the set of equations for the steady state averages of the system. Indeed, using this method, we find the following analytical expressions for the derivatives of the steady state averages with respect to the linear and quadratic coupling constants (valid for the quadratic model):

$$
\begin{aligned}
&\frac{\partial Q_0}{\partial g_1}\\
&= \frac{256\sqrt{2} g_1 \epsilon^3 \omega_m \left(\left(4\Delta_{\mathit{eff}}^2+\kappa^2\right)\left(\Gamma_m^2+4\omega_m^2\right)+16 g_2 \epsilon^2 \omega_m\right)}{\left(4\Delta_{\mathit{eff}}^2+\kappa^2\right)\left(\left(4\Delta_{\mathit{eff}}^2+\kappa^2\right)\left(\Gamma_m^2+4\omega_m^2\right)+32 g_2 \epsilon^2 \omega_m\right)^2 \left(1-\frac{256 g_1^2 \epsilon^2 \Delta_{\mathit{eff}} \omega_m \left(4\Delta_{\mathit{eff}}^2+\kappa^2\right)\left(\Gamma_m^2+4\omega_m^2\right)^2}{\left(\left(4\Delta_{\mathit{eff}}^2+\kappa^2\right)\left(\Gamma_m^2+4\omega_m^2\right)+32 g_2 \epsilon^2 \omega_m\right)^3}\right)}\\
&- \frac{2048\sqrt{2} g_1 \epsilon^3 \Delta_{\mathit{eff}}^2 \omega_m \left(\left(4\Delta_{\mathit{eff}}^2+\kappa^2\right)\left(\Gamma_m^2+4\omega_m^2\right)+16 g_2 \epsilon^2 \omega_m\right)}{\left(4\Delta_{\mathit{eff}}^2+\kappa^2\right)^2\left(\left(4\Delta_{\mathit{eff}}^2+\kappa^2\right)\left(\Gamma_m^2+4\omega_m^2\right)+32 g_2 \epsilon^2 \omega_m\right)^2 \left(1-\frac{256 g_1^2 \epsilon^2 \Delta_{\mathit{eff}} \omega_m \left(4\Delta_{\mathit{eff}}^2+\kappa^2\right)\left(\Gamma_m^2+4\omega_m^2\right)^2}{\left(\left(4\Delta_{\mathit{eff}}^2+\kappa^2\right)\left(\Gamma_m^2+4\omega_m^2\right)+32 g_2 \epsilon^2 \omega_m\right)^3}\right)},
\end{aligned}
\tag{A.1}
$$

$$
\begin{aligned}
&\frac{\partial P_0}{\partial g_1}\\
&= -\frac{1024\sqrt{2} g_1 \kappa \epsilon^3 \Delta_{\mathit{eff}} \omega_m \left(\left(4\Delta_{\mathit{eff}}^2+\kappa^2\right)\left(\Gamma_m^2+4\omega_m^2\right)+16 g_2 \epsilon^2 \omega_m\right)}{\left(4\Delta_{\mathit{eff}}^2+\kappa^2\right)^2\left(\left(4\Delta_{\mathit{eff}}^2+\kappa^2\right)\left(\Gamma_m^2+4\omega_m^2\right)+32 g_2 \epsilon^2 \omega_m\right)^2 \left(1-\frac{256 g_1^2 \epsilon^2 \Delta_{\mathit{eff}} \omega_m \left(4\Delta_{\mathit{eff}}^2+\kappa^2\right)\left(\Gamma_m^2+4\omega_m^2\right)^2}{\left(\left(4\Delta_{\mathit{eff}}^2+\kappa^2\right)\left(\Gamma_m^2+4\omega_m^2\right)+32 g_2 \epsilon^2 \omega_m\right)^3}\right)},
\end{aligned}
\tag{A.2}
$$

$$
\begin{aligned}
&\frac{\partial x_0}{\partial g_1}\\
&= \frac{16\sqrt{2}\epsilon^2 \omega_m}{\left(4\Delta_{\mathit{eff}}^2+\kappa^2\right)\left(\Gamma_m^2+4\omega_m^2\right)+32 g_2 \epsilon^2 \omega_m}\\
&+ \frac{8192\sqrt{2} g_1^2 \epsilon^4 \Delta_{\mathit{eff}} \omega_m^2 \left(\Gamma_m^2+4\omega_m^2\right)\left(\left(4\Delta_{\mathit{eff}}^2+\kappa^2\right)\left(\Gamma_m^2+4\omega_m^2\right)+16 g_2 \epsilon^2 \omega_m\right)}{\left(\left(4\Delta_{\mathit{eff}}^2+\kappa^2\right)\left(\Gamma_m^2+4\omega_m^2\right)+32 g_2 \epsilon^2 \omega_m\right)^4 \left(1-\frac{256 g_1^2 \epsilon^2 \Delta_{\mathit{eff}} \omega_m \left(4\Delta_{\mathit{eff}}^2+\kappa^2\right)\left(\Gamma_m^2+4\omega_m^2\right)^2}{\left(\left(4\Delta_{\mathit{eff}}^2+\kappa^2\right)\left(\Gamma_m^2+4\omega_m^2\right)+32 g_2 \epsilon^2 \omega_m\right)^3}\right)},
\end{aligned}
\tag{A.3}
$$

$$\begin{aligned}&\frac{\partial p_0}{\partial g_1}\\&=\frac{8\sqrt{2}\epsilon^2\Gamma_m}{\left(4\Delta_{eff}^2+\kappa^2\right)\left(\Gamma_m^2+4\omega_m^2\right)+32g_2\epsilon^2\omega_m}\\&+\frac{4096\sqrt{2}g_1^2\epsilon^4\Delta_{eff}\Gamma_m\omega_m\left(\Gamma_m^2+4\omega_m^2\right)\left(\left(4\Delta_{eff}^2+\kappa^2\right)\left(\Gamma_m^2+4\omega_m^2\right)+16g_2\epsilon^2\omega_m\right)}{\left(\left(4\Delta_{eff}^2+\kappa^2\right)\left(\Gamma_m^2+4\omega_m^2\right)+32g_2\epsilon^2\omega_m\right)^4\left(1-\frac{256g_1^2\epsilon^2\Delta_{eff}\omega_m\left(4\Delta_{eff}^2+\kappa^2\right)(\Gamma_m^2+4\omega_m^2)^2}{\left(\left(4\Delta_{eff}^2+\kappa^2\right)(\Gamma_m^2+4\omega_m^2)+32g_2\epsilon^2\omega_m\right)^3}\right)},\end{aligned}\tag{A.4}$$

$$\begin{aligned}&\frac{\partial Q_0}{\partial g_2}\\&=\frac{16384\sqrt{2}g_1^2\epsilon^5\Delta_{eff}^2\omega_m^2\left(3\left(4\Delta_{eff}^2+\kappa^2\right)\left(\Gamma_m^2+4\omega_m^2\right)+32g_2\epsilon^2\omega_m\right)}{\left(4\Delta_{eff}^2+\kappa^2\right)^2\left(\left(4\Delta_{eff}^2+\kappa^2\right)\left(\Gamma_m^2+4\omega_m^2\right)+32g_2\epsilon^2\omega_m\right)^3\left(1-\frac{256g_1^2\epsilon^2\Delta_{eff}\omega_m\left(4\Delta_{eff}^2+\kappa^2\right)(\Gamma_m^2+4\omega_m^2)^2}{\left(\left(4\Delta_{eff}^2+\kappa^2\right)(\Gamma_m^2+4\omega_m^2)+32g_2\epsilon^2\omega_m\right)^3}\right)}\\&-\frac{2048\sqrt{2}g_1^2\epsilon^5\omega_m^2\left(3\left(4\Delta_{eff}^2+\kappa^2\right)\left(\Gamma_m^2+4\omega_m^2\right)+32g_2\epsilon^2\omega_m\right)}{\left(4\Delta_{eff}^2+\kappa^2\right)\left(\left(4\Delta_{eff}^2+\kappa^2\right)\left(\Gamma_m^2+4\omega_m^2\right)+32g_2\epsilon^2\omega_m\right)^3\left(1-\frac{256g_1^2\epsilon^2\Delta_{eff}\omega_m\left(4\Delta_{eff}^2+\kappa^2\right)(\Gamma_m^2+4\omega_m^2)^2}{\left(\left(4\Delta_{eff}^2+\kappa^2\right)(\Gamma_m^2+4\omega_m^2)+32g_2\epsilon^2\omega_m\right)^3}\right)},\end{aligned}\tag{A.5}$$

$$\begin{aligned}&\frac{\partial P_0}{\partial g_2}\\&=\frac{8192\sqrt{2}g_1^2\kappa\epsilon^5\Delta_{eff}\omega_m^2\left(3\left(4\Delta_{eff}^2+\kappa^2\right)\left(\Gamma_m^2+4\omega_m^2\right)+32g_2\epsilon^2\omega_m\right)}{\left(4\Delta_{eff}^2+\kappa^2\right)^2\left(\left(4\Delta_{eff}^2+\kappa^2\right)\left(\Gamma_m^2+4\omega_m^2\right)+32g_2\epsilon^2\omega_m\right)^3\left(1-\frac{256g_1^2\epsilon^2\Delta_{eff}\omega_m\left(4\Delta_{eff}^2+\kappa^2\right)(\Gamma_m^2+4\omega_m^2)^2}{\left(\left(4\Delta_{eff}^2+\kappa^2\right)(\Gamma_m^2+4\omega_m^2)+32g_2\epsilon^2\omega_m\right)^3}\right)},\end{aligned}\tag{A.6}$$

$$\begin{aligned}&\frac{\partial x_0}{\partial g_2}\\&=-\frac{16\sqrt{2}g_1\epsilon^2\omega_m\left(\frac{4096g_1^2\epsilon^4\Delta_{eff}\omega_m^2\left(\Gamma_m^2+4\omega_m^2\right)\left(3\left(4\Delta_{eff}^2+\kappa^2\right)\left(\Gamma_m^2+4\omega_m^2\right)+32g_2\epsilon^2\omega_m\right)}{\left(\left(4\Delta_{eff}^2+\kappa^2\right)(\Gamma_m^2+4\omega_m^2)+32g_2\epsilon^2\omega_m\right)^3\left(1-\frac{256g_1^2\epsilon^2\Delta_{eff}\omega_m\left(4\Delta_{eff}^2+\kappa^2\right)\left(\Gamma_m^2+4\omega_m^2\right)^2}{\left(\left(4\Delta_{eff}^2+\kappa^2\right)\left(\Gamma_m^2+4\omega_m^2\right)+32g_2\epsilon^2\omega_m\right)^3}\right)}+32\epsilon^2\omega_m\right)}{\left(\left(4\Delta_{eff}^2+\kappa^2\right)\left(\Gamma_m^2+4\omega_m^2\right)+32g_2\epsilon^2\omega_m\right)^2},\end{aligned}\tag{A.7}$$

$$\frac{\partial p_0}{\partial g_2}$$

$$= -\frac{8\sqrt{2} g_1 \epsilon^2 \Gamma_m \left(\frac{4096 g_1^2 \epsilon^4 \Delta_{eff} \omega_m^2 \left(\Gamma_m^2 + 4\omega_m^2\right) \left(3\left(4\Delta_{eff}^2 + \kappa^2\right)\left(\Gamma_m^2 + 4\omega_m^2\right) + 32 g_2 \epsilon^2 \omega_m\right)}{\left(\left(4\Delta_{eff}^2 + \kappa^2\right)(\Gamma_m^2 + 4\omega_m^2) + 32 g_2 \epsilon^2 \omega_m\right)^3 \left(1 - \frac{256 g_1^2 \epsilon^2 \Delta_{eff} \omega_m \left(4\Delta_{eff}^2 + \kappa^2\right)\left(\Gamma_m^2 + 4\omega_m^2\right)^2}{\left(\left(4\Delta_{eff}^2 + \kappa^2\right)\left(\Gamma_m^2 + 4\omega_m^2\right) + 32 g_2 \epsilon^2 \omega_m\right)^3}\right)} + 32\epsilon^2 \omega_m \right)}{\left(\left(4\Delta_{eff}^2 + \kappa^2\right)\left(\Gamma_m^2 + 4\omega_m^2\right) + 32 g_2 \epsilon^2 \omega_m\right)^2}. \tag{A.8}$$

Equivalent formulas for the derivatives of the steady state averages with respect to the linear coupling constant (g_1), valid for the linear model, can be recovered by simply setting $g_2 = 0$.

Appendix B

Derivation of the amplitude equation for limit cycle oscillations

Here, we present a detailed derivation of the amplitude equation (6.3).

As discussed in Sec. 6.2, classically, the evolution of the vdP oscillator can be described via a non-linear second order differential equation:

$$\ddot{x} - \gamma_1(1 - \gamma_2 x^2)\dot{x} + \omega_0^2 x = 0, \tag{B.1}$$

with ω_0 the natural frequency of the oscillator and x a dimensionless displacement [39, 108, 111]. The resulting limit cycle can then be approximated by the amplitude equation (6.3), recovered through a change of variables:

$$x = \frac{\alpha + \alpha^*}{2}, \tag{B.2}$$

$$\dot{x} = i\omega_0 \frac{\alpha^* - \alpha}{2}. \tag{B.3}$$

Subsequently, differentiating Eq. B.3 with respect to time, we obtain

$$\ddot{x} = i\omega_0 \frac{\dot{\alpha}^* - \dot{\alpha}}{2}. \tag{B.4}$$

Substituting the expressions for x, $\dot{x}$ and $\ddot{x}$ into Eq. B.1, we then end up with a following first order equation:

$$-(\dot{\alpha}^* - \dot{\alpha}) + \gamma_1 \left(\alpha^* - \alpha - \frac{\gamma_2}{4}(|\alpha|^2\alpha^* + \alpha^{*3} - \alpha^3 - |\alpha|^2\alpha) \right) + \omega_0(\alpha + \alpha^*) = 0. \tag{B.5}$$

Separating the real and imaginary parts, we obtain a first order differential equation for α:

$$\dot{\alpha} = -i\omega_0 + \alpha\gamma_1 \left(1 - \frac{\gamma_2}{4}(|\alpha|^2 + \alpha^3) \right). \tag{B.6}$$

Finally, the $O(\alpha^3)$ term can be neglected provided that both conditions: $\gamma_1 \ll \omega_0$ and $\gamma_2 \ll \omega_0/\gamma_1$ are satisfied, resulting in the amplitude equation (6.3) [4].

Bibliography

[1] K. Sala, T. Doicin, A. D. Armour, T. Tufarelli, Phys. Rev. A **104**, 033508 (2021).

[2] M. Aspelmeyer, T. Kippenberg, F. Marquardt, Rev. Mod. Phys. **86**, 1391 (2014).

[3] I. Favero, F. Marquardt, New J. Phys. **16**, 085006 (2014).

[4] W. P. Bowen, G. J. Milburn, *Quantum optomechanics* (CRC Press, Boca Raton, 2016).

[5] V. B. Braginsky, A. B. Manukin, Soviet Physics-JETP **25**, 653 (1967).

[6] V. B. Braginsky, A. B. Manukin, M. Y. Tikhonov, Soviet Journal of Experimental and Theoretical Physics **31**, 829 (1970).

[7] Y. C. Liu, Y. W. Hu, C. W. Wong, Y. F. Xiao, Chinese Physics B **22**, 114213 (2013).

[8] P. N. Lebedev, Annalen der Physik **6**, 433 (1901).

[9] B. Kubala, M. Ludwig, F. Marquardt, *Optomechanics In Complex Phenomena in Nanoscale Systems* (Springer, Dordrecht, 2009).

[10] F. F. Nichols, G. F. Hull, Phys. Rev. (Series I) **13**, 307 (1901).

[11] A. Einstein, Phys. Z. **10**, 817 (1909).

[12] O. Frisch, Zeitschrift für Physik B **86**, 42 (1933).

[13] R. Beth, Phys. Rev. **50**, 115 (1936).

[14] J. F. Morizur, M. Colla, H. A. Bachor, American Journal of Physics **76**, 1022 (2008).

[15] V. Giovannetti, S. Lloyd, and L. Maccone, Nature **412**, 417 (2001).

[16] C. M. Caves, Phys. Rev. Lett. **45**, 75 (1980).

[17] V. B. Braginsky, F. Y. Khalili, *Quantum Measurements* (Cambridge University Press, New York, 1995).

[18] V. B. Braginsky, A. B. Manukin, *Measurement of weak forces in Physics experiments* (University of Chicago Press, Chicago, 1977).

[19] C. F. Ockeloen-Korppi, E. Damskägg, J.-M. Pirkkalainen, A. A. Clerk, M. J. Woolley, M. A. Sillanpää, Phys. Rev. Lett. **117**, 140401 (2016).

[20] M. Aspelmeyer, P. Meystre, K. Schwab, Physics Today **65**, 29 (2012).

[21] F. Y. Khalili, S. L. Danilishin, Progress in Optics **61**, 113 (2016).

[22] P. Meystre, Annalen der Physik **525**, 215 (2013).

[23] V. B. Braginsky, Zhurnal Eksperimental'noy Teoreticheskoy Fiziki **53**, 1434 (1967).

[24] I. Wilson-Rae, N. Nooshi, W. Zwerger, T. J. Kippenberg, Phys. Rev. Lett. **99**, 093901 (2007).

[25] T. Rocheleau, T. Ndukum, C. Macklin, J. B. Hertzberg, A. A. Clerk, K. C. Schwab, Nature **463**, 72 (2010).

[26] J. D. Teufel, T. Donner, D. Li, J. W. Harlow, M. S. Allman, K. Cicak, A. J. Sirois, J. D. Whittaker, K. W. Lehnert, R. W. Simmonds, Nature **475**, 359 (2011).

[27] J. Chan, A. T. P. Mayer, A. H. Safavi-Naeini, J. T. Hill, A. Krause, S. Gröblacher, M. Aspelmeyer, O. Painter, Nature **478**, 89 (2011).

[28] R. Riviere, S. Deleglise, S. Weis, E. Gavartin, O. Arcizet, A. Schliesser, T. Kippenberg, Phys. Rev. A **83**, 063835 (2011).

[29] S. Banerjee, A. Jayannavar, arXiv preprint arXiv:1902.08576 (2019).

[30] E. E. Wollman, C. U. Lei, A. J. Weinstein, J. Suh, A. Kronwald, F. Marquardt, A. A. Clerk, K. C. Schwab, Science **349**, 952 (2015).

[31] R. Riedinger, A. Wallucks, I. Marinković, C. Löschnauer, M. Aspelmeyer, S. Hong, S. Gröblacher, Nature **556**, 473 (2018).

[32] C. F. Ockeloen-Korppi, E. Damskägg, J. M. Pirkkalainen, M. Asjad, A. A. Clerk, F. Massel, M. J. Woolley, M. A. Sillanpää, Nature **556**, 478 (2018).

[33] M. G. Paris, International Journal of Quantum Information **7**, 125 (2009).

[34] N. Lörch, J. Qian, A. Clerk, F. Marquardt, K. Hammerer, Phys. Rev. X **4**, 011015 (2014).

[35] C. Genes, A. Mari, D. Vitali, P. Tombesi, Advances in atomic, molecular, and optical physics **57**, 33 (2009).

[36] D. A. Rodrigues, A. D. Armour, Phys. Rev. Lett. **104**, 053601 (2010).

[37] T. E. Lee, H. R. Sadeghpour, Phys. Rev. Lett. **111**, 234101 (2013).

[38] L. B. Arosh, M. C. Cross, R. Lifshitz, Phys. Rev. Research **3**, 013130 (2021).

[39] S. Dutta, N. R. Cooper, Phys. Rev. Lett. **123**, 250401 (2019).

[40] C. K. Law, Phys. Rev. A **51**, 2537 (1995).

[41] J. Angeles, *Dynamic response of linear mechanical systems: Modeling, analysis and simulation* (Springer Science & Business Media, New York, 2011).

[42] M. Szczykulska, T. Baumgratz, A. Datta, Adv. Phys. X **1**, 621 (2016).

[43] C. W. Helstrom, Journal of Statistical Physics **1**, 231-252 (1969).

[44] A. S. Holevo, *Probabilistic and statistical aspects of quantum theory* (North-Holland Publishing Company, Amsterdam, 1982).

[45] Z. Ji, G. Wang, R. Duan, Y. Feng, M. Ying, IEEE Transactions on Information Theory **54**, 5172-5185 (2008).

[46] L. Bakmou, M. Daoud, Journal of Physics A: Mathematical and Theoretical, **53**, 385301 (2020).

[47] C. M. Caves, Phys. Rev. D **23**, 1693 (1981).

[48] M. de Burgh, S. D. Bartlett, Phys. Rev. A **72**, 042301 (2005).

[49] J. Preskill, arXiv:quant-ph/0010098 (2000).

[50] I. Chuang, Phys. Rev. Lett. **85**, 2006 (2000).

[51] Y. Yang, G. Chiribella, M. Hayashi, Commun. Math. Phys. **368**, 223 (2019).

[52] G. J. Milburn, W. Y. Chen, K. R. Jones, Phys. Rev. A **50**, 801 (1994).

[53] G. Chiribella, G. M. D'Ariano, M. F. Sacchi, Phys. Rev. A **73**, 062103 (2006).

[54] S. Alipour, M. Mehboudi, A. T. Rezakhani, Phys. Rev. Lett. **112**, 120405 (2014).

[55] D. Braun, G. Adesso, F. Benatti, R. Floreanini, U. Marzolino, M. W. Mitchell, S. Pirandola, 2018, Rev. Mod. Phys. **90**, 035006 (2018).

[56] A. Monras, arXiv:1303.3682 (2013).

[57] J. Liu, H. Yuan, X. M. Lu, X. Wang, Journal of Physics A: Mathematical and Theoretical **53**, 023001 (2019).

[58] J. S. Sidhu, P. Kok, AVS Quantum Science **2**, 014701 (2020).

[59] A. Serafini, *Quantum Continuous Variables: A Primer of Theoretical Methods* (CRC Press, Boca Raton, 2017).

[60] C. Oh, C. Lee, C. Rockstuhl, H. Jeong, J. Kim, H. Nha, S. Y. Lee, npj Quantum Information **5**, 1 (2019).

[61] D. Šafránek, Journal of Physics A: Mathematical and Theoretical **52**, 035304 (2018).

[62] C. Sanavio, J. Z. Bernád, A. Xuereb, Phys. Rev. A **102**, 013508 (2020).

[63] M. Cerezo, A. Sone, J. L. Beckey, P. J. Coles, Quantum Science and Technology **6**, 035008 (2021).

[64] E. L. Lehmann, G. Casella, *Theory of point estimation.* (Springer Science & Business Media, New York, 2006).

[65] M. Nielsen, I. Chuang, *Quantum Computation and Quantum Information* (Cambridge University Press, New York, 2000).

[66] T. Baumgratz, A. Datta, Phys. Rev. Lett **116**, 030801 (2016).

[67] P. C. Humphreys, M. Barbieri, A. Datta, I. A. Walmsley, Phys. Rev. Lett. **111**, 070403 (2013).

[68] H. Breuer, F. Petruccione, *The theory of open quantum systems* (Oxford University Press, Oxford, 2010).

[69] G. Adesso, S. Ragy, A. R. Lee, Open Systems & Information Dynamics **21**, 1440001 (2014).

[70] C. W. Helstrom, Found. Phys. **4**, 453 (1974).

[71] T. J. Kippenberg, K. J. Vahala, Science **321**, 1172 (2008).

[72] K. Jacobs, I. Tittonen, H. M. Wiseman, S. Schiller, Phys. Rev. A **60**, 538 (1999).

[73] M. Pinard, Y. Hadjar, A. Heidmann, The European Physical Journal D-Atomic, Molecular, Optical and Plasma Physics **7**, 107 (1999).

[74] K. C. Schwab, M. L. Roukes, Physics Today **58**, 36 (2005).

[75] The LIGO Scientific Collaboration et al., Classical and Quantum Gravity **32**, 074001 (2015).

[76] T. P. Purdy, R. W. Peterson, C. A. Regal, Science **339**, 801 (2013).

[77] P. R. Saulson, Phys. Rev. D **42**, 2437 (1990).

[78] M. Poot, H. S. van der Zant, Physics Reports **511**, 273 (2012).

[79] A. Dorsel, J. D. McCullen, P. Meystre, E. Vignes, H. Walther, Phys. Rev. Lett. **51**, 1550 (1983).

[80] R. Ghobadi, S. Gholizadeh, M. Mazaheri, International Journal of Optics and Photonics (IJOP) **9**, 19 (2015).

[81] R. Ghobadi, A. R. Bahrampour, C. Simon, Phys. Rev. A **84**, 033846 (2011).

[82] K. Sala, T. Tufarelli, Scientific Reports **8**, 157 (2018).

[83] G. T. Moore, Journal of Mathematical Physics **11**, 2679 (1970).

[84] J. S. Zhang, M. C. Li, A. X. Chen, Phys. Rev. A **99**, 013843 (2019).

[85] J. D. Thompson, B. M. Zwickl, A. M. Jayich, F. Marquardt, S. M. Girvin, J. G. E. Harris, Nature (London) **452**, 72 (2008).

[86] J. Q. Liao, F. Nori, Scientific Reports **4**, 6302 (2014).

[87] O. Pinel, P. Jian, N. Treps, C. Fabre, D. Braun, Phys. Rev. A **88**, 040102 (2013).

[88] A. Nunnenkamp, K. Børkje, J. G. E. Harris, S. M. Girvin, Phys. Rev. A **82**, 021806 (2010).

[89] M. Brunelli, A. Xuereb, A. Ferraro, G. De Chiara, N. Kiesel, M. Paternostro, New J. Phys. **17**, 035016 (2015).

[90] S. P. Kumar, M. B. Plenio, arXiv:1708.05659 (2017).

[91] S. Kryszewski, J. Czechowska-Kryszk, arXiv:0801.1757 (2008).

[92] H. Zoubi, M. Orenstein, A. Ron, Phys. Rev. A **62**, 033801 (2000).

[93] M. T. Naseem, A. Xuereb, Ö. E. Müstecaplıoğlu, Phys. Rev. A **98**, 052123 (2018).

[94] H. Carmichael, *Statistical Methods in Quantum Optics 1* (Springer-Verlag Berlin Heidelberg, New York, 1999).

[95] F. Marquardt, A. Püttmann, arXiv:0809.4403 (2008).

[96] M. Schlosshauer, *Decoherence and the quantum-to-classical transition* (Springer Berlin Heidelberg, New York, 2010).

[97] D. Bacon, arXiv:quant-ph/0305025 (2003).

[98] K. C. Schwab, M. L. Roukes, Physics Today **58**, 36 (2005).

[99] R. Paschotta, *Encyclopedia of Laser Physics and Technology* (Wiley-VCH, Weinheim, 2008).

[100] C. Ventura-Velázquez, B. M. Rodríguez-Lara, H. M. Moya-Cessa, Physica Scripta **90**, 068010 (2015).

[101] C. A. Potts, E. Varga, V. A. S. V. Bittencourt, S. Viola Kusminskiy, J. P. Davis, Phys. Rev. X **11**, 031053 (2021).

[102] K. Ikeda, O. Akimoto, Phys. Rev. Lett. **48**, 617 (1982).

[103] J. Z. Bernád, C. Sanavio, A. Xuereb, Phys. Rev. A **97**, 063821 (2018).

[104] K. Nakamura, M. K. Fujimoto, arXiv:1711.03713 (2017).

[105] F. Schneiter, S. Qvarfort, A. Serafini, A. Xuereb, D. Braun, D. Rätzel, D. E. Bruschi, Phys. Rev. A **101**, 033834 (2020).

[106] M. Brunelli, O. Houhou, D. W. Moore, A. Nunnenkamp, M. Paternostro, A. Ferraro, Phys. Rev. A **98**, 063801 (2018).

[107] Q. Zheng, Y. Yao, Y. Li, Phys. Rev. A **93**, 013848 (2016).

[108] M. Tsatsos, arXiv preprint arXiv:0803.1658 (2008).

[109] M. L. Cartwright, J. Balthazar van der Pol, London Math. Soc. **35**, 367 (1960).

[110] A. Carollo, B. Spagnolo, D. Valenti, Entropy, **20**, 485 (2018).

[111] C. Davis-Tilley, *Synchronisation in open quantum systems* (PhD thesis, University of Nottingham, 2018).

[112] S. Walter, A. Nunnenkamp, C. Bruder, Phys. Rev. Lett. **112**, 094102 (2014).

[113] S. H Strogatz, *Nonlinear Dynamics and Chaos* (Westview Press, Cambridge, 1994).

[114] T. E. Lee, C. Chan, S. Wang, Phys. Rev. E **89**, 022913 (2014).

[115] N. Lörch, E. Amitai, A. Nunnenkamp, C. Bruder, Phys. Rev. Lett., **117**, 073601 (2016).

[116] A. S. Pikovsky, M. Rosenblum, J. Kurths, *Synchronization: A Universal Concept in Nonlinear Science* (Cambridge University Press, New York, 2001).

[117] L. B. Arosh, M. C. Cross, R. Lifshitz, Phys. Rev. Research 3, 013130 (2021).

[118] V. V. Dodonov, S. S. Mizrahi, J. Phys. A: Math. Gen. **30**, 5657 (1997).

[119] G. P. Hildred, Optica Acta: International Journal of Optics, **27**, 1621-1627 (1980).

[120] H. Bateman, *Higher transcendental functions [volumes i-iii]* (McGraw-Hill Book Company, New York, 1953).

[121] R. Shamey, X. Zhao, *Modelling, simulation and control of the dyeing process* (Woodhead Publishing, Cambridge, 2014).

[122] T.Y. Na, *Computational methods in engineering boundary value problems* (Academic press, New York, 1980).

[123] D. M. Causon, C. G. Mingham, *Introductory finite difference methods for PDEs* (Ventus Publishing, 2010).

[124] R. J. LeVeque, *Finite difference methods for ordinary and partial differential equations: steady-state and time-dependent problems* (SIAM, Philadelphia, 2007).